University of Nevada, Reno

5 ns Electric pulses evoke longer-lived calcium responses in adrenal chromaffin cells than the physiological stimulus: an experimental and computational study

A thesis submitted in partial fulfillment of the

requirements for the degree of Master of Science

in Biomedical Engineering

By

Ruby Khattak (née Sukhraj)

Dr. Gale Louise Craviso/ Thesis advisor

Dr. Indira Chatterjee/Thesis co-advisor

December 2019

UNIVERSITY OF NEVADA, RENO

THE GRADUATE SCHOOL

We recommend that the thesis

prepared under our supervision by

Ruby Khattak (née Sukhraj)

Entitled

5 ns Electric pulses evoke longer-lived calcium responses in adrenal chromaffin cells than the physiological stimulus: an experimental and computational study

be accepted in partial fulfillment of the requirements for the degree of

MASTER OF SCIENCE

Gale Louise Craviso, Ph. D., Advisor

Indira Chatterjee, Ph. D., Co-Advisor

Ji Hwan Yoon, Ph. D., Committee Member

Reuben Dagda, Ph. D., Committee Member

Normand LeBlanc, Ph. D., Graduate School Representative

David W. Zeh, Ph. D., Dean, Graduate School

December 2019

Abstract

Nanosecond duration electric pulses of high electric field magnitudes (>1 MV/m) are being explored by our group as a novel type of electric stimulus for evoking catecholamine release from neuroendocrine adrenal chromaffin cells. The overall goal of this work is to understand why 5 ns, 5 MV/m pulses evoke longer-lived calcium responses than nicotinic cholinergic receptor activation, the physiological stimulus. *In vivo*, stimulation of chromaffin cells by acetylcholine causes calcium influx through voltage-gated calcium channels (VGCCs) that increases the concentration of calcium at sites where exocytosis of catecholamine-storing secretory granules occurs, evoking the release of catecholamines. This action is mimicked by the application of a 5 ns, 5 MV/m electric pulse. However, fluorescence imaging of chromaffin cells loaded with the fluorescent calcium indicator dye Calcium Green-1 has shown that the calcium responses evoked by a 5 ns pulse outlast those evoked by a nicotinic receptor agonist. Given the short duration and high electric field magnitude of the 5 ns pulse, it is possible that the externally applied electric field can affect internal organelles important for calcium clearance.

Since in chromaffin cells mitochondria are the main organelle involved in the rapid clearing of intracellular calcium following calcium influx through VGCCs, and a disruption of mitochondrial membrane potential has been shown to delay calcium clearance, our first aim was to explore whether 5 ns pulses affect mitochondrial membrane potential using fluorescent mitochondrial membrane potential dyes. Control experiments established that treating the cells with a mitochondrial membrane potential disrupter altered the shape of the calcium responses evoked by nicotinic receptor stimulation. Experiments

next established that in cells in which mitochondria were labeled with mitochondrial membrane potential dyes, cells treated with a mitochondrial membrane potential disrupter caused a decrease in fluorescence, which is indicative of a decrease in mitochondrial membrane potential. When cells were exposed to a single 5 ns, 5 MV/m pulse, no decrease in fluorescence was observed. However, a train of five or ten pulses applied at 10 Hz caused an average decrease of less than 2% in mitochondrial membrane potential fluorescence in approximately 31% and 60% of the cells, respectively. Moreover, a single pulse applied at a higher electric field of 10 MV/m caused an average decrease of less than 2% in mitochondrial membrane potential fluorescence in 44% of the cells, and less than 1.8% in 50% of the cells exposed to a pulse at 15 MV/m. These results suggest that a single 5 ns, 5 MV/m pulse does not affect mitochondrial membrane potential, and that increasing the number of pulses or the electric field magnitude has only minimal effects.

A second aim of the research was to explore if there are differences in the electric field distribution between the two exposure systems used in our laboratory that could explain why calcium responses evoked by a 5 ns pulse varied in duration with each exposure system. Experiments by our group were initially conducted with a gold strip electrode exposure system where cells in suspension were placed between the electrodes on a glass slide. Our current delivery system is comprised of tungsten rod electrodes that are immersed at 45° to the vertical plane into a glass bottom culture dish in which the cells are attached. The tips of the electrodes are placed 40 μm above the bottom of the dish, with the target cell located at the center of the gap between the electrode tips. Although previous simulations performed in our laboratory using a coarse mesh (mesh size of 16 μm) had shown that the electric field was homogenous in the region containing the cell in both

exposure systems, our goal here was to perform refined simulations with higher discretization in the region containing an exposed cell using the Huygens box (mesh size of 4 μm for the tungsten rod exposure system and 1 μm for the gold strip chamber exposure system). The results showed that at 60 MHz, the frequency that encompassed 99% of the pulse's energy, there were only minor differences in the homogeneity of the electric field in the X and Y directions between the tungsten rod and gold strip chambers exposure systems, as well as in other electric field parameters, such as the direction of the electric field. These minor differences are likely not contributing to the different durations of the calcium responses evoked by each exposure system.

In conclusion, a single 5 ns, 5 MV/m pulse produced no detectable effect on the mitochondrial membrane potential in adrenal chromaffin cells. Even multiple pulses and a single pulse applied at higher electric fields caused only an average decrease of less than 2% in fluorescence in a fraction of the cells studied, indicating that 5 ns pulses caused minimal mitochondrial toxicity. This finding indicates that other cellular mechanisms may be affected that will require further investigation, such as inhibitory effects on calcium extrusion, prolonged calcium-induced calcium release (CICR) from the endoplasmic reticulum (ER), and sustained membrane depolarization that may prolong the opening of VGCCs. In addition, our refined simulations showed that despite the very different geometries of the exposure systems, the electric field was homogeneous in the region containing the cell to the same extent, suggesting that other factors may be involved, such as differences in the current density between the electrodes. This and other possibilities will require further simulations.

Dedication

Dedicated to Bhupinder Kaur Bilkhu, Jyoti Singh, and Nuvraj Kaur Bilkhu.

Acknowledgements

I would like to thank first my advisor Dr. Gale Louise Craviso for giving me the opportunity to work in her lab and gain valuable experience in conducting research. I would like to thank my co-advisor Dr. Indira Chatterjee for giving me the opportunity to work with her as well and learn how to use electrical engineering concepts in research.

A big thank you to Dr. Jihwan Yoon for always being available to help when needed and offering discussions with my work.

I heartfelt thank you to Dr. Normand Leblanc for providing helpful feedback and suggestions on my thesis.

I appreciate Dr. Reuben Dagda for his insight on my research and providing feedback on my presentation skills.

I am so thankful for Dr. Lisha Yang for her tremendous help in the laboratory, preparing cells, and for being a great friend.

I would like to thank Marissa Macedo for conducting experiments with electrodes placed at different heights.

I would like to thank Jennifer Li for helping with data analysis.

I would like to thank Robert Terhune for helping with technical issues with the simulations and providing helpful discussions of my numerical modeling results.

I appreciate and am thankful for the help and support from my sister, Nuvraj Bilkhu.

I would like to thank Shehryar Khattak for his support throughout this journey.

This research was supported by the Air Force Office of Scientific Research (AFOSR) Grants: FA9550-12-1-0018, FA9550-12-1-0023 and MURI FA9550-15-1-0517.

Contents

Abstract **i**

Acknowledgements **v**

List of Tables **xii**

List of Figures **xiv**

1 Introduction **1**

1.1 Nanosecond pulses can penetrate the cell interior and cause multiple effects….1

1.2 Bovine Adrenal Chromaffin Cells: Model of Neural Type Cells……2

1.3 Calcium signaling and exocytosis in chromaffin cells……2

1.4 Calcium responses evoked by 5 ns pulses in chromaffin cells are longer lived than those evoked by the physiological stimulus……..4

1.5 Possible mechanisms that could prolong the duration of calcium responses in chromaffin cells exposed to a 5 ns pulse……..6

1.6 Mitochondria: the main organelle involved with the rapid clearance of calcium…….8

1.6.1 Mitochondrial Membrane Potential dyes to study changes in mitochondrial membrane potential……...……...9

1.6.2 NEPs decrease the mitochondrial membrane potential in different cell types……...10

1.6.3 Protonophores cause mitochondrial membrane potential…….12

1.7 Exposure systems to stimulate cells with NEPs……15

1.7.1 Gold strip chamber exposure system……..…….….15

1.7.2 Tungsten rod exposure system……...17

1.8 Refined computations using the Huygens box approach……..19

1.9 Summary of goals…….…20

References…….…….22

2 Experimental Methods 32

2.1 Chromaffin cell isolation and culturing…….……...32

2.2 Preparation of chromaffin cells for experiments…….....33

2.3 Receptor agonist stimulation……34

2.3.1 One cell at a time…….…..34

2.3.2. Dish of cells…….….35

2.4 Stimulating cells with 5 ns pulses…….…36

2.4.1. Tungsten rod electrode fabrication…….……..36

2.4.2 Pulse delivery setup……..38

2.5 Fluorescence imaging of intracellular calcium…….……42

2.6 Fluorescence labeling of mitochondria…….……43

2.7 Monitoring mitochondrial membrane potential…….…...44

2.7.1 Labeling Mitochondria……..44

2.7.2 Perfusion of TMRE and RH 123 labeled cells with CCCP……44

2.7.3 Application of a stimulus to TMRE and RH 123 labeled cells…..….45

2.8 Statistical analysis……45

2.9 Reagents……...46

References……..47

3 Fluorescence imaging of intracellular calcium and mitochondrial membrane potential in chromaffin cells exposed to 5 ns pulses 48

3.1 Introduction……..48

3.2 A single 5 ns pulse evokes longer-lived increases in intracellular calcium compared to the physiological stimulus……..…….…….49

3.3 Disrupting mitochondrial membrane potential alters the calcium response of cells evoked by a depolarizing stimulus…….……54

3.3.1 Effects of CCCP on calcium responses evoked by multiple applications of DMPP……...……54

3.3.2 Effect of FCCP on calcium responses evoked by ten applications of DMPP……58

3.3.3 Effect of CCCP on calcium responses evoked by multiple applications of KCl…….……..59

3.4 Monitoring changes in mitochondrial membrane potential…….…..…61

3.4.1 Fluorescence imaging of mitochondria…….….61

3.5 Assessing TMRE and RH 123 fluorescence for photobleaching……..64

3.6 Monitoring changes in mitochondrial membrane potential in cells treated with CCCP……...64

3.7 Effect of DMPP on TMRE fluorescence……..……69

3.8 Assessing changes in TMRE fluorescence - whole cell fluorescence vs. fluorescence of mitochondrial clusters……..……..71

3.9 Monitoring changes in mitochondrial membrane potential in response to 5 ns pulses……74

3.9.1 Effect of a single 5 ns, 5 MV/m pulse on TMRE fluorescence…...…74

3.9.2 Effect of multiple 5 ns, 5 MV/m pulses on TMRE fluorescence……75

3.9.3 Effect of a single 5 ns pulse at 10 and 15 MV/m on TMRE fluorescence……..……77

3.11 Summary and Conclusions……....79

References……81

4 Numerical modeling methods **84**

4.1 Introduction……..84

4.2 Electric field simulations……..…85

4.3 Fourier transform of the 5 ns electric pulse……..…86

4.4 Geometrical model of the gold strip exposure chamber…….…...87

4.5 Geometrical model of the tungsten rod exposure system……..…89

4.6 Huygens box simulation……...93

4.7 Grid settings……93

4.8 Signal input for a 5 ns pulse numerical simulation……..98

4.9 Computer specifications……...98

4.10 Simulation settings common to both exposure systems……..…99

4.11 Tungsten rod electrode properties……103

4.12 Gold strip electrode properties……103

4.13 Copper strip properties……104

4.14 Extracting Results……105

References……106

5 Numerical modeling results for both exposure systems 109

5.1 Introduction……109

5.2 Area of homogeneity of the electric field distribution in the region containing the cell……113

5.3 Tungsten rod exposure system: control simulations……..114

5.3.1 Tungsten rod exposure system: control simulation with cell dish dimensions in the model matching the dimensions of the cell dish used in experiments……..114

5.3.2 Tungsten rod exposure system: control simulation with reduced cell dish dimensions……117

5.3.3 Comparison of the computed electric field magnitude and direction for the tungsten rod exposure system with the actual cell dish and reduced dimension cell dish……..…120

5.4 Validation of the conversion factor for obtaining the desired electric field magnitude for experiments……...……122

5.5 Tungsten rod exposure system: Electrode tips placed at different heights from the surface of the glass bottom dish……...123

5.5.1 Computed electric field magnitude and direction at the location of a cell when electrode tips are placed 35 μm and 45 μm above the surface of the glass bottom dish……..……..…123

5.5.2 Calcium responses evoked by pulses delivered with electrode tips placed 35 µm and 45 µm above the surface of the glass bottom dish……...127

5.6 Tungsten rod exposure system: Misaligned electrode tips……128

5.7 Homogeneity in the region containing the cell for the tungsten rod exposure system at a single frequency……..130

5.7.1 Tungsten rod electrodes: Computations at 60 MHz……...130

5.8 Gold strip chamber exposure system: Control Simulations……...133

5.9 Homogeneity in the region containing the cell in the gold strip chamber exposure system at a single frequency……134

5.9.1 Gold strip chambers: Computations at 60 MHz…….135

5.10 Summary and Conclusions……..137

References……140

6 Discussion **141**

6.1 Introduction……141

6.2 5 ns pulses have no apparent effect on the mitochondrial membrane potential……..142

6.3 The electric field distribution in the region containing a cell is homogenous to the same degree in each NEP exposure system…….144

6.4 Future directions……146

References……148

List of Tables

Table 1: Comparison of the characteristics of calcium responses evoked by a 5 ns pulse and DMPP…….52

Table 2: Summary of the percent decrease in TMRE fluorescence in response to CCCP……..69

Table 3: Summary of the decrease in TMRE fluorescence in response to 5 ns pulses and DMPP…….79

Table 4: Discretization for each simulation for both exposure systems……..…95

Table 5: Basic components used in creating the geometries in SEMCAD of the two exposure systems…….....99

Table 6: Dielectric properties for each material used in the exposure system models……...……100

Table 7: Settings for the background……...100

Table 8: Settings for the chromaffin cell and BSS for both exposure systems…100

Table 9: Settings for the glass components for both exposure systems……...101

Table 10: Settings for the control 5 ns pulse simulation……..102

Table 11: Settings for tungsten in the tungsten rod electrode exposure system..103

Table 12: Settings for the gold strips in the gold strip exposure chamber……...103

Table 13: Copper strip settings used in gold strip exposure system……104

Table 14: Settings specific to the Huygens box simulations for both exposure systems……..104

Table 15: Characteristics of calcium responses generated by the gold strip chambers and tungsten rod exposure systems……..111

List of Figures

1.1 A cell is composed of a conductive cytoplasm with a dielectric cell membrane……..1

1.2: Calcium signaling in chromaffin cells……..….4

1.3: Schematic diagram of representative calcium responses evoked by a physiological stimulus and a 5 ns pulse…….…….….6

1.4: Mechanisms that can prolong calcium responses evoked by a 5 ns pulse in chromaffin cells……..…….7

1.5: Schematic of calcium uptake by the mitochondria…….……..8

1.6: Structures of CCCP and FCCP……..…….12

1.7: Protonophores disrupt the mitochondrial membrane potential……...13

1.8: Photograph and diagram of the gold chambers used to apply 5 ns pulses……..16

1.9: Diagram of a side view of the cells placed in between the gold electrodes……...17

1.10: Picture of the tungsten rod electrodes immersed in a cell dish during experiments.18

1.11: Diagram of electrode tips positioned over target cell……..…...18

2.1: Stimulation of a chromaffin cell with the physiological stimulus……..…..35

2.2: Photographs of the perfusion setup…….….36

2.3: Photograph of a pair of tungsten rod electrodes used to deliver a 5 ns pulse to chromaffin cells……..37

2.4: Schematic of the 5 ns electric pulse delivery setup……..…38

2.5: Photograph showing the location of the voltage divider with respect to the electrodes…….39

2.6: Photograph of the pulse delivery and fluorescence imaging setup……..…….40

2.7: Photomicrograph showing the location of the target cell between the tungsten rod electrode tips……41

2.8: Representative trace of a 5 ns electric pulse…….……42

3.1: Fluorescence images of a chromaffin cell stimulated with a 5 ns, 5 MV/m pulse…....50

3.2: Calcium responses in chromaffin cells evoked by a single 5 ns pulse…….....50

3.3: Calcium responses of chromaffin cells stimulated with DMPP……..….51

3.4: Calcium responses in cells stimulated with trains of DMPP applications versus trains of 5 ns pulses…….…..53

3.5: Calcium responses in cells treated with CCCP and stimulated with 5 applications of DMPP…….56

3.6: Calcium responses of cells treated with CCCP and stimulated with 10 applications of DMPP…….57

3.7: Calcium responses of cells treated with FCCP and stimulated with 10 applications of DMPP…….59

3.8: Calcium responses in cells treated with 0.5 µM CCCP and stimulated with five applications KCl…….60

3.9: Confocal image of a chromaffin cell in which mitochondria were labeled with 100 nM Mitotracker Green……...…….61

3.10: Fluorescence images of cells in which mitochondria were labeled with mitochondrial labeling dyes……...63

3.11: Photobleaching of TMRE and RH 123 fluorescence……64

3.12: Calcium response to DMPP delivered to the cells by perfusion……...…65

3.13: Schematic diagram showing the procedure used for perfusing Calcium Green-1 labeled cells with CCCP…….…….66

3.14: Fluorescence traces of TMRE and RH 123 labeled-mitochondria during cell perfusion……...……67

3.15: Fluorescence traces of TMRE and RH 123 labeled mitochondira during cell perfusion with 8 µM CCCP…….……..68

3.16: Traces of TMRE fluorescence in cells exposed to ten applications (10 Hz) of DMPP……70

3.17: Analysis of decreases in TMRE fluorescence in response to a stimulus…….……71

3.18: Fluorescence trace corrected for photobleaching……...71

3.19: Analysis of changes in TMRE fluorescence using different regions of interest…….73

3.20: Superimposed fluorescence traces of changes in TMRE analyzed by different methods……..74

3.21: Traces of TMRE fluorescence in cells exposed to a single pulse (5 MV/m)……...75

3.22: Traces of TMRE fluorescence in cells exposed to five pulses……76

3.23: Traces of TMRE fluorescence in response to ten pulses……76

3.24: Calcium responses in cells stimulated with a single 5 ns pulse at 10 MV/m and 15 MV/m72……..……..77

3.25: Traces of TMRE fluorescence in cells exposed to a 5 ns pulse at electric fields great than 5 MV/m……...……..78

4.1: FT of the 5 ns electric pulse……..…87

4.2: Geometry of the gold strip chamber exposure system created in SEMCAD……...….89

4.3: Geometry of the tungsten rod exposure system created in SEMCAD…….....91

4.4: Geometry of the tungsten rod exposure system created in SEMCAD showing a view of the electrode tips with respect to the cell……..…….92

4.5: Discretization of a cell in the gold strip chamber exposure system for the Huygens box simulations……...……94

4.6: Discretization of the cell in the tungsten rod exposure system for the Huygens box simulations……..95

4.7: Initial computational and the Huygens box computational domain that was used for each simulation……...97

5.1 Comparison of calcium responses evoked by each exposure system……..…110

5.2: Diagram of the axes showing the planes at which contour plots were extracted in SEMCAD……112

5.3: Homogeneity in the electric field magnitude was calculated by volume with the cell centered in the region……..114

5.4: Computed electric field magnitude distribution for the tungsten rod exposure system with the cell dish dimensions matching the actual dish size used in experiments.....116

5.5: Vector plot showing the direction of the electric field distribution in the Y plane…..116

5.6: Surface plot of the computed electric field magnitude in a plane normal to the Z axis for the tungsten rod exposure system……....117

5.7: Computed distribution of the electric field magnitude for the tungsten rod exposure system with reduced cell dish dimensions……..118

5.8: Vector plot showing the direction of the electric field distribution in the Y plane with reduced cell dish dimensions…….….119

5.9: Surface plot of the computed electric field magnitude in a plane normal to the Z axis for the tungsten rod exposure system……....119

5.10: Comparison of the computed distribution of the electric field in the tungsten rod simulations using different cell dish sizes…….121

5.11: The computed electric field magnitude is 5 MV/m in the tungsten rod simulations using different cell dish sizes……...…….121

5.12: Electric field magnitudes of 10 MV/m and 15 MV/m correlate with the conversion factor……...…..123

5.13: Computed electric field for tungsten rod electrode tips placed 35 µm above the surface of the glass bottom dish……..……..124

5.14: Vector plot showing the direction of the electric field distribution in the Y plane with electrodes placed 35 µm above the glass bottom dish……...125

5.15: Computed electric field for tungsten rod electrode tips placed 45 µm above the surface of the glass bottom dish……..…….126

5.16: Vector plot showing the direction of the electric field distribution in the Y plane with electrodes placed 45 µm above the glass bottom dish…….…126

5.17: Calcium responses in chromaffin cells stimulated with a 5 ns pulse when the tungsten rod electrode tips were placed at two different heights above the surface of the glass bottom dish……...…128

5.18: Computed electric field for misaligned tungsten rod electrode tips…….…129

5.19: Vector plot showing the direction of the electric field distribution in the Y plane with misaligned electrode tips……..……..129

5.20: Computed distribution of the electric field magnitude for the tungsten rod exposure system at 60 MHz along the X, Y, Z directions……132

5.21: Vector plot showing the direction of the electric field distribution in the X, Y, and Z planes at 60 MHz for the tungsten rod exposure system in the region containing the cell…….……..133

5.22: Electric field magnitude and direction within the gold strip chamber exposure system……...134

5.23: Computed distribution of the electric field magnitude for the gold strip chamber exposure system at 60 MHz along the X, Y, Z directions……...……..….136

5.24: Vector plot showing the direction of the electric field distribution in the X, Y, and Z planes at 60 MHz for the gold strip chamber exposure system in the region containing the cell……...…….137

5.25: Comparison of the distribution of the electric field magnitude for the gold strip chamber and tungsten rod exposure systems at 60 MHz along the X, Y, Z directions…….138

5.26: Comparison of the vector plots of the electric field in both exposure systems…….139

APPENDIX 1: Copyright permission to use Mitotracker Green labeled chromaffin cell 152

Chapter 1: Introduction

1.1 Nanosecond pulses can penetrate the cell interior and cause multiple effects

Nanosecond electric pulses (NEPs) have been shown to influence cellular behavior in different cell types by inducing a voltage across the cell membrane [1-2]. This occurs due to the accumulation of electric charges at the cell membrane from the resulting current, which can be perceived by viewing the cell as an electrical model with a conductive cellular cytoplasm surrounded by a dielectric cell membrane (Figure 1.1) [1-2].

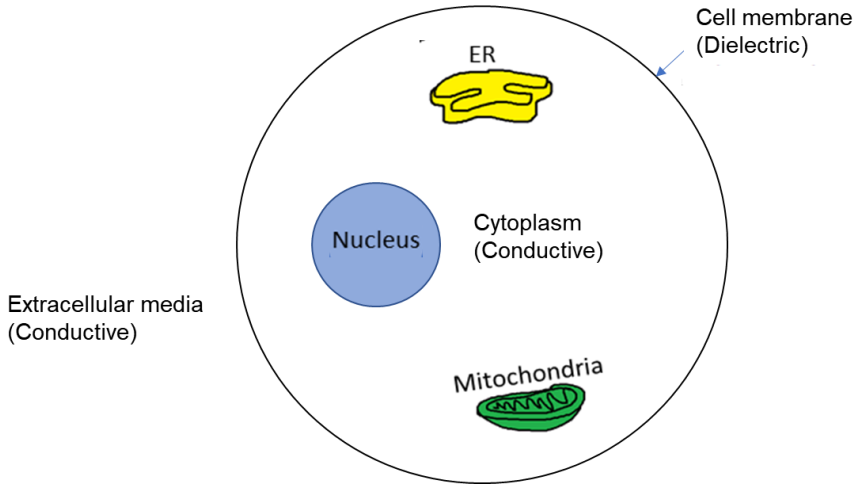

Figure 1.1 A cell is composed of a conductive cytoplasm with a dielectric cell membrane. The diagram shows a circular cell model with a conductive interior containing the endoplasmic reticulum (ER), the nucleus, and mitochondria, surrounded by a dielectric plasma membrane bathed in conductive media.

Furthermore, NEPs, due to their short duration, can penetrate the cell membrane where they can cause intracellular effects [1-2]. The best documented effect is the release of calcium from the endoplasmic reticulum (ER) caused by a 60 ns pulse applied to Jurkat cells at an electric field from 2.5-5 MV/m [3], a 60 ns pulse applied to HL-60 cells (1.5 MV/m) [4], and in chromaffin cells at high electric fields [5]. Other effects include, for

example, changes in the mitochondrial membrane potential [6-7], activation of caspase [8] and disruption in actin assembly within the cytoskeleton [9]. As discussed in the next section, our studies use adrenal chromaffin cells, a well characterized neural-cell type, to understand the effects of 5 ns electric pulses on cellular function.

1.2 Bovine Adrenal Chromaffin Cells: Model of Neural Type Cells

Adrenal chromaffin cells, like sympathetic neurons, originate from the neural crest, which is found at the dorsal surface of the embryonic neural tube [11-12]. Anatomically, adrenal chromaffin cells are found in the inner medulla of adrenal glands that are located on top of the kidneys. Chromaffin cells are excitable and upon stimulation release the catecholamines norepinephrine and epinephrine, which are involved in the "fight or flight" response, via calcium-dependent exocytosis. As such, these cells serve as a model system for studies of stimulus-secretion. The advantages of using chromaffin cells are that a single bovine adrenal gland yields millions of cells that are easy to maintain in culture [13-14]. In addition, chromaffin cells maintain a round morphology in culture, which facilitates cell modeling [5, 15]. Lastly, these cells have been well characterized in terms of various cellular mechanisms such as calcium signaling and exocytosis, which is discussed in the next section.

1.3 Calcium signaling and exocytosis in chromaffin cells

In vivo, chromaffin cells are activated when the neurotransmitter, acetylcholine, is released from the splanchnic nerve terminal and binds to ligand-gated nicotinic cholinergic

receptors, which are Na^+ channels located in the plasma membrane. This causes an influx of Na^+ that depolarizes the cell membrane resulting in the activation of voltage-gated calcium channels (VGCCs) through which calcium enters the cell. The influx of calcium causes a rapid rise in intracellular calcium at sites where exocytosis occurs, forming a high calcium microdomain between the mitochondria located near the cell membrane and the ER, causing calcium-induced calcium release (CICR) from the ER that in turn refines the exocytosis process.

The process of exocytosis involves calcium-dependent fusion of the catecholamine-containing secretory granules with the cell membrane, whereby the calcium trigger for exocytosis is the protein synaptotagmin [16-17]. To terminate exocytosis, calcium is cleared rapidly by mitochondria so that the cell can respond to the next stimulus. Ultimately, calcium is extruded from the cell through the Na^+/Ca^{2+} exchanger and plasmalemmal calcium ATPase (PMCA). These mechanisms are shown schematically in Figure 1.2.

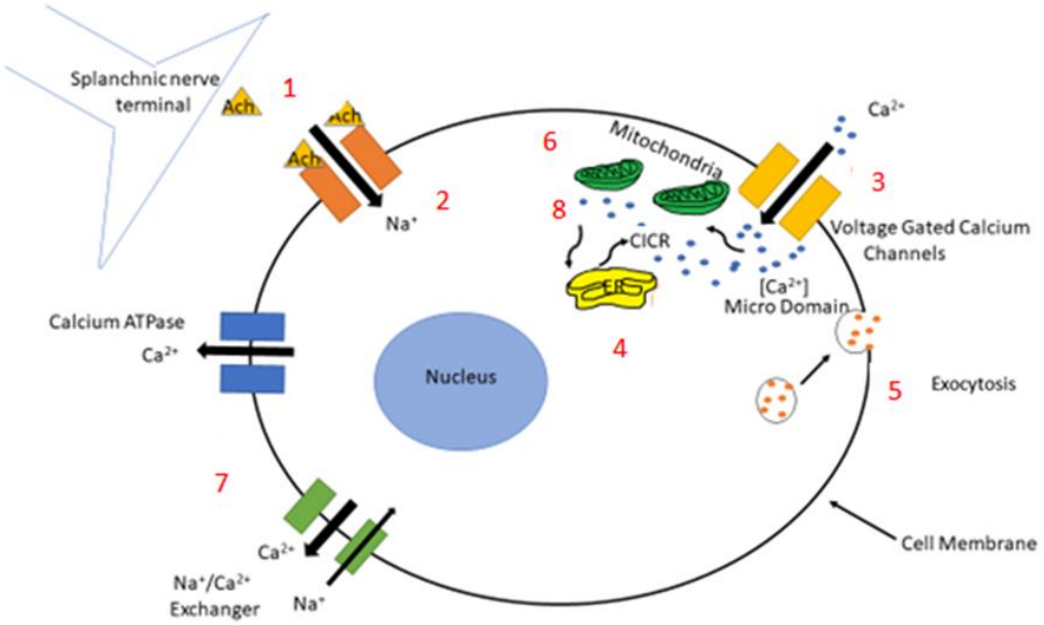

Figure 1.2: Calcium signaling in chromaffin cells. 1) Acetylcholine (Ach) binds to the nicotinic receptor (orange). 2) Binding of Ach causes influx of Na^+ that depolarizes the cell membrane. 3) Voltage-gated calcium channels (VGCCs) are activated allowing influx of calcium that forms high calcium microdomains between the mitochondria, ER, and the VGCCs. 4) The high calcium near the ER causes CICR. 5) The rise in intracellular calcium evokes exocytosis of epinephrine and norepinephrine. 6) Mitochondria rapidly take up calcium to terminate the signal. 7) Calcium is extruded from the cell through the Na^+/Ca^{2+} exchanger (green) or plasma membrane calcium ATPase (blue). 8) Calcium is extruded from the mitochondria through its own Na^+/Ca^{2+} exchanger, which replenishes calcium stores in the ER.

1.4 Calcium responses evoked by 5 ns pulses in chromaffin cells are longer lived than those evoked by the physiological stimulus

Our laboratory has shown using fluorescence imaging of intracellular calcium in adrenal chromaffin cells that a single 5 ns, 5 MV/m pulse mimics the physiological stimulus by causing influx of Na^+ , which depolarizes the cell membrane [5, 18-20]. This

in turn causes activation of VGCCs and calcium influx [5,18-21]. Interestingly, however, the rise in intracellular calcium is longer lived than that evoked by the physiological stimulus. This difference was observed regardless of how the cells are exposed to a 5 ns pulse.

Two different types of exposure systems have been used to expose chromaffin cells to 5 ns electric pulses. The exposure system first used by our group was a gold strip chamber exposure system in which cells in suspension were placed between two gold strips that served as electrodes [22]. A 5 ns pulsed delivered with this system evoked calcium responses in which there was a rapid rise in intracellular calcium, but when compared to the physiological stimulus took slightly longer to return to pre-stimulus calcium levels. That is, cells exposed to a 5 ns pulse evoked calcium responses that recovered to pre-stimulus calcium levels with an average half-width of 8.6 s [19], half-width being the time interval for intracellular calcium to decline to 50% of the maximal value. In contrast, in cells exposed to a brief application of a nicotinic receptor agonist, the half-width of the rise in intracellular calcium was ~5-6 s [5]. More recent experiments conducted in our laboratory (by Dr. Josette Zaklit, University of Nevada, Reno) reproduced the results obtained with the gold strip chamber exposure system.

Due to limitations in conducting various experiments with this exposure system, such as the inability to allow for perfusion of the cells, or to carry electrophysiological experiments such as patch clamp, our group began using an exposure system commonly employed by other laboratories that would allow for these types of experiments. Essentially, a 5 ns pulse is delivered to single attached cells by a pair of tungsten rod electrodes [10, 23-27]. We found that a 5 ns pulse evoked more prolonged calcium

responses compared not only to the physiological stimulus, but also to those evoked when using the gold strip chamber exposure system. Now the half-width of the calcium responses was 23 s or greater. Figure 1.3 is a schematic representation of the differences in the duration of the calcium responses evoked in each case.

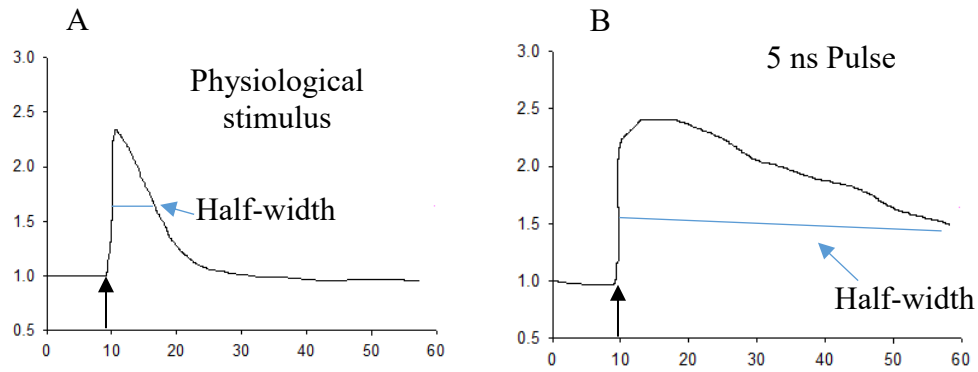

Figure 1.3: Schematic diagram of representative calcium responses evoked by a physiological stimulus and a 5 ns pulse. A) A single application of a nicotinic receptor agonist causes a rapid rise in intracellular calcium that rapidly returns to pre-stimulus calcium levels. B) Application of a 5 ns pulse using the tungsten rod exposure system evokes a rapid rise in intracellular calcium that takes much longer to return to pre-stimulus calcium levels. Diagrams are based on results from [11]. Arrows indicate when the stimulus was applied.

Section 1.7 gives more details about each exposure system.

1.5 Possible mechanisms that could prolong the duration of calcium responses in chromaffin cells exposed to a 5 ns pulse

As stated previously, chromaffin cells must clear intracellular calcium in order to prevent calcium overload and to be prepared to respond to the next stimulus. Long lived calcium responses evoked by a 5 ns pulse could mean that one or more of the following calcium clearing mechanisms may be affected: calcium uptake by mitochondria, and/or a

reduction in the activity of the plasma membrane calcium ATPase (PMCA), and the Na^+/Ca^{2+} exchanger. In addition to these mechanisms, other mechanisms may also be impacted that may delay calcium clearance such as: sustained CICR from the ER and sustained activation of VGCCs due to prolonged membrane depolarization. These possibilities are schematically shown in Figure 1.4. For this thesis, the focus is on assessing the effect of a 5 ns pulse on the main organelle involved in calcium clearance in adrenal chromaffin cells, the mitochondria.

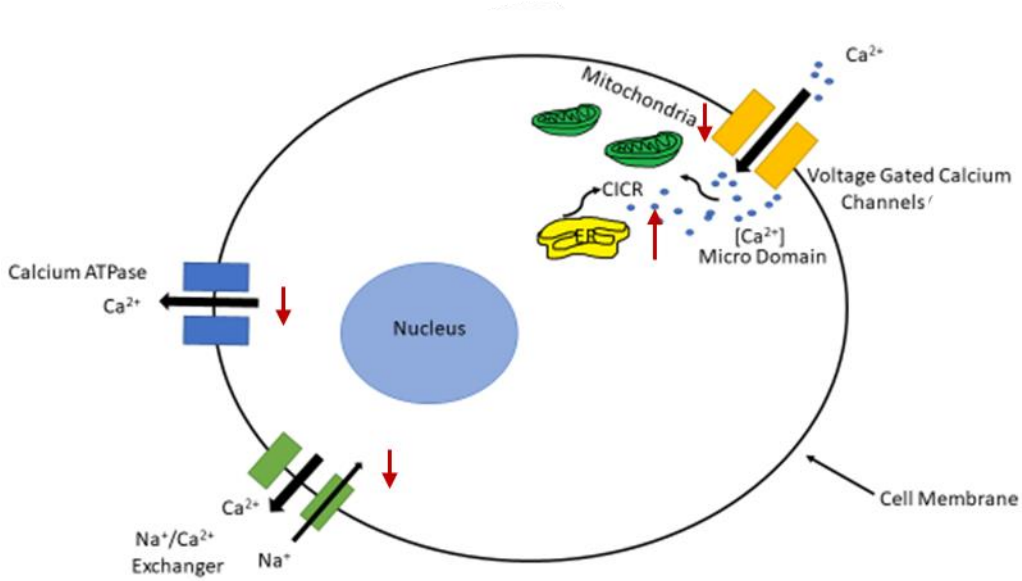

Figure 1.4: Mechanisms that can prolong calcium responses evoked by a 5 ns pulse in chromaffin cells. Calcium clearance mechanisms: rapid clearance by the mitochondria and calcium extrusion through the plasma membrane Na^+/Ca^{2+} exchanger and the plasma membrane calcium ATPase. Prolonged CICR from the ER. Sustained membrane depolarization that may keep VGCCs remain open after a pulse. Upright arrows indicate an increase and arrows facing down indicate a decrease.

1.6 Mitochondria: the main organelle involved with the rapid clearance of calcium

Calcium signaling is imperative for cellular function and communication, which plays an imperative role in stimulus-secretion coupling in chromaffin cells [27, 29-30]. As already mentioned, depolarization of a chromaffin cell causes calcium influx into the cell and the calcium is rapidly taken up by mitochondria [29-37]. Mitochondria take up calcium ions through the mitochondrial calcium uniporter protein (MCU), which is dependent on the mitochondrial membrane potential (the electrochemical gradient of protons across the inner mitochondrial membrane potential) for proper function and maintained by the electron transport chain [29-38]. Figure 1.5 shows a schematic of calcium uptake by the mitochondria.

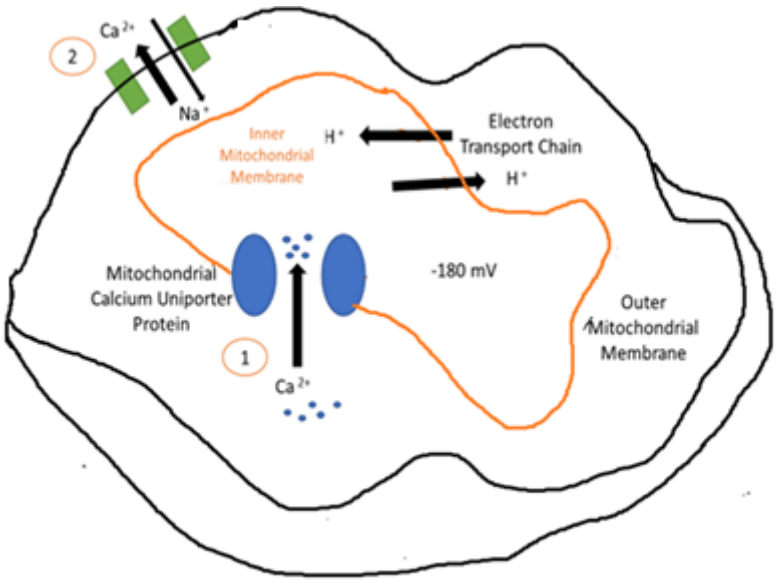

Figure 1.5: Schematic of calcium uptake by the mitochondria. The mitochondria at rest stores little to no calcium. The mitochondrial membrane potential is maintained by the electron transport chain and is the driving force behind 1) calcium uptake through the mitochondrial calcium uniporter protein. 2) Calcium is extruded from the mitochondria through a Na^{+}/Ca^{2+} exchanger.

As previously shown in Figure 1.2, the mitochondria extrude calcium through the antiport Na^+ and Ca^{2+} exchanger at the end of a stimulus. The released calcium in turn replenishes calcium stores in the ER [29-38]. Inhibiting or disrupting mitochondrial function by altering mitochondrial membrane potential can delay intracellular calcium clearance, which is being investigated in this study as the mechanism underlying the long-lived calcium responses evoked by 5 ns pulses.

1.6.1 Mitochondrial Membrane Potential dyes to study changes in mitochondrial membrane potential

Changes in mitochondrial membrane potential have been studied by labeling mitochondria with mitochondrial membrane potential dyes. For the purpose of only visualizing the mitochondria, Mitotracker Green is the recommended dye as it labels the global mass population of the mitochondria in a cell by labeling both living and dead mitochondria. Labeling occurs by forming covalent bonds to proteins inside the inner mitochondrial membrane [39-41]. The dyes Mitotracker Orange, Tetramethylrhodamine, Ethyl Ester, Perchlorate (TMRE), and Rhodamine 123 (RH 123) in contrast label only actively respiring mitochondria in a cell [39]. These dyes are cationic and readily accumulate inside the mitochondria due to the overall electro-negative charge caused by the mitochondrial membrane potential. TMRE is the more sensitive dye that is recommended for monitoring changes in mitochondrial membrane potential, followed by

RH 123 and Mitotracker Orange, with the concentration of each dye that is optimal experiments being cell dependent [39]. When there is a change in the mitochondrial membrane potential, there is a decrease in fluorescence that results from dye molecules being released from the mitochondria [39]. For validation of experimental results, typically more than one dye is used. However, it should be noted that these dyes are limited to qualitative rather than quantitative evaluation of changes in the mitochondrial membrane, especially in our studies where monitoring changes in fluorescence is carried out using wide field fluorescence microscope [39-45].

1.6.2 NEPs decrease the mitochondrial membrane potential in different cell types

Studies of the effects of NEPs that have focused on cell viability in relation to the mitochondrial membrane potential have shown that NEPs can cause disruption in the mitochondrial membrane potential in different cell types. In one study, Jurkat cells labeled with TMRE showed that a 600 ns pulse at electric fields ranging from 40 kV/cm to 80 kV/cm caused a decrease in TMRE fluorescence, hence a change in the mitochondrial membrane potential [46]. Another study focused on the viability of cancer cells and possible cancer ablation techniques using N1-S1 hepatocellular carcinoma cells labeled with TMRE. In that study it was found that a 600 ns pulse at electric fields higher than 50 kV/cm caused a decrease in TMRE fluorescence (~ 25%), and hence mitochondrial membrane potential disruption [6]. Another study focusing on the effects of NEPs on cancer ablation showed that U87 glioblastoma cells labeled with TMRM exposed to 100, 10 ns pulses at a repetition rate of 10 Hz showed a decrease of 30% in TMRM

fluorescence, and hence a disruption in mitochondrial membrane potential [9]. In addition, these authors showed that mitochondrial membrane potential disruption occurred in a dose-dependent manner where more pulses caused a larger decrease in TMRM fluorescence [9]. Moreover, changes in mitochondrial fluorescence were still evident 30 minutes after exposure to NEPs, suggesting that there are long-term effects of NEPs on the mitochondria [9]. Another study focusing on the effects of NEPs on mitochondrial membrane potential in wild-type Jurkat T-lymphocytes (clone A3) labeled with TMRE showed that disruption of the mitochondrial membrane potential was electric field-dependent, with a maximum decrease of 20% in fluorescence at electric fields higher than 30 kV/cm [49]. Another study conducted in real-time to determine the effects of NEPs on mitochondrial membrane potential in Jurkat cells labeled with TMRE and RH 123 also showed that disruption of the mitochondrial membrane potential was dependent of the electric field and the number of applied pulses (<10% decrease in TMRE fluorescence observed 30 seconds and three minutes after application of ten pulses) [7]. As a positive control, TMRE and RH 123 labeled cells were treated with 20 μM carbonyl cyanide 3-chlorophenylhydrazone (CCCP), a mitochondrial membrane potential disrupter, to correlate the decrease in fluorescence signal with mitochondrial membrane potential (discussed in the following section). Taken as a whole, these findings suggest that NEPs can affect the mitochondrial membrane potential, which is one of the aims of this thesis.

1.6.3 Protonophores cause mitochondrial membrane potential

In order to establish that a decrease in TMRE/RH 123 fluorescence signal correlates with mitochondrial membrane potential disruption, it is customary to expose TMRE or RH 123 labeled cells to CCCP or the related compound carbonyl cyanide-4-(trifluoromethoxy)phenylhydrazone (FCCP) [39]. This treatment provides a fluorescence signal that decreases, indicating mitochondrial membrane potential disruption [39]. Multiple studies have shown that the decrease in TMRE or RH 123 labeled cells is usually dependent on the concentration of CCCP or FCCP, where higher concentrations cause a larger decrease in fluorescence, and hence greater mitochondrial membrane potential disruption [45, 46-48, 50]. The structures CCCP and FCCP are shown in Figure 1.6.

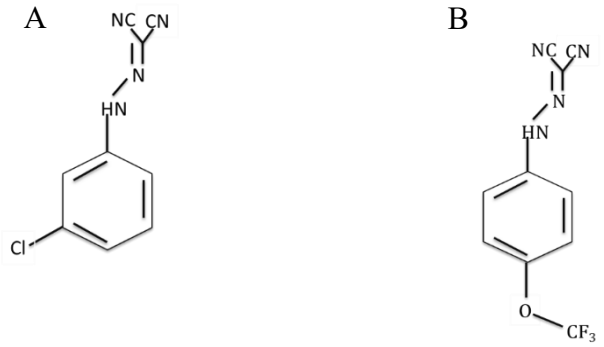

Figure 1.6: Structures of CCCP and FCCP. A) CCCP has a Cl^- attached to the benzene ring. B) FCCP has a CF_3 attached to its benzene ring.

CCCP has a Cl^- atom linked to its benzene ring whereas FCCP has a CF_3 molecule. Both protonophores function in the same manner to disrupt the mitochondrial membrane potential. That is, both readily intercalate into both the inner and outer mitochondrial membranes, inducing the formation of pores, and introducing protons into the inner

mitochondrial membrane [51-52]. The accumulation of extra protons in the inner mitochondrial membrane collapses the electron transport chain causing a change in the voltage of the mitochondrial membrane potential, which hinders the MCU from taking up calcium ions. This causes a string of events linked to changes in the mitochondrial membrane potential such as disruption of the MCU protein, delay of intracellular calcium clearance, disruption in ATP production, and production of reactive oxygen species (ROS) [51-52]. The schematic in Figure 1.7 shows the effect of CCCP on mitochondrial membrane potential by importing protons.

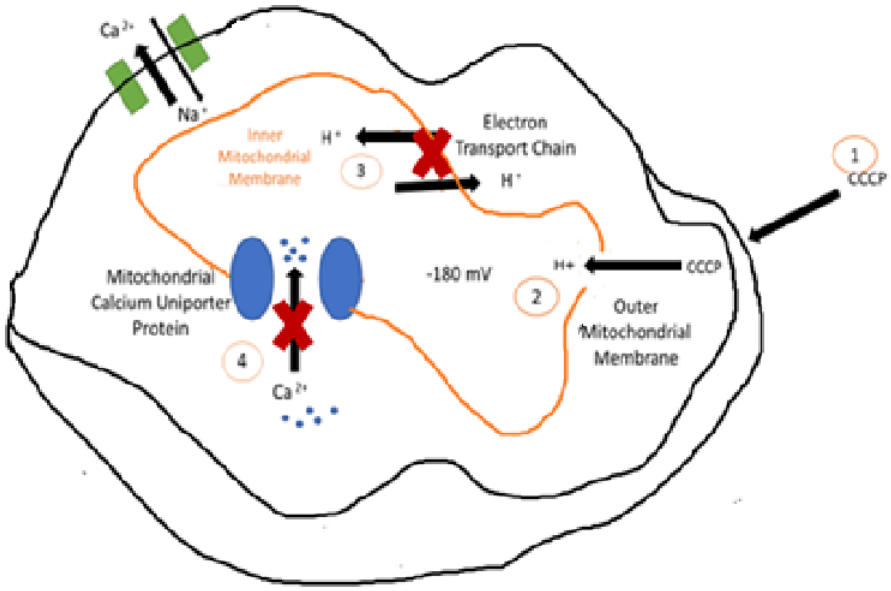

Figure 1.7: Protonophores disrupt the mitochondrial membrane potential. Protonophores (i.e. CCCP) import protons into the inner mitochondrial membrane, collapsing the electron transport chain and the mitochondrial membrane potential.

It is worth noting that the effects of CCCP are not limited to disrupting the mitochondrial membrane potential. Previous studies have shown that FCCP and CCCP at concentrations higher than 10 µM can permeabilize the plasma membrane and cause

multiple effects such as ATP disruption, immediate reduction of the calcium current, which in turn inhibits ATP disruption, changes in the pH gradient, and ROS production [34, 37, 39]. Regarding chromaffin cells, a study has shown that CCCP can cause disruption of the pH gradient, and release of catecholamines from granules [50-53]. In addition, a concentration of 2 μM CCCP was shown to cause an inhibition of the calcium current, which may be a secondary cause of ATP synthesis disruption and inhibiting processes that require ATP (such as calcium ATPases) [54]. A concentration of 1 μM CCCP was shown to cause mitochondrial membrane potential disruption, and thereby induce a rise in intracellular calcium [37]. Furthermore, studies have shown that doubling the concentration of CCCP (>1 μM) usually doubles the dissipation effect on the mitochondrial membrane potential in a dose-dependent manner [39, 47, 52]. However, cells treated with CCCP do not always show an increase in intracellular calcium levels. In fact, CCCP treated bovine chromaffin cells have shown calcium responses with a decrease in calcium amplitude [55]. These findings suggest that cells have variable responses in increase in intracellular calcium after being treated with protonophores, which may be due to multiple mechanisms being affected. However, it has been suggested that in order to see a larger affect in mitochondrial membrane potential disruption and a rise in intracellular calcium, a stronger or more prolonged stimulus is required [55]. This suggests that providing a small or short-lived stimulus to CCCP/FCCP treated cells may not always show a sustained rise in intracellular calcium from mitochondrial membrane potential disruption [55]. Overall, CCCP and FCCP have been shown to alter calcium responses in chromaffin cells.

1.7 Exposure systems to stimulate cells with NEPs

1.7.1 Gold strip chamber exposure system

As stated earlier, previous experiments in our laboratory were conducted using a gold chamber exposure system to expose chromaffin cells to 5 ns electric pulses. The gold strip chamber exposure system was fabricated as described in [56] but using gold strips as described in [22]. It is composed of a rectangular glass slide measuring 75 mm in length and 25 mm in width. Two gold strips were deposited onto the slide with a length of 40 mm, 5 mm wide, and a thickness of 25 µm, separated 100 µm apart from each other. The cells were located in suspension between the electrodes in a total volume of BSS of 3 µl. A square glass coverslip was placed over the gap between the electrodes for experiments. Figure 1.8 shows a photograph and a diagram of the gold strip chamber. Figure 1.9 shows a diagram of a cell placed between the electrodes and a contour slice of the electric field distribution normal to the Z plane showing that the region containing the cell is exposed to a uniform electric field.

As stated earlier, chromaffin cells exposed to a 5 ns pulse with this exposure system had calcium responses that were longer-lived compared to those evoked by a physiological stimulus. More recent experiments conducted in our laboratory using the gold strip chamber exposure system showed results that were consistent with those obtained previously in that calcium had a half-width of ~11s. Simulations performed in [20] showed that the electric field distribution was homogeneous in the region containing the cell. The electric field in this system could be calculated by using the following equation (1)

$$E=\frac{V}{D} \tag{1}$$

where E is the electric field magnitude (V/m), V is the applied voltage (V), and D is the distance between the electrodes (m). This relation shows that increasing the voltage and decreasing the distance between the two electrodes increases the electric field.

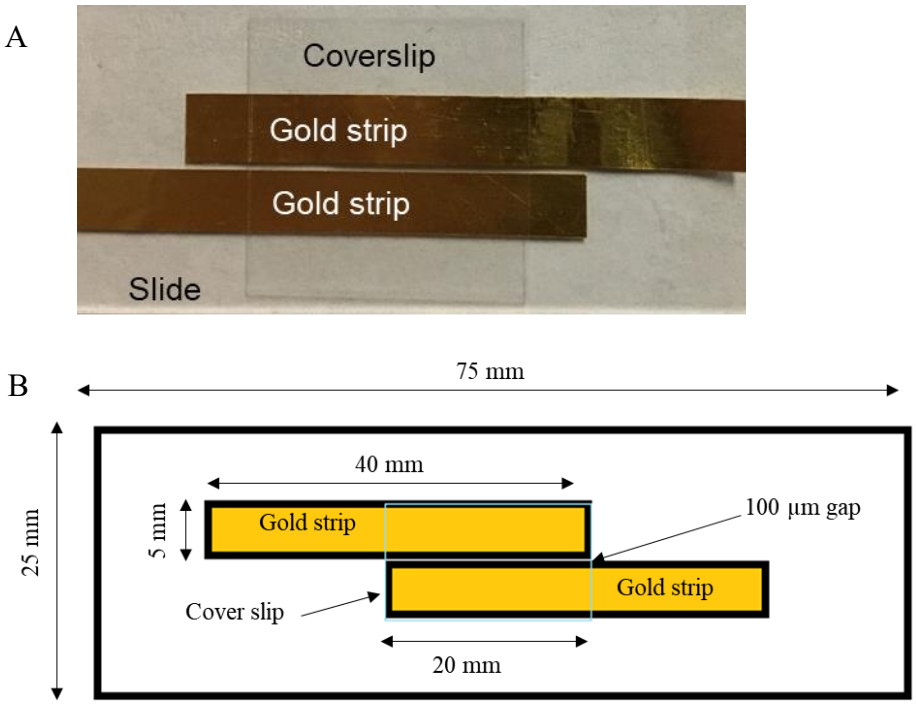

Figure 1.8: Photograph and diagram of the gold chambers used to apply 5 ns pulses. A) Gold chamber exposure system used in experiments. B) Diagram of the dimensions of the glass slide, gold electrodes, and cover slip.

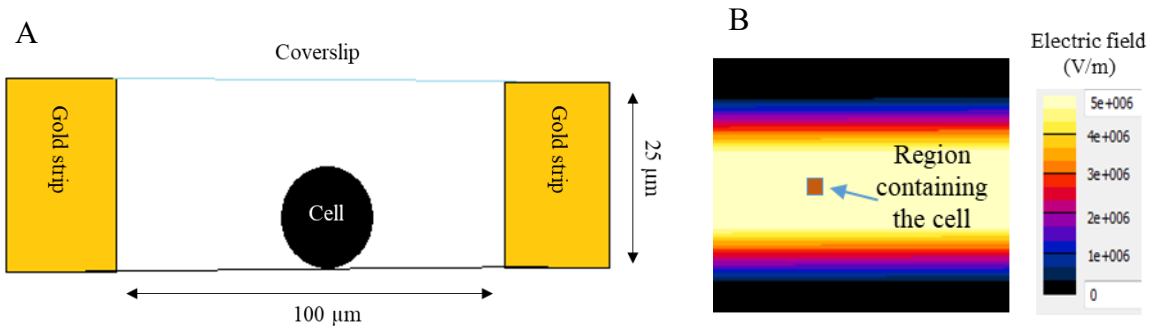

Figure 1.9: Diagram of a side view of the cells placed in between the gold electrodes. The total volume of the balanced salt solution between the electrodes was 3 µl. A) A side view of the cell placed between the gold electrodes. B) A contour slice of the electric field distribution normal to the Z axis generated by using the software package SEMCAD (version 14.8.5, SPEAG, Zurich, Switzerland) shows that the region containing the cell is exposed to a uniform electric field of 5 MV/m.

1.7.2 Tungsten rod exposure system

Our current exposure system is a tungsten rod exposure system commonly used by other groups to study the effects of NEPs on cells [24-27]. The electrodes consist of two cylindrical gold-plated tungsten rods (127 µm diameter) spaced 100 µm apart from each other. Details of how the electrodes are fabricated are given in Chapter 2. The electrode tips are placed 40 µm above a glass bottom dish in which chromaffin cells are attached. They are positioned 45° to the vertical plane, with a target cell located centrally between the electrode tips. Cells are exposed in a total volume of balanced salt solution of 2 ml. Figure 1.10 shows a photograph of a pair of tungsten rod electrodes placed in a cell dish used in our experiments. Figure 1.11 shows a diagram of the tungsten rod electrode tips positioned near a target cell and a contour slice of the electric field distribution normal to the Z plane showing that the region containing the cell is exposed to a uniform electric

field. Details about how the simulations were performed in our laboratory using are given in Chapter 2.

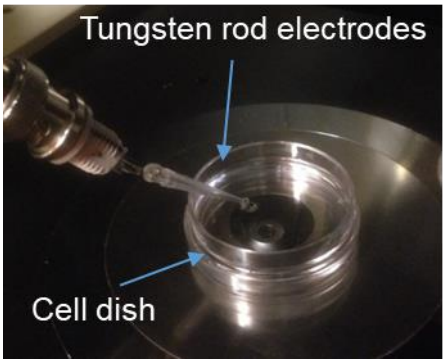

Figure 1.10: Picture of the tungsten rod electrodes immersed in a cell dish during experiments. The cell dish has a total volume of 2 ml of the balanced salt solution.

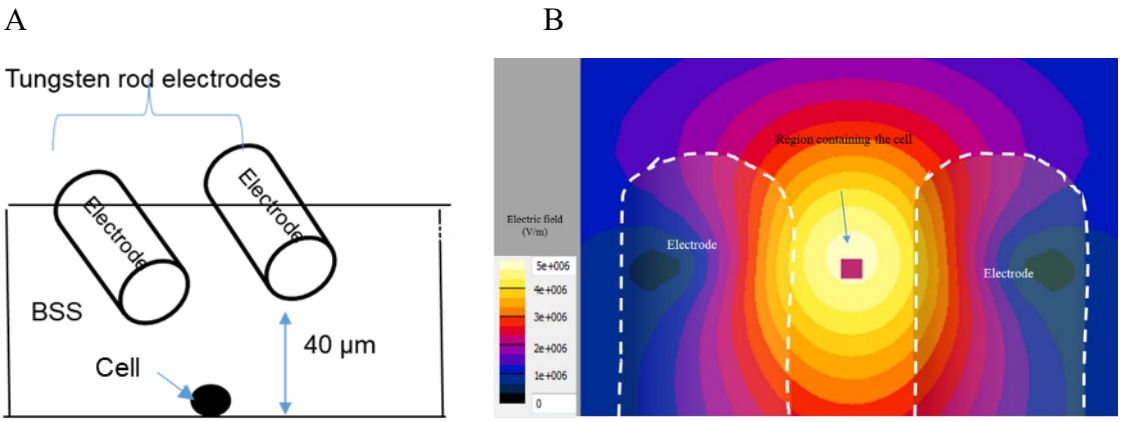

Figure 1.11: Diagram of electrode tips positioned over target cell. A) The electrode tips face towards the target cell. B) A contour slice of the electric field normal to the Z plane generated using SEMCAD shows that the region containing the cells is exposed to a uniform electric field of 5 MV/m.

As stated above, calcium responses evoked by the two exposure systems are different in that the rise in intracellular calcium in cells exposed to a 5 ns pulse using the tungsten rod exposure system is much longer in duration that that that found for cells

exposed to 5 ns pulses using the gold chamber exposure system. Although previous simulations in our laboratory have shown that the electric field distribution in the region containing the cell in both exposure systems was homogeneous [5, 57], the two exposure systems nevertheless differ in their geometries and in other characteristics, such as the volume of balanced salt solution surrounding the cell. In this thesis, we will conduct refined simulations of the electric field in the region containing the cell in both exposure systems using the Huygens box approach.

1.8 Refined computations using the Huygens box approach

The electric field distribution will be computed by SEMCAD using the FDTD method, which computes electromagnetic equations for 3D geometries [58-62]. Homogeneity in the electric field of any exposure system is required for reproducibility of biological results, with a recommendation that the homogeneity of the electric field be constant in the location of the target cell but can be within 30% over a larger distance (such as 100 μm), since absolute homogeneity in an exposure system is difficult to achieve [63]. Refined computations of the electric field will obtained using the Huygens box approach with reduced simulation time to assess differences in the electric field magnitude between the two exposure systems[64]. For example, to complete a simulation with a discretization step size of 4 μm without the Huygens box, the time to complete the simulation was 138 hours. However, with the Huygens box, the simulation time was reduced to 27 hours. We will be using this method to compute homogeneity in the electric field in the region containing the cell because the Huygens box is preferred over a highly discretized simulation, which is imperative for providing refinement by reducing simulation time

As described in this thesis, the simulations required a total of two simulations for a single completed Huygens box simulation. The first simulation computes the electric field in the initial computational domain with a coarse mesh (minimum mesh size of 16 μm). This is followed by a Huygens box computational domain, which is smaller in area compared to the initial computational domain, has finer discretization (minimum mesh size of 1 μm), uses the computed results from the first simulation as input, and decreases the simulation time significantly [64-68]. The overall goal of is to assess the differences in the electric field between the two exposure systems that could account for the different calcium responses.

1.9 Summary of goals

Aa 5 ns, 5 MV/m pulse mimics the physiological stimulus by evoking a rapid rise in intracellular calcium that is longer in duration than that evoked by physiological stimulus. One of the aims of this thesis is to determine whether the electric field penetrates the cell interior and disrupts the mitochondrial membrane potential. Our approach involves labeling mitochondria with fluorescent mitochondrial membrane potential dyes and monitoring changes in fluorescence in cells exposed to 5 ns pulses in real time.

A second aim of this thesis focuses on potential differences in the electric field distribution in the region containing the cell in the two exposure systems used in our laboratory. We approached this by conducting refined simulations of the electric field in the region containing the cell.

This thesis addresses these two questions by discussing the Experimental methods in Chapter 2, Experimental results in Chapter 3, Numerical modeling methods in Chapter 4, Numerical modeling results in Chapter 5, and ending with the Conclusion and Future works in Chapter 6.

References:

[1] K. Schoenbach, B. Hargrave, R. Joshi, J. Kolb, R. Nuccitelli, C. Osgood, A. Pakhomov, M. Stacey, R. Swanson, J. White, S. Xiao, J. Zhang, S. Beebe, P. Blackmore, and E. Buescher, "Bioelectric Effects of Intense Nanosecond Pulses," *IEEE Transactions on Dielectrics and Electrical Insulation*, vol. 14, no. 5, pp. 1088–1109, 2007.

[2] K. H. Schoenbach, S. J. Beebe, and E. S. Buescher, "Intracellular Effect of Ultrashort Electrical Pulses," *Bioelectromagnetics*, vol. 22, no. 6, pp. 440–448, 2001.

[3] S. S. Scarlett, J. A. White, P. F. Blackmore, K. H. Schoenbach, and J. F. Kolb, "Regulation of Intracellular Calcium concentration by Nanosecond Pulsed Electric Fields," *Biochimica et Biophysica Acta (BBA) - Biomembranes*, vol. 1788, no. 5, pp. 1168–1175, 2009.

[4] S. J. Beebe, P. F. Blackmore, J. White, R. P. Joshi, and K. H. Schoenbach, "Nanosecond Pulsed Electric Fields modulate Cell function through Intracellular Signal Transduction Mechanisms," *Physiological Measurement*, vol. 25, no. 4, pp. 1077–1093, 2004.

[5] J. Zaklit, G. L. Craviso, N. Leblanc, L. Yang, P. T. Vernier, and I. Chatterjee, "Adrenal Chromaffin Cells Exposed to 5-ns Pulses Require Higher Electric Fields to Porate Intracellular Membranes than the Plasma Membrane: An Experimental and Modeling Study," *The Journal of Membrane Biology*, vol. 250, no. 5, pp. 535–552, 2017.

[6] S. J. Beebe, Y.-J. Chen, N. M. Sain, K. H. Schoenbach, and S. Xiao, "Transient Features in Nanosecond Pulsed Electric Fields Differentially Modulate Mitochondria and Viability," *PLoS ONE*, vol. 7, no. 12, 2012.

[7] Napotnik, T., Wu, Y., Gundersen, M., Miklavčič, D. and Vernier, P. (2011). Nanosecond Electric Pulses cause Mitochondrial Membrane Permeabilization in Jurkat cells. *Bioelectromagnetics*, 33(3), pp.257-264.

[8] W. Ren, N. M. Sain, and S. J. Beebe, "Nanosecond Pulsed Electric Fields (nsPEFs) activate Intrinsic Caspase-Dependent and Caspase-Independent cell death in Jurkat cells," *Biochemical and Biophysical Research Communications*, vol. 421, no. 4, pp. 808–812, 2012.

[9] L. Carr, S. M. Bardet, R. C. Burke, D. Arnaud-Cormos, P. Leveque, and R. P. O'Connor, "Calcium-Independent disruption of Microtubule Dynamics by Nanosecond Pulsed Electric Fields in U87 Human Glioblastoma Cells," *Scientific Reports*, vol. 7, no. 1, 2017.

[10] A. G. Pakhomov, S. Xiao, O. N. Pakhomova, I. Semenov, M. A. Kuipers, and B. L. Ibey, "Disassembly of Actin structures by Nanosecond Pulsed Electric Field is a downstream Effect of Cell Swelling," *Bioelectrochemistry*, vol. 100, pp. 88–95, 2014.

[11] K. Huber, "The Sympathoadrenal Cell Lineage: Specification, Diversification, and New Perspectives," *Developmental Biology*, vol. 298, no. 2, pp. 335–343, 2006.

[12] K. Huber, C. Kalcheim, and K. Unsicker, "The Development of the Chromaffin cell Lineage from the Neural Crest," *Autonomic Neuroscience*, vol. 151, no. 1, pp. 10–16, 2009.

[13] J.C. Waymire, W.F. Bennett, R. Boeheme, L. Hankins, K.G. Waymire and J.W. Haycock. Bovine Adrenal Chromaffin Cells: High-yield purification and Viability in Suspension Culture. J. Neurosci. Methods, 7: 329-351, 1983.

[14] N. Hassan, I. Chatterjee, N. Publicover, and G. Craviso, "Mapping Membrane-potential perturbations of Chromaffin Cells exposed to Electric Fields," *IEEE Transactions on Plasma Science*, vol. 30, no. 4, pp. 1516–1524, 2002.

[15] R. Joshi, Q. Hu, and K. Schoenbach, "Modeling Studies of Cell Response to Ultrashort, High-Intensity Electric Fields—Implications for Intracellular Manipulation," *IEEE Transactions on Plasma Science*, vol. 32, no. 4, pp. 1677–1686, 2004.

[16] García, A., Padín, F., Fernández-Morales, J., Maroto, M. and García-Sancho, J. (2012). Cytosolic Organelles shape Calcium Signals and Exo–endocytotic responses of Chromaffin cells. *Cell Calcium*, 51(3-4), pp.309-320.

[17]Contreras, L., Drago, I., Zampese, E. and Pozzan, T. (2010). Mitochondria: The Calcium Connection. *Biochimica et Biophysica Acta (BBA) - Bioenergetics*, 1797(6-7), pp.607-618.

[18] G. L. Craviso, S. Choe, P. Chatterjee, I. Chatterjee, and P. T. Vernier, "Nanosecond Electric Pulses: A Novel Stimulus for Triggering Ca^{2+} Influx into Chromaffin Cells Via Voltage-Gated Ca^{2+} Channels," *Cellular and Molecular Neurobiology*, vol. 30, no. 8, pp. 1259–1265, 2010.

[19] G. L. Craviso, S. Choe, I. Chatterjee, and P. T. Vernier, "Modulation of Intracellular Ca^{2+} levels in Chromaffin cells by Nanoelectropulses," *Bioelectrochemistry*, vol. 87, pp. 244–252, 2012.

[20] G. Craviso, P. Chatterjee, G. Maalouf, A. Cerjanic, J. Yoon, I. Chatterjee, and P. Vernier, "Nanosecond Electric Pulse-induced increase in Intracellular Calcium in Adrenal Chromaffin cells triggers Calcium-Dependent Catecholamine release," *IEEE Transactions on Dielectrics and Electrical Insulation*, vol. 16, no. 5, pp. 1294–1301, 2009.

[21] P. T. Vernier, Y. Sun, M.-T. Chen, M. A. Gundersen, and G. L. Craviso, "Nanosecond Electric Pulse-Induced Calcium entry into Chromaffin Cells," *Bioelectrochemistry*, vol. 73, no. 1, pp. 1–4, 2008.

[22] P. Vernier, Y. Sun, L. Marcu, S. Salemi, C. M. Craft, and M. A. Gundersen, "Calcium bursts induced by Nanosecond Electric Pulses," *Biochemical and Biophysical Research Communications*, vol. 310, no. 2, pp. 286–295, 2003.

[23] M. Casciola, S. Xiao, and A. G. Pakhomov, "Damage-free Peripheral Nerve Stimulation by 12-ns Pulsed Electric Field," *Scientific Reports*, vol. 7, no. 1, 2017.

[24] A. G. Pakhomov, E. Gianulis, P. T. Vernier, I. Semenov, S. Xiao, and O. N. Pakhomova, "Multiple Nanosecond Electric Pulses increase the Number but not the size of long-lived Nanopores in the Cell Membrane," *Biochimica et Biophysica Acta (BBA) - Biomembranes*, vol. 1848, no. 4, pp. 958–966, 2015.

[25] A. G. Pakhomov, A. M. Bowman, B. L. Ibey, F. M. Andre, O. N. Pakhomova, and K. H. Schoenbach, "Lipid Nanopores can form a stable, Ion Channel-like Conduction pathway in Cell Membrane," *Biochemical and Biophysical Research Communications*, vol. 385, no. 2, pp. 181–186, 2009.

[26] A. M. Bowman, O. M. Nesin, O. N. Pakhomova, and A. G. Pakhomov, "Analysis of Plasma Membrane Integrity by Fluorescent Detection of Tl Uptake," *The Journal of Membrane Biology*, vol. 236, no. 1, pp. 15–26, 2010.

[27] O. N. Pakhomova, B. W. Gregory, V. A. Khorokhorina, A. M. Bowman, S. Xiao, and A. G. Pakhomov, "Electroporation-Induced Electrosensitization," *PLoS ONE*, vol. 6, no. 2, 2011.

[28] M.-F. Bader, R. W. Holz, K. Kumakura, and N. Vitale, “Exocytosis: The Chromaffin Cell As a Model System,” *Annals of the New York Academy of Sciences*, vol. 971, no. 1, pp. 178–183, 2002.

[29] García-Sancho, J., de Diego, A. and García, A. (2012). Mitochondria and Chromaffin Cell Function. *Pflügers Archiv - European Journal of Physiology*, 464(1), pp.33-41.

[30] García, A., Padín, F., Fernández-Morales, J., Maroto, M. and García-Sancho, J. (2012). Cytosolic Organelles shape Calcium signals and exo–endocytotic responses of Chromaffin Cells. *Cell Calcium*, 51(3-4), pp.309-320.

[31] Santo-Domingo, J. and Demaurex, N. (2010). Calcium uptake mechanisms of Mitochondria. *Biochimica et Biophysica Acta (BBA) - Bioenergetics*, 1797(6-7), pp.907-912.

[32] J. García-Sancho and A. Verkhratsky, “Cytoplasmic organelles determine complexity and specificity of calcium signalling in adrenal chromaffin cells,” *Acta Physiologica*, vol. 192, no. 2, pp. 263–271, 2007.

[33] M. Montero, M. T. Alonso, E. Carnicero, I. Cuchillo-Ibáñez, A. Albillos, A. G. García, J. García-Sancho, and J. Alvarez, “Chromaffin-cell stimulation triggers fast millimolar mitochondrial Ca2 transients that modulate secretion,” *Nature Cell Biology*, vol. 2, no. 2, pp. 57–61, 1999.

[34] D. R. Giovannucci, M. D. Hlubek, and E. L. Stuenkel, “Mitochondria Regulate the Ca^{2+}–Exocytosis Relationship of Bovine Adrenal Chromaffin Cells,” *The Journal of Neuroscience*, vol. 19, no. 21, pp. 9261–9270, 1999.

[35] S. Vestring, J. C. Fernández-Morales, I. Méndez-López, D. C. Musial, A.-M. G. D. Diego, J. F. Padín, and A. G. García, “Tight mitochondrial control of calcium and

exocytotic signals in chromaffin cells at embryonic life," *Pflügers Archiv - European Journal of Physiology*, vol. 467, no. 12, pp. 2589–2601, 2015.

[36] J. K. Foskett and M. Madesh, "Regulation of the mitochondrial Ca^{2+} uniporter by MICU1 and MICU2," *Biochemical and Biophysical Research Communications*, vol. 449, no. 4, pp. 377–383, 2014.

[37] N. Demaurex, D. Poburko, and M. Frieden, "Regulation of plasma membrane calcium fluxes by mitochondria," *Biochimica et Biophysica Acta (BBA) - Bioenergetics*, vol. 1787, no. 11, pp. 1383–1394, 2009.

[38] B. Alberts, A. Johnson, J. Lewis, M. Raff, K. Roberts, and P. Walter, *Molecular biology of the cell*. NY.: Garland Science, 2002.

[39] S. W. Perry, J. P. Norman, J. Barbieri, E. B. Brown, and H. A. Gelbard, "Mitochondrial membrane potential probes and the proton gradient: a practical usage guide," *BioTechniques*, vol. 50, no. 2, pp. 98–115, 2011.

[40] A. D. Presley, K. M. Fuller, and E. A. Arriaga, "MitoTracker Green labeling of mitochondrial proteins and their subsequent analysis by capillary electrophoresis with laser-induced fluorescence detection," *Journal of Chromatography B*, vol. 793, no. 1, pp. 141–150, 2003.

[41] J. Villanueva, S. Viniegra, Y. Gimenez-Molina, V. Garcia-Martinez, G. Exposito-Romero, M. D. M. Frances, J. Garcia-Sancho, and L. M. Gutierrez, "The position of mitochondria and ER in relation to that of the secretory sites in chromaffin cells," *Journal of Cell Science*, vol. 127, no. 23, pp. 5105–5114, 2014.

[42] A. Mathur, “Evaluation of fluorescent dyes for the detection of mitochondrial membrane potential changes in cultured cardiomyocytes,” *Cardiovascular Research*, vol. 46, no. 1, pp. 126–138, 2000.

[43] D. C. Joshi and J. C. Bakowska, “Determination of Mitochondrial Membrane Potential and Reactive Oxygen Species in Live Rat Cortical Neurons,” *Journal of Visualized Experiments*, no. 51, 2011.

[44] Miyamoto, S., Howes, A., Adams, J., Dorn, G. and Brown, J. (2005). Ca^{2+} Dysregulation Induces Mitochondrial Depolarization and Apoptosis. *Journal of Biological Chemistry*, 280(46), pp.38505-38512.

[45] Y. Li, N. Johnson, M. Capano, M. Edwards, and M. Crompton, “Cyclophilin-D promotes the mitochondrial permeability transition but has opposite effects on apoptosis and necrosis,” *Biochemical Journal*, vol. 383, no. 1, pp. 101–109, 2004.

[46] S. Beebe, N. Sain, and W. Ren, “Induction of Cell Death Mechanisms and Apoptosis by Nanosecond Pulsed Electric Fields (nsPEFs),” *Cells*, vol. 2, no. 1, pp. 136–162, 2013.

[47] B. Xiao, J.-Y. Goh, L. Xiao, H. Xian, K.-L. Lim, and Y.-C. Liou, “Reactive oxygen species trigger Parkin/PINK1 pathway–dependent mitophagy by inducing mitochondrial recruitment of Parkin,” *Journal of Biological Chemistry*, vol. 292, no. 40, pp. 16697–16708, 2017.

[48] E. Jones, N. Gaytan, I. Garcia, A. Herrera, M. Ramos, D. Agarwala, M. Rana, W. Innis-Whitehouse, E. Schuenzel, and R. Gilkerson, “A threshold of transmembrane potential is required for mitochondrial dynamic balance mediated by DRP1 and OMA1,” *Cellular and Molecular Life Sciences*, vol. 74, no. 7, pp. 1347–1363, 2016.

[49] Beebe, S. (2015). Considering effects of nanosecond pulsed electric fields on proteins. *Bioelectrochemistry*, 103, pp.52-59.

[50] M. L. Lim, T. Minamikawa, and P. Nagley, "The protonophore CCCP induces mitochondrial permeability transition without cytochrome c release in human osteosarcoma cells," *FEBS Letters*, vol. 503, no. 1, pp. 69–74, 2001.

[51] S. Chalmers, S. T. Caldwell, C. Quin, T. A. Prime, A. M. James, A. G. Cairns, M. P. Murphy, J. G. Mccarron, and R. C. Hartley, "Selective Uncoupling of Individual Mitochondria within a Cell Using a Mitochondria-Targeted Photoactivated Protonophore," *Journal of the American Chemical Society*, vol. 134, no. 2, pp. 758–761, 2011.

[52] P.-H. Lou, B. S. Hansen, P. H. Olsen, S. Tullin, M. P. Murphy, and M. D. Brand, "Mitochondrial uncouplers with an extraordinary dynamic range," *Biochemical Journal*, vol. 407, no. 1, pp. 129–140, 2007.

[53] C. L. Haynes, L. A. Buhler, and R. M. Wightman, "Vesicular Ca^{2+} -induced secretion promoted by intracellular pH-gradient disruption," *Biophysical Chemistry*, vol. 123, no. 1, pp. 20–24, 2006.

[54] J. M. Hernández-Guijo, V. E. Maneu-Flores, A. Ruiz-Nuño, M. Villarroya, A. G. García, and L. Gandía, "Calcium-Dependent Inhibition of L, N, and P/Q Ca^{2+} Channels in Chromaffin Cells: Role of Mitochondria," *The Journal of Neuroscience*, vol. 21, no. 8, pp. 2553–2560, 2001.

[55] E. Alés, J. Fuentealba, A. G. García, and M. G. López, "Depolarization evokes different patterns of calcium signals and exocytosis in bovine and mouse chromaffin cells: the role of mitochondria," *European Journal of Neuroscience*, vol. 21, no. 1, pp. 142–150, 2005.

[56] Y. Sun, P. Vernier, M. Behrend, L. Marcu, and M. Gundersen, "Electrode Microchamber for Noninvasive Perturbation of Mammalian Cells With Nanosecond Pulsed Electric Fields," *IEEE Transactions on Nanobioscience*, vol. 4, no. 4, pp. 277–283, 2005.

[57] J. Yoon, N. Leblanc, J. Zaklit, P. T. Vernier, I. Chatterjee, and G. L. Craviso, "Enhanced Monitoring of Nanosecond Electric Pulse-Evoked Membrane Conductance Changes in Whole-Cell Patch Clamp Experiments," *The Journal of Membrane Biology*, vol. 249, no. 5, pp. 633–644, 2016.

[58] K. Yee, "Numerical solution of initial boundary value problems involving Maxwell's equations in isotropic media," *IEEE Transactions on Antennas and Propagation*, vol. 14, no. 3, pp. 302–307, 1966.

[59] W. Fan, Z. Chen, and S. Yang, "On the Analytical Solution of the FDTD Method," *IEEE Transactions on Microwave Theory and Techniques*, vol. 64, no. 11, pp. 3370–3379, 2016.

[60] M. Gaffar and D. Jiao, "An explicit and unconditionally stable FDTD method for 3-D electromagnetic analysis," *2013 IEEE MTT-S International Microwave Symposium Digest (MTT)*, 2013.

[61] H. Zhao, S. Crozier, and F. Liu, "Finite difference time domain (FDTD) method for modeling the effect of switched gradients on the human body in MRI," *Magnetic Resonance in Medicine*, vol. 48, no. 6, pp. 1037–1042, 2002.

[62] A. Taflove and S. C. Hagness, *Computational electrodynamics: the finite-difference time-domain method*. Boston: Artech House, 2000.

[63] N. Kuster and F. Schönborn, “Recommended minimal requirements and development guidelines for exposure setups of bio-experiments addressing the health risk concern of wireless communications,” *Bioelectromagnetics*, vol. 21, no. 7, pp. 508–514, 2000.

[64] S. Benkler, N. Chavannes, and N. Kuster, “Novel FDTD Huygens source enables highly complex simulation scenarios on ordinary PCs,” *2009 IEEE Antennas and Propagation Society International Symposium*, 2009.

[65] W. Liu, H. Wang, P. Zhang, C. Li, J. Sun, Z. Chen, S. Xing, P. Liang, and T. Wu, “Statistical Evaluation of Radiofrequency Exposure during Magnetic Resonant Imaging: Application of Whole-Body Individual Human Model and Body Motion in the Coil,” *International Journal of Environmental Research and Public Health*, vol. 16, no. 6, p. 1069, 2019.

[66] G. Vermeeren, M. C. Gosselin, S. Kühn, V. Kellerman, A. Hadjem, A. Gati, W. Joseph, J. Wiart, F. Meyer, N. Kuster, and L. Martens, “The influence of the reflective environment on the absorption of a human male exposed to representative base station antennas from 300 MHz to 5 GHz,” *Physics in Medicine and Biology*, vol. 55, no. 18, pp. 5541–5555, 2010.

[67] S.-E. Hong, I.-K. Cho, H.-D. Choi, and J.-K. Pack, “Numerical anlaysis of human exposure to electromagnetic fields from wireless power transfer systems,” *2014 IEEE Wireless Power Transfer Conference*, 2014.

[68] A. Christ, M. G. Douglas, J. M. Roman, E. B. Cooper, A. P. Sample, B. H. Waters, J. R. Smith, and N. Kuster, “Evaluation of Wireless Resonant Power Transfer Systems With Human Electromagnetic Exposure Limits,” *IEEE Transactions on Electromagnetic Compatibility*, pp. 1–10, 2012.

Chapter 2: Experimental Methods

2.1 Chromaffin cell isolation and culturing

Bovine chromaffin cells were isolated from the medulla of fresh adrenal glands and maintained in suspension culture as described in [1], with modifications described in [2]. Briefly, fresh adrenal glands were acquired from Wolf Pack Meats (University of Nevada, Reno, NV, USA) and transported to the laboratory on ice. The inner medulla was obtained by dissection and placed in ice-cold Ca^{2+}/Mg^{2+} Hank's free balanced salt solution (HBSS[1]) comprised of the following: 137 mM NaCl, 5.37 mM KCl, 0.44 mM KH_2PO_4, 0.54 mM Na_2HPO_4, 4.17 mM $NaHCO_3$, 5.55 mM D-glucose, 5 mM HEPES, phenol red (0.03%) and 0.02% bovine serum albumin (BSA), pH 7.2. A plastic catheter was inserted into the adreno-lumbar vein and red blood cells flushed out by perfusing the medulla with room temperature HBSS[1] for 10 minutes. The medulla was then digested by perfusing the tissue at 30 °C in HBSS[1] containing collagenase B (0.05%) and $CaCl_2$ (50 µM) until the medulla became swollen (typically 30 to 40 minutes). Cells were isolated from the digested medulla by removing the catheter and gently agitating the tissue against the side of the beaker. The cell suspension was filtered through a 100 µm nylon mesh to rid the suspension of tissue debris. The cells were then centrifuged at room temperature four times (30 x g for 6 minutes, 30 x g for 4 minutes, 25 x g for 4 minutes, 25 x g for 3 minutes), with each centrifugation step followed by trituration of the cell pellet and resuspension in HBSS[1] (centrifugation steps 1-3), and Ham's F-12 medium (centrifugation step 4). The Ham's F-12 medium was comprised of the following: Ham's F-12 Nutrient mix (Gibco)

supplemented with 10% bovine calf serum, 1% antibiotic-antimycotic (100 U/ml penicillin, 100 μg/ml streptomycin, and 0.25 μg/ml fungizone), and 6 mg/ml cytosine β-D-arabinofuranoside. After the final centrifugation step, the cells were filtered through a 53 μm nylon mesh and diluted to a final concentration of 4 x 10^5 cells/ml in Ham's F-12 supplemented medium. Chromaffin cells were isolated from non-chromaffin cells by using a differential plating step. This consisted of placing the cell suspension in tissue culture flasks and incubating the cells for ~5-6 hours at 36.5 °C in an atmosphere consisting of 5% CO_2 in air. Under these conditions, non-chromaffin cells adhere to the bottom of the flask whereas chromaffin cells remain in suspension [1]. After the ~5-6 hour incubation period, the cells were pooled from the flasks, and the concentration adjusted to 1 x 10^5 cells/ml. The cells were transferred to 60 mm Petri dishes (10 ml of cells in suspension/dish) and maintained in suspension culture at 36.5 °C in an atmosphere consisting of 5% CO_2 in air. Cells were used in experiments for up to 14 days after culturing.

2.2 Preparation of chromaffin cells for experiments

Aggregates of chromaffin cells that form in suspension culture were dissociated with the neutral protease dispase as reported in [3]. Briefly, the night before an experiment, ~20 mg of the neutral protease dispase and 0.5 mM $CaCl_2$ were added to a Petri dish containing the cells. On the morning of the experiment, the cells were transferred to a conical tube and centrifuged at 20 x g for 10 minutes. The supernatant fraction was removed, and the cell pellet was gently triturated in Ca^{2+}/Mg^{2+}-free HBSS[2] (145 mM NaCl, 5 mM KCl, 1.2 mM Na_2HPO_4, 10 mM D-glucose, 15 mM HEPES). The resuspended cells

were incubated for 10 minutes at 36.5 °C in the cell culture incubator. After the 10-minute incubation period the cells were gently triturated to facilitate cell dissociation. They were returned to the cell culture incubator for another 10 minutes. This process was repeated until the cell aggregates were completely dissociated. The cells were collected by centrifugation at 30 x g at room temperature for 10 minutes and the cell pellet resuspended in 0.7 ml Ham's F-12 complete medium. Cell aliquots of 120 µl were plated on fibronectin-coated 35 mm glass bottom dishes (inner glass diameter 20 mm or 10 mm). Cells were allowed to attach to the dishes for up to two hours. Then, 2.5 ml of Ham's F-12 complete medium was added to each dish and the cells returned to the tissue culture incubator. Cells were used in experiments for up to two days.

2.3 Receptor agonist stimulation

2.3.1 One cell at a time

A dish of attached cells was removed from the incubator on the day of the experiment. Cell medium was removed from the dish and replaced with a balanced salt solution (BSS) comprising the following: 145 mM NaCl, 5 mM KCl, 1.2 mM Na_2HPO_4 , 2 mM $CaCl_2$, 1.3 mM $MgCl_2$, 10 mM glucose, 15 mM HEPES and 0.1% BSA, pH 7.4. The selective nicotinic receptor agonist 1, 1-dimethyl-4-phenyl-piperazinum (DMPP) was applied to a single cell at a concentration of 100 µM in BSS using a pressure ejection system (Picospritzer III®, Parker Hannifin Corporation, Hollis, NH, USA). The micropipettes that delivered the agonist to the cells were fabricated from borosilicate glass

capillaries (Sutter Instruments, FG-GB 120-69-10, outer diameter 1.2 mm, inner diameter 0.69 mm) using a micropipette puller (Sutter Instrument Co. Model P-97). The tips were 1 µm in diameter, measured using a microforge (Sutter MF-830). For applying DMPP, the tip of the micropipette was placed 1.5-cell diameters away from the target cell, as shown in Figure 2.1. The Picosopritzer was triggered through a custom LabVIEW program (version 9, National Instruments, Austin, TX, USA). The settings for each ejection were: pressure, 18 psi (N_2); duration 5 ms.

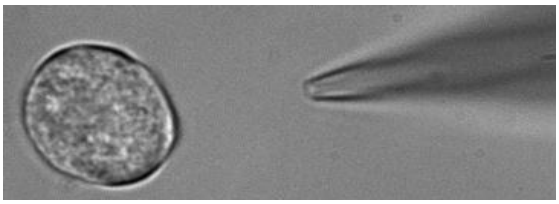

Figure 2.1: Stimulation of a chromaffin cell with the physiological stimulus. A photomicrograph showing a micropipette tip positioned to deliver an ejection of 100 µM DMPP to a chromaffin cell (100x).

2.3.2. Dish of cells

A dish of attached cells was removed from the incubator on the day of the experiment. Cell medium was removed from the dish and replaced with BSS. DMPP was applied to a dish of cells at a concentration of 100 µM in BSS using a perfusion system (Model VC-6, Warner Instruments, Hamden, CT, USA). For the perfusion, a Petri dish insert (Bioscience Tools, San Diego, CA, USA) was attached to the bottom of the dish using vacuum grease. BSS was added to fill the chamber and the dish was placed on the microscope stage. Inlet and outlet tubings were connected to the perfusion dish, and the cells perfused first with BSS at a flow rate of 1-1.2 ml/minutes, followed by perfusion with

DMPP, which reached the cells 30-35 seconds after the valve was switched from BSS to BSS containing the agonist DMPP. Figure 2.2 shows photographs of the perfusion setup.

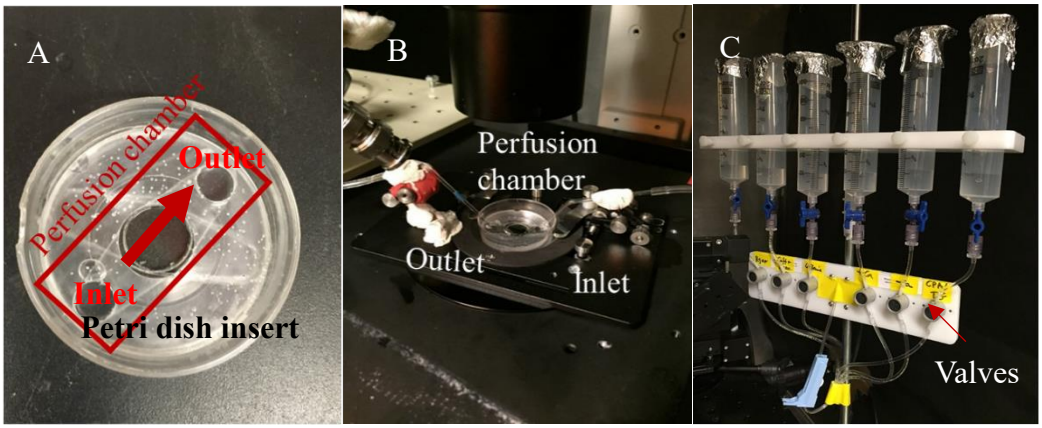

Figure 2.2: Photographs of the perfusion setup. A) A Petri dish insert inside the dish of attached cells. B) The cell dish on the microscope stage and connected to the inlet and outlet tubing. C) The manifold that holds the solutions for perfusion and the valves that control the flow of BSS from each syringe.

2.4 Stimulating cells with 5 ns pulses

2.4.1. Tungsten rod electrode fabrication

A pair of electrodes for delivering 5 ns pulses to cells (shown in Figure 2.3) was fabricated from two cylindrical tungsten rods having a diameter of 127 μm (A-M systems, catalog #716200). Prior to fabrication, the rods were gold coated (160 nm coating thickness) using a sputtering machine (Department of Mechanical Engineering, University of Nevada, Reno).

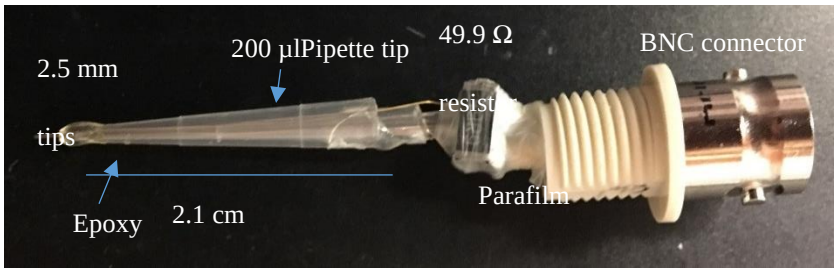

Figure 2.3: Photograph of a pair of tungsten rod electrodes used to deliver a 5 ns pulse to chromaffin cells. The tungsten rods are located inside the pipette tips that have an overall length of 2.1 cm. The tungsten rods protrude 2.5 mm from the end of the pipette tips for exposing cells to a pulse.

To fabricate the electrodes, one of the tungsten rods was inserted through a 200 µl plastic pipette tip with 2.5 mm protruding from the tapered end. A 10 µl plastic pipette tip was placed inside the 200 µl pipette tip to stabilize the first tungsten rod and provide a conduit for the second tungsten rod, which was also inserted with 2.5 mm protruding from the tapered end. Biocompatible epoxy was used to seal the tungsten rods at the point where they exited the pipette tip. The top ends of the pipette tips were trimmed off so that the overall pipette length was 2.1 cm. The tungsten rods protruding from the top end of the pipette tips were soldered onto a BNC connector. A 49.9 Ω surface mount resistor (2 Watts) was soldered onto the BNC connector and the tungsten rod ends using Kester organic solder. The resistance of the electrodes was measured with a multimeter to ensure that the electrodes were not open or short circuited. The range of resistance was 48 Ω to 49.9 Ω. To minimize vibrations of the electrodes during an experiment, a thin layer of parafilm was wrapped around the resistor and the upper end of the pipette tip to stabilize the electrodes. Electrode tips were spaced 100 µm apart from each other using a tweezer coated with electrical tape to avoid scratching the gold coating. The spacing was measured at 20x on an inverted Nikon TE2000 microscope.

2.4.2 Pulse delivery setup

Pulses were generated by a custom fabricated pulse generator [4] obtained from Transient Plasma Systems (Torrance, CA, USA). The pulse generator has an analog control setup, with a maximum voltage output of 6 kV into a 50 Ω load, a maximum power input of 380 V, and a maximum pulse repetition rate of 1 kHz. Voltage output was controlled by a voltage control knob. Figure 2.4 shows a schematic of how a pulse travels from the pulse generator and reaches the electrodes.

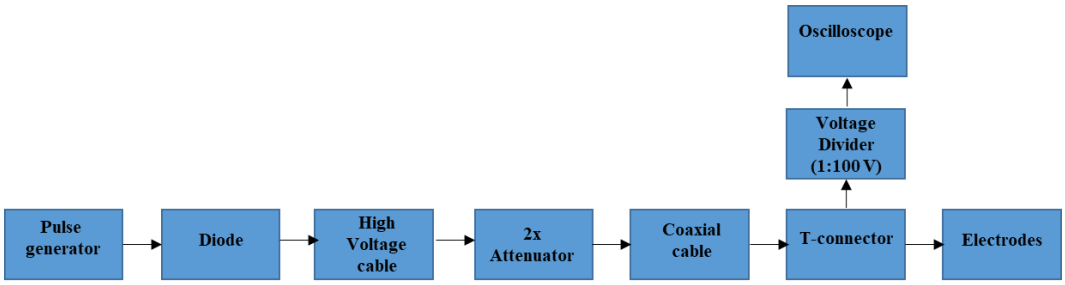

Figure 2.4: Schematic of the 5 ns electric pulse delivery setup.

A diode was attached to the output port of the pulse generator because there was a significant negative peak followed by the main pulse, which was removed by the diode. The signal then passed through a 2x attenuator in order to decrease the voltage by half. The signal then passed through a coaxial cable and through a T-connector, which allowed the signal to reach the electrodes on one end and the oscilloscope on the other. A voltage divider was connected between the T-connector and the oscilloscope cable with a ratio of 1:100 V in order to measure the voltage near the electrodes without damaging the oscilloscope (Figure 2.5). A custom-written LabVIEW program was used to trigger the

pulse generator. The complete pulse delivery setup together with the setup for monitoring cell fluorescence (section 2.5) is shown in Figure 2.6

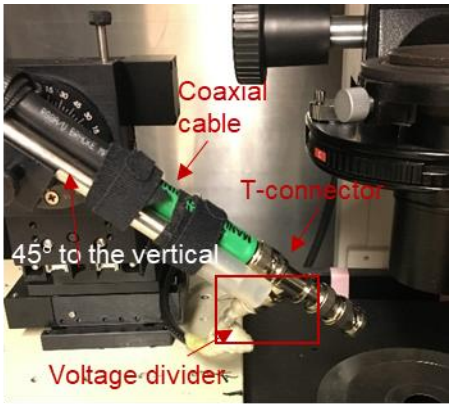

Figure 2.5: Photograph showing the location of the voltage divider with respect to the electrodes. The 50 Ω voltage divider, which is wrapped in parafilm, was connected to the oscilloscope via the T-connector.

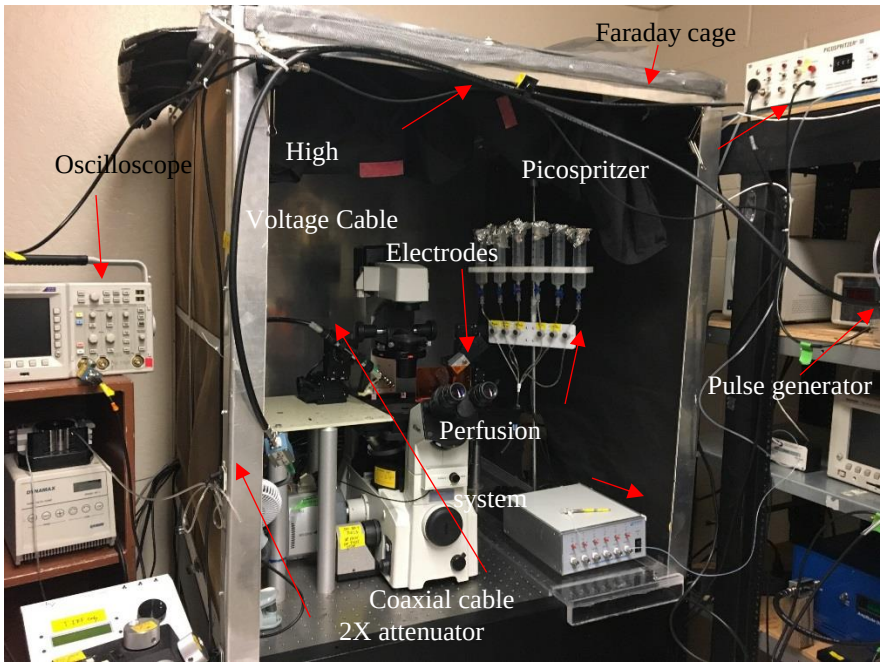

Figure 2.6: Photograph of the pulse delivery and fluorescence imaging setup. The Nikon TE2000 microscope used for experiments is placed on an anti-vibration table and surrounded by a Faraday cage. A rack located to the right of the Faraday cage holds the pulse generator and the diode (not shown). The high voltage cable connected to the pulse generator, the 2x attenuator, and the coaxial cable are secured on the outside of the Faraday cage for attachment to the electrodes. The oscilloscope is on a rack on the left side of the Faraday cage. The Picospritzer is located on the top right shelf of the rack on the right and the perfusion system is located on the right side of the microscope.

FDTD simulations were conducted using the software SEMCAD to determine the electric field magnitude at an applied voltage (see Chapter 5). The computed electric field magnitude at the location of the cell was divided by the maximum applied voltage, which provided a scale factor in MV/m. In order to obtain the desired electric field magnitude, the scale factor was multiplied by an applied voltage to calculate the electric field magnitude. For example, at an applied voltage of 1000 V, the computed electric field is 4.95 MV/m. The scale factor becomes:

$$\text{Scale factor} = (4.95 \times 10^{6}\ \text{V/m})\ (1000\ \text{V})$$

$$= 4.95 \times 10^{-3}\ \text{m}^{-1}$$

Using the above conversion factor, applying 2000 V yields an electric field magnitude of 9.9 MV/m. Validation of the conversion factor and electric field magnitude generated by each applied voltage are shown in Chapter 5.

For experiments, one or more 5 ns pulses were applied to a cell using the tungsten rod electrodes, fabricated as described above. The spacing of the electrode tips was measured before and after each experiment. The electrode tips were positioned 40 µm above the glass bottom dish and positioned 45° to the vertical plane, with the target cell located in the center between the electrode tips as shown in Figure 2.7. Pulses had a half-width of 5 ns, as shown in Figure 2.8. Simulations regarding the electric field distribution can be found in Chapter 5.

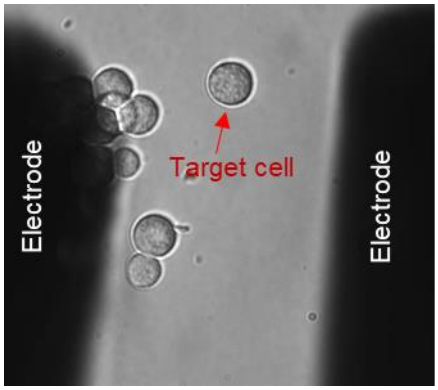

Figure 2.7: Photomicrograph showing the location of the target cell between the tungsten rod electrode tips. The tips are positioned 40 µm above the glass bottom dish and 45° to the vertical for experiments (40x).

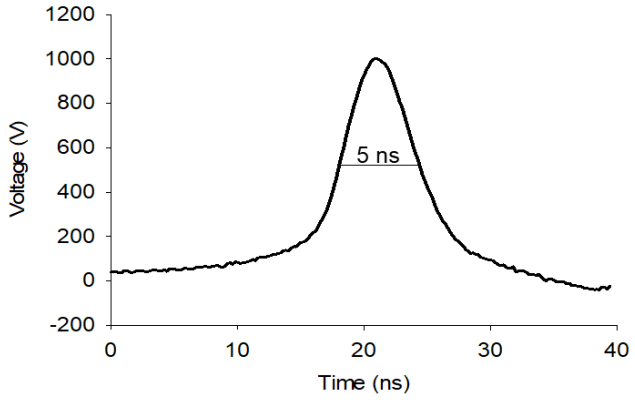

Figure 2.8: Representative trace of a 5 ns electric pulse. The pulse has a half-width of 5 ns, rise and fall time of 4-5 ns. The maximum voltage is 1000 V.

2.5 Fluorescence imaging of intracellular calcium

A dish of attached cells was removed from the incubator on the day of the experiment. Cell medium was carefully removed from the dish and the cells washed twice with BSS. Cells were then incubated with the calcium fluorescence indicator dye Calcium Green-1-AM (1 µM; 480/535 nm) for 45 minutes at 36.5 °C in BSS containing 10% BSA. After the incubation, the cells were washed with BSS lacking BSA and the cell dish was placed directly onto the stage of a Nikon TE2000 epifluorescence microscope. Bright field and fluorescence images of the cells were obtained with a 100x air objective and captured with an iXonEM + DU-897 EMCCD (Andor Technology Ltd. Belfast, UK) using the open source software Micro-Manager (version 1.4). For monitoring intracellular calcium, baseline calcium fluorescence was monitored for 10 seconds prior to applying a stimulus (pulse or physiological stimulus), and for 50 seconds following a stimulus. Changes in fluorescence intensity were calculated by subtracting background fluorescence from the

cell fluorescence utilizing Image J (https://imagej.nih.gov/ij/). The change in fluorescence intensity was obtained by normalizing the fluorescence to the time the stimulus was applied using LabVIEW.

As a control for establishing changes in intracellular calcium caused by mitochondrial membrane potential disruption, cells were labeled with Calcium-Green-1 as described, then incubated with carbonyl cyanide 3-chlorophenyldrazone (CCCP) or carbonilcyanide p-trifluoromethoxyphenylhydrazone (FCCP) for 5 minutes at 36.5 °C in BSS. The concentrations of each were 0.5 µM, 1 µM, or 2 µM. After incubation, cells were placed on the microscope stage and DMPP was applied to the cells by pressure ejection at a saturating concentration of 100 µM. Changes in intracellular calcium were monitored and analyzed as mentioned earlier.

2.6 Fluorescence labeling of mitochondria

Cells were incubated with 100 nM Mitotracker Green (Ex/Em: 490/516 nm) or 20 nM Mitotracker Orange (Ex/Em: 554/576 nm) for 30 minutes at 36.5 °C in BSS. The dye solution was then removed and replaced with dye-free BSS. Fluorescence images were obtained to observe mitochondrial populations in chromaffin cells, as described in the Introduction. Images were obtained with z-stacking at a step size of 0.5 µm.

2.7 Monitoring mitochondrial membrane potential

2.7.1 Labeling Mitochondria

A dish of attached cells was removed from the incubator on the day of the experiment. Cell medium was carefully removed, and the cells washed twice with BSS. Cells were incubated with Tetramethylrhodamine (TMRE, Ex/Em: 543/593 nm) at a concentration of 50 nM or 20 nM in BSS for 20 minutes at 36.5 °C. Alternatively, cells were incubated with Rhodamine 123 (RH 123, Ex/Em: 482/536 nm) at a concentration of 100 nM or 200 nM in BSS for 45 minutes at 36.5 °C. For each, the dye solution was carefully removed and replaced with BSS prior to imaging. Cells were viewed at 100x and images obtained with z-stacking, with a step size of 0.5 µm. Preliminary experiments established that the optimal concentrations for labeling mitochondria were 20 nM TMRE and 200 nM RH 123 as cells did not exhibit saturation at room temperature (Figure 3.10 in Chapter 3).

2.7.2 Perfusion of TMRE and RH 123 labeled cells with CCCP

As a control to monitor a decrease in TMRE or RH 123 fluorescence due to mitochondrial membrane potential disruption, CCCP was applied to TMRE or RH 123 labeled cells using the perfusion setup described earlier for applying DMPP to a dish of cells. A dish of attached cells was removed from the incubator and the cells washed twice with BSS. Cells were labeled with TMRE and RH 123, as described earlier. The dye solution was removed and replaced with BSS. The dish was then placed on the microscope

stage for imaging. Changes in mitochondrial membrane potential were analyzed for a decrease in either TMRE or RH 123 fluorescence by subtracting background fluorescence from whole cell fluorescence and normalized to the time a stimulus was applied as described earlier.

2.7.3 Application of a stimulus to TMRE and RH 123 labeled cells

Mitochondria were labeled with either TMRE or RH 123 and the cells were placed on the microscope stage. Baseline fluorescence was monitored for 10 seconds prior to applying a stimulus (pulse or physiological stimulus) and 50 seconds following a stimulus. Changes in mitochondrial membrane potential were analyzed for a decrease in either TMRE or RH 123 fluorescence by subtracting background fluorescence from whole cell fluorescence, and normalized to the time a stimulus was applied, as described earlier.

2.8 Statistical analysis

Experiments were repeated at least twice using cells from two or more cell preparations. Normalized calcium and mitochondrial membrane potential responses are represented as the mean ± standard error (S.E.). Rate of recovery of calcium traces was calculated by fitting either a linear equation or a 3-parameter exponential decay ($y = y_0 + ae^{-bx}$). Origin pro (Origin Lab corporation, 2019) was used to correct TMRE and RH 123 fluorescence traces for photobleaching. Sigmapot (Systat software, 2014) was used to plot the results. A one-way analysis of variance (ANOVA) was used to determine the statistical

significance between two or more groups. P values <0.05 were considered statistically significant.

2.9 Reagents

Calcium Green-1-AM, Mitotracker Green, and Mitotracker Orange were purchased from Molecular Probes (Eugene, OR, USA). Ham's F-12 medium, dispase II, and antibiotic-antimycotic were purchased from Gibco Laboratories (Grand Island, NY, USA). Bovine calf serum was purchased from Gemini Bio-Products (West Sacramento, CA, USA). Collagenase B was purchased from Roche Diagnostics (Indianapolis, IN, USA). Cytosine β-D-arabinofuranoside, tetramethylrhodamine, Rhodamine 123, carbonyl cyanide 3-cholorophenyldrazone (CCCP), carbonilcyanide p-trifluoromethoxyphenylhydrazone (FCCP), were purchased from Sigma. All other chemicals and reagents were purchased from standard commercial sources.

References:

[1] J.C. Waymire, W.F. Bennett, R. Boeheme, L. Hankins, K.G. Waymire and J.W. Haycock. Bovine Adrenal Chromaffin cells: High-yield purification and viability in suspension culture. J. Neurosci. Methods, 7: 329-351, 1983.

[2] N. Hassan, I. Chatterjee, N. Publicover, and G. Craviso, "Mapping membrane-potential perturbations of chromaffin cells exposed to electric fields," *IEEE Transactions on Plasma Science*, vol. 30, no. 4, pp. 1516–1524, 2002.

[3] G.L. Craviso. Generation of functionally competent single bovine adrenal chromaffin cells from cell aggregates using the neutral protease dispase. J. Neurosci. Methods, 137: 275-281, 2004.

[4] Kuthi, A., Gabrielsson, P., Behrend, M., Vernier, P. and Gundersen, M. (2005). Nanosecond pulse Generator using fast recovery diodes for cell electromanipulation. *IEEE Transactions on Plasma Science*, 33(4), pp.1192-1197.

Chapter 3: Fluorescence imaging of intracellular calcium and mitochondrial membrane potential in chromaffin cells exposed to 5 ns pulses

3.1 Introduction

The results presented in this Chapter show that in chromaffin cells, application of a 5 ns, 5 MV/m pulse caused a rapid rise in intracellular calcium that is longer-lived than in cells stimulated with either a single application or even multiple applications of a saturating concentration of the nicotinic receptor agonist DMPP. As a potential explanation for this difference, we hypothesized that the externally applied electric field penetrates the cell membrane causing a disruption of the mitochondrial membrane potential, thereby delaying clearance of calcium. As stated previously, mitochondria are the main organelle involved in the rapid clearance of intracellular calcium following calcium influx via VGCCs [1-5] and that disruption of the mitochondrial membrane potential delays calcium uptake into this organelle [1]. This Chapter describes the results of studies in which mitochondria were labeled with membrane potential-dependent fluorescent dyes to determine whether 5 ns electric pulses have an effect on mitochondrial membrane potential.

3.2 A single 5 ns pulse evokes longer-lived increases in intracellular calcium compared to the physiological stimulus

As previously reported [6-9], chromaffin cells labeled with Calcium-Green-1 and stimulated with a single 5 ns pulse at 5 MV/m underwent a rise in intracellular calcium level (Figure 3.1). Shown in Figure 3.2 is the time course of the response. The rise in intracellular calcium reached a peak amplitude 2-4 s after the pulse, with an average T_{50} (time to reach half of the maximum increase in intracellular calcium) of 2.2 s. However, there was a great deal of variation with respect to the time taken for intracellular calcium to return to pre-stimulus levels, with the cells falling roughly into two groups. In half of the cells (N=11/21), intracellular calcium returned to near pre-stimulus levels within the 50 s post-pulse monitoring period, displaying a half-width (i.e., the time to decline to half of the maximum rise in calcium) of 23 s. In the remaining cells, the decline of intracellular calcium to pre-stimulus levels was much slower such that a half-width could not be determined. Therefore, a 5 ns pulse at 5 MV/m can evoke calcium responses in cells that either recover to near pre-stimulus calcium levels 50 s post-stimulus or are longer-lived. Differences in response duration have been observed previously and are most likely due to cell-cell variability [6-9]. However, factors such as electrode placement during an experiment could also contribute to variability. This issue is further discussed in Chapter 5.

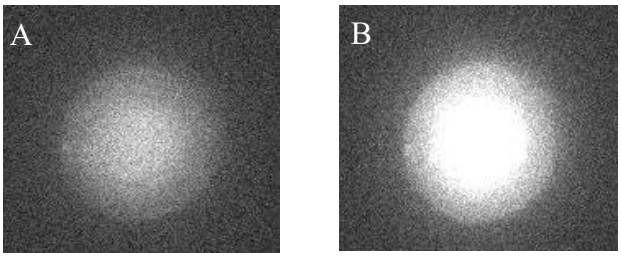

Figure 3.1: Fluorescence images of a chromaffin cell stimulated with a 5 ns, 5 MV/m pulse. The cell was loaded with Calcium-Green-1 and a fluorescence image obtained A) before and B) 1 s after the pulse was delivered to the cell.

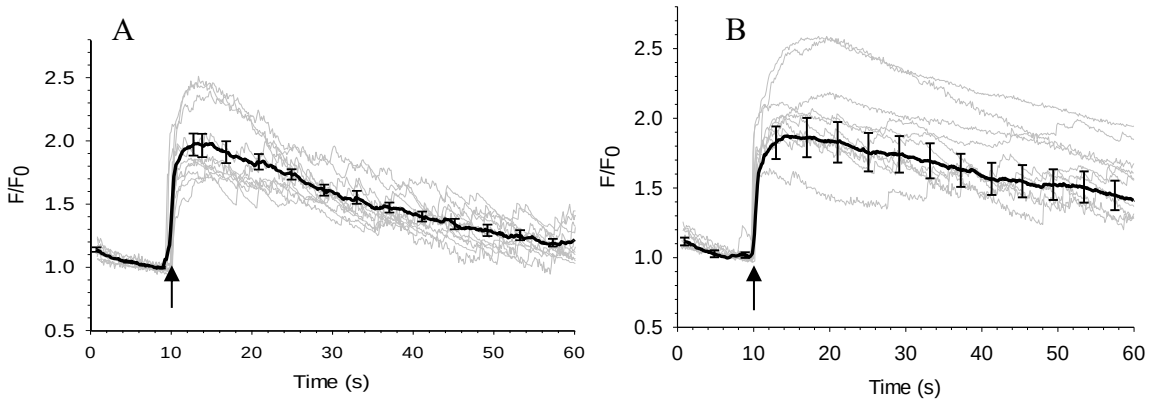

Figure 3.2: Calcium responses in chromaffin cells evoked by a single 5 ns pulse. Representative fluorescence traces together with the averaged responses for cells exposed to a 5 ns pulse. A) Calcium responses (N=11) having an average half-width of 23 s. B) Calcium responses (N=10) having no measurable half-width during the monitoring period. Arrows indicate the time that the pulse was delivered to the cells.

Using carbachol as a cholinergic receptor agonist, we had previously shown that following the rapid rise in intracellular calcium evoked by the agonist, intracellular calcium returned to pre-stimulus levels within 20 s, displaying a half-width of ~5-6 s [6]. Given these results, we compared here calcium responses evoked by a 5 ns pulse to those evoked by DMPP, a cholinergic receptor agonist that is specific for nicotinic receptors. For these experiments a saturating concentration of DMPP (100 μM) was used to stimulate the cells. As shown in Figure 3.3, a 5 ms application of DMPP caused the cells to undergo a rapid

rise in intracellular calcium that reached a maximum in 1-2 s, with an average T_{50} of 0.5 s. The amplitude of the response was similar to that caused by a 5 ns pulse. Importantly, the return of intracellular calcium to pre-stimulus levels occurred within 20 s, with an average half-width of ~8 s. These results are similar to our results reported previously using carbachol as the agonist [6]. It is important to note that the calcium responses also lacked the variability in duration observed for calcium responses evoked by a 5 ns pulse.

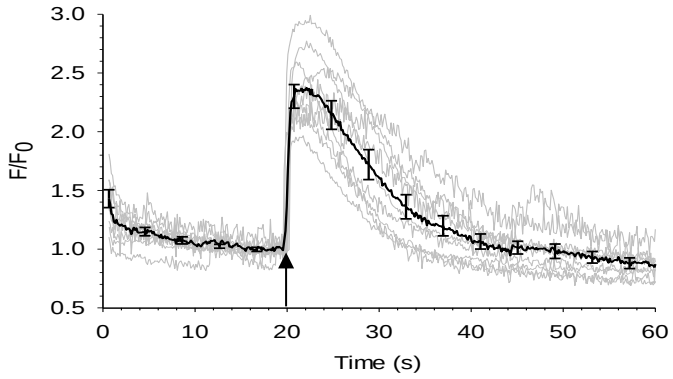

Figure 3.3: Calcium responses of chromaffin cells stimulated with DMPP. Representative fluorescence traces together with the averaged responses for cells (N=9) exposed to a 5 ms application of 100 µM DMPP, applied at 20 s (indicated by the arrow).

Table 1 summarizes the characteristics of the calcium responses evoked by a 5 ns pulse versus those evoked by nicotinic receptor activation. Although the time for intracellular calcium to reach a maximum was slightly faster for DMPP, the biggest difference between the calcium responses evoked by the two stimuli was the duration of the response. DMPP-stimulated cells had a faster recovery compared to cells stimulated by a 5 ns pulse.

Table 1: Comparison of the characteristics of calcium responses evoked by a 5 ns pulse and DMPP

Stimulus	T_{50} ± SE (s)	Maximum Amplitude ± SE (F/F_0)	Half-width ± SE (s)	Recovery Rate ± SE* ((F/F_0)/s)
5 ns pulse (N=21)	2.2 ± 0.3	2.1 ± 0.3	23.0 ± 2.6 (N =11)	0.02± 0.0 (N =11)
DMPP (N=9)	0.5 ± 0.0	2.0 ± 0.2	8.0 ± 1.0	4.94 ± 4.5

*Calcium responses were graphed in Sigmaplot. Those for DMPP were fit to an exponential decay whereas those evoked by a 5 ns pulse were fit to a linear function.

To explore further the difference in duration of calcium responses evoked by each stimulus, we compared the time course of the rise in intracellular calcium in response to multiple applications of DMPP versus a single or a train of 5 ns pulses. As shown in Figure 3.4, A, five applications of DMPP at a repetition rate of 1 Hz stimulated a rise in intracellular calcium that rapidly returned toward baseline once DMPP application stopped. The average half-width of the response was 9 s, which was similar to the half-width of the response recorded for one application of DMPP and thus still less than that for a single 5 ns pulse. Ten applications of DMPP also at a repetition rate of 1 Hz similarly showed a rapid return of intracellular calcium to baseline as soon as the DMPP stimulus ended (Figure 3.4, B). In this case, the average half-width of the response was 13 s but still significantly less than that observed for a single 5 ns pulse. These results indicate that the calcium response evoked by a single 5 ns pulse outlasts the calcium response stimulated by multiple applications of the physiological stimulus.

The delay in the recovery of intracellular calcium to baseline in cells exposed to 5 ns pulses was even more dramatic when cells were exposed to multiple pulses. As shown in Figure 3.4, C, calcium responses evoked by a train of five pulses delivered at a rate of 1 Hz started to decline slowly at the end of the pulse train, displaying a half-width of ~26 s.

For a train of 10 pulses delivered at the same rate, (Figure 3.4, D), the half-width could not be measured as it was longer than the recording period. These results are clear evidence that 5 ns pulses evoke calcium responses that are prolonged relative to those evoked by the physiological stimulus. As a basis for understanding this effect on intracellular calcium, we next explored whether the effects could be due to mitochondrial membrane potential disruption.

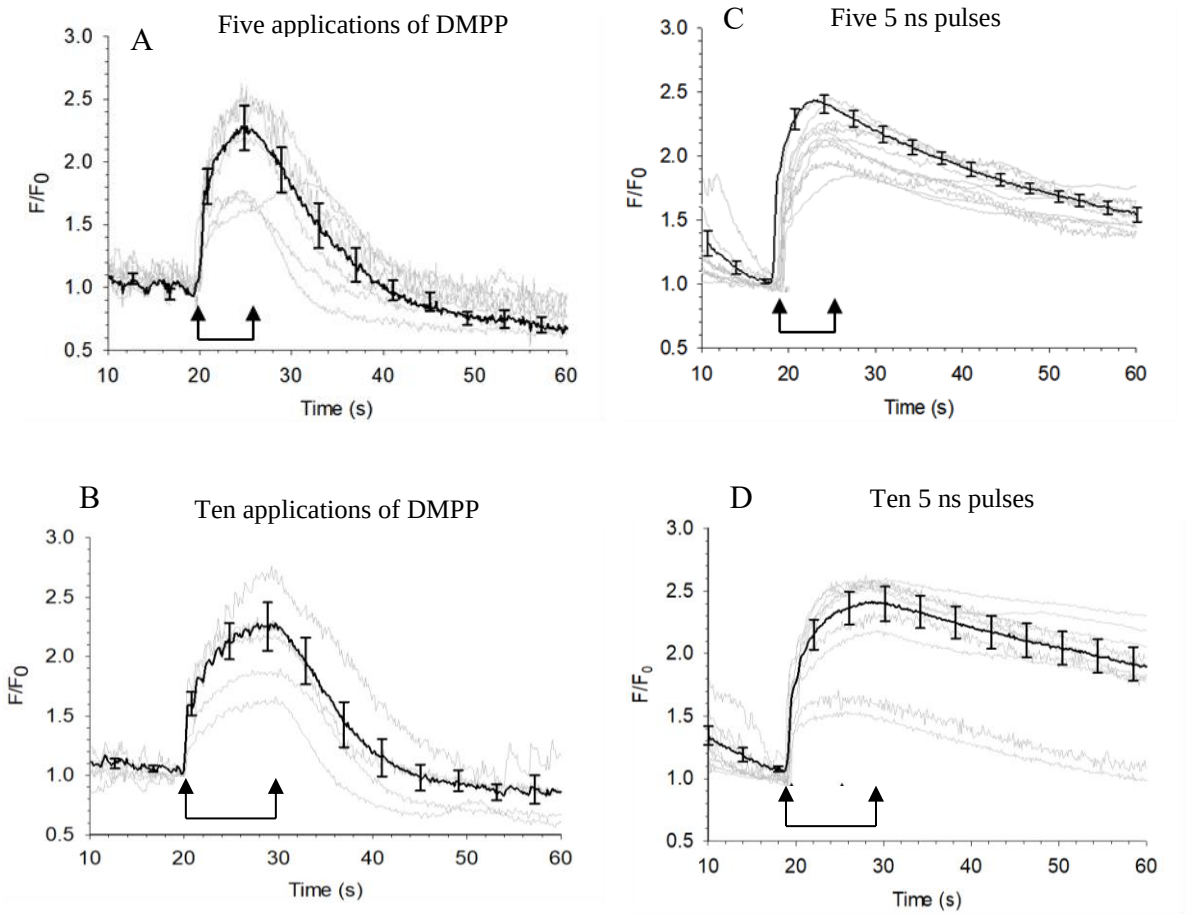

Figure 3.4: Calcium responses in cells stimulated with trains of DMPP applications versus trains of 5 ns pulses. Representative fluorescence traces together with the averaged responses for cells exposed to A) five (N=6) or B) ten (N=4) 5 ms applications of 100 µM DMPP (repetition rate of 1 Hz), and to a train of C) five (N=11) or D) ten (N=8) 5 ns pulses (repetition rate of 1 Hz). The arrows indicate the time of DMPP or pulse delivery.

3.3 Disrupting mitochondrial membrane potential alters the calcium response of cells evoked by a depolarizing stimulus

Previous studies by other groups have shown that pre-treating bovine chromaffin cells with 1-2 µM of the mitochondrial membrane potential disrupter CCCP had little effect on the amplitude of the rise in intracellular calcium evoked by perfusing the cells with high KCl, causing only a more rounded versus a sharp calcium peak [10-12]. CCCP, however, did cause the half-width of the response to slightly increase (by 20 s) compared to the control cells. Since the ability to observe the effects of CCCP on stimulus evoked-calcium responses appeared to require a prolonged period of cell stimulation [12], our approach to assess the effect of CCCP was to apply multiple applications of a depolarizing stimulus to cells pretreated with CCCP.

3.3.1 Effects of CCCP on calcium responses evoked by multiple applications of DMPP

As a control for assessing the effects of disrupting mitochondrial membrane potential on calcium responses, cells were labeled with Calcium-Green-1 as described in Section 2.6. After incubation, the dye solution was removed and replaced with BSS containing 0.5 µM, 1 µM or 2 µM CCCP. Cells were then incubated with CCCP for 5 minutes at 36.5 °C. After the 5-minute incubation, cells were placed immediately on the stage of the microscope and stimulated with five applications of 100 µM DMPP at a repetition rate of 1 Hz in the continued presence of CCCP (the maximum time that the cells

were in the presence of CCCP was 15 minutes). In cells treated with 1 µM (Figure 3.5) and 2 µM CCCP (not shown), calcium responses were significantly reduced in amplitude compared to the control responses. This reduction may have been due to the immediate effects of CCCP on the calcium current by reducing calcium influx through VGCCs [13], a disruption in ATP production [13-14], or possibly longer-term effects such as a change in the pH gradient and ROS production [15-16]. Given these results we then reduced further the concentration of CCCP to 0.5 µM (Figure 3.5) that may be more selective for causing mitochondrial membrane disruption. The results still showed significant effects of CCCP on calcium responses. As determined by a one-way ANOVA with a post-hoc Tukey analysis with a significance level of $p = 0.05$, the p-value for the calcium amplitude was < 0.01 between the calcium responses of the control cells and all the CCCP treated cells, indicating that the differences were statistically significant. With respect to the half-width, differences were not statistically significant ($p > 0.05$). We did not further reduce the concentration of CCCP below 0.5 µM.

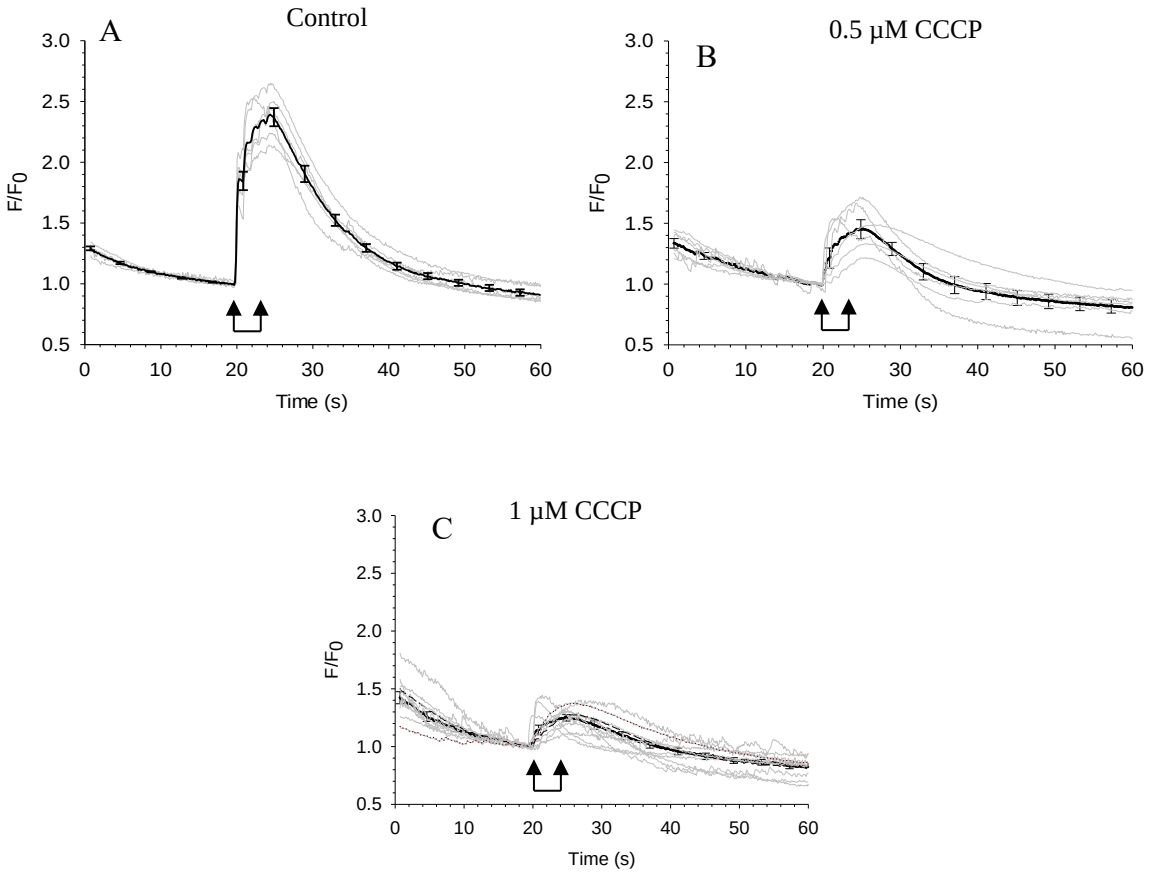

Figure 3.5: Calcium responses in cells treated with CCCP and stimulated with 5 applications of DMPP. Representative fluorescence traces together with the average responses for five applications of DMPP (100 µM, 1 Hz). A) Control cells (N=6), B) 0.5 µM CCCP-treated cells (N=6), and C) 1 µM CCCP-treated cells (N=17). Arrows indicate the time of DMPP delivery.

We next increased the number of applications of DMPP to ten at a repetition rate of 10 Hz, thus providing an even stronger stimulus. As shown in Figure 3.6, calcium responses in cells treated with 0.5 µM CCCP were variable with amplitudes that were either similar to those of the control cells or much smaller. In cells treated with 1 µM CCCP, calcium responses were significantly reduced, as shown in Figure 3.5 for cells exposed to 5 applications of DMPP. A one-way ANOVA with post-hoc Tukey analysis with a significance level of $p = 0.05$ showed that the p-value was < 0.05 between the calcium

response of the control cells and the CCCP-treated cells, indicating statistical significance. With respect to the half-width, differences were not statistically significant ($p > 0.05$).

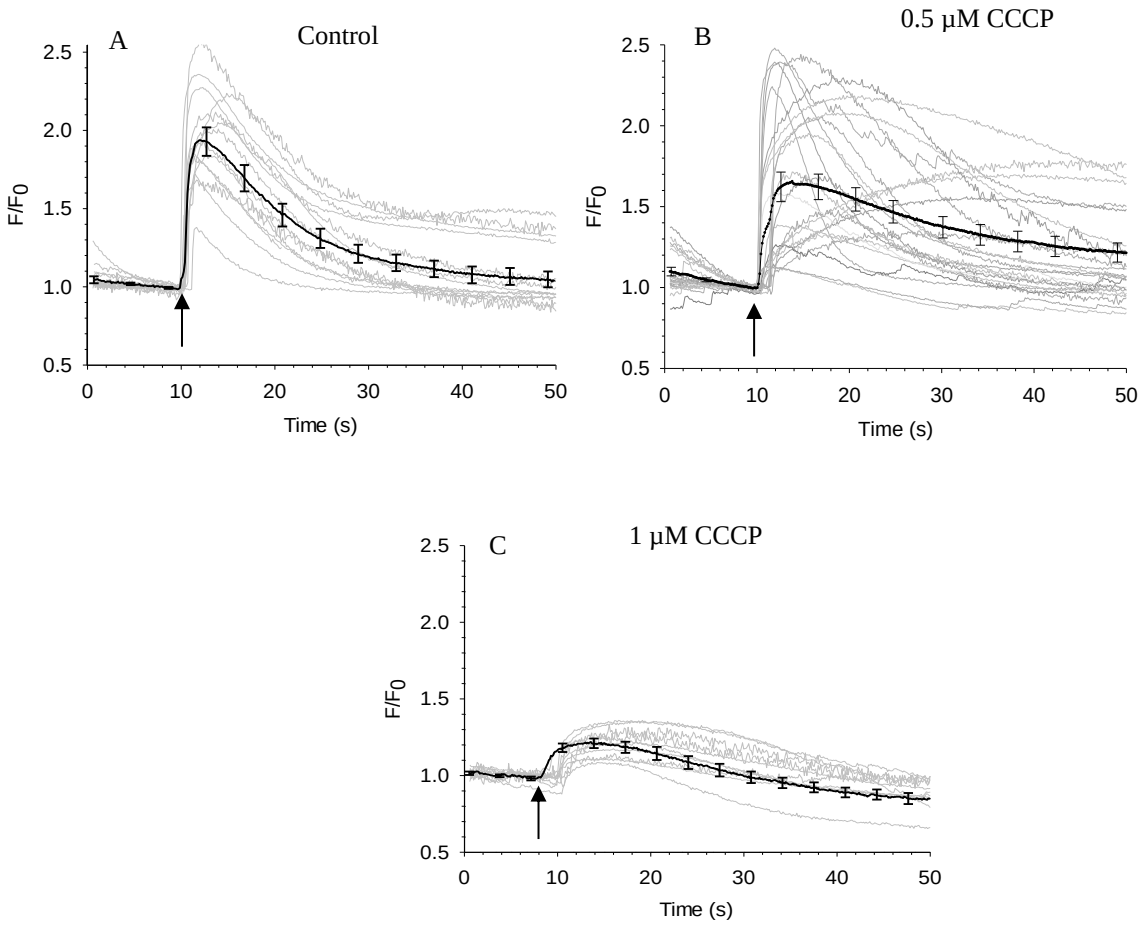

Figure 3.6: Calcium responses of cells treated with CCCP and stimulated with 10 applications of DMPP. Representative fluorescence traces together with the average responses for ten applications of DMPP (100 µM, 10 Hz). A) Control cells (N=14), B) cells treated with 0.5 µM CCCP (N=26), C) cells treated with 1 µM CCCP (N=10). Arrows indicate the time of DMPP delivery.

The next section discusses results obtained using a second mitochondrial membrane potential disrupter, FCCP.

3.3.2 Effect of FCCP on calcium responses evoked by ten applications of DMPP

Chromaffin cells were treated with a second mitochondrial membrane potential disrupter, FCCP, to establish further how calcium responses to DMPP are altered by mitochondrial membrane potential disruption. Cells were labeled with Calcium-Green-1, incubated with FCCP in the same manner as CCCP, and stimulated with ten applications of DMPP at a repetition rate of 10 Hz. Overall, the calcium responses of cells treated with FCCP (Figure 3.7) were similar to those observed in cells treated with CCCP (Figure 3.6). A one-way ANOVA test with a significance level of $p = 0.05$ showed that the p-value for the calcium amplitude between the calcium responses of the control cells and FCCP treated cells was $p < 0.01$, indicating statistical significance. The p-value for the half-width was $p > 0.05$, indicating that the differences were not statistically significant.

The next section discusses calcium responses evoked by KCl as the depolarizing stimulus.

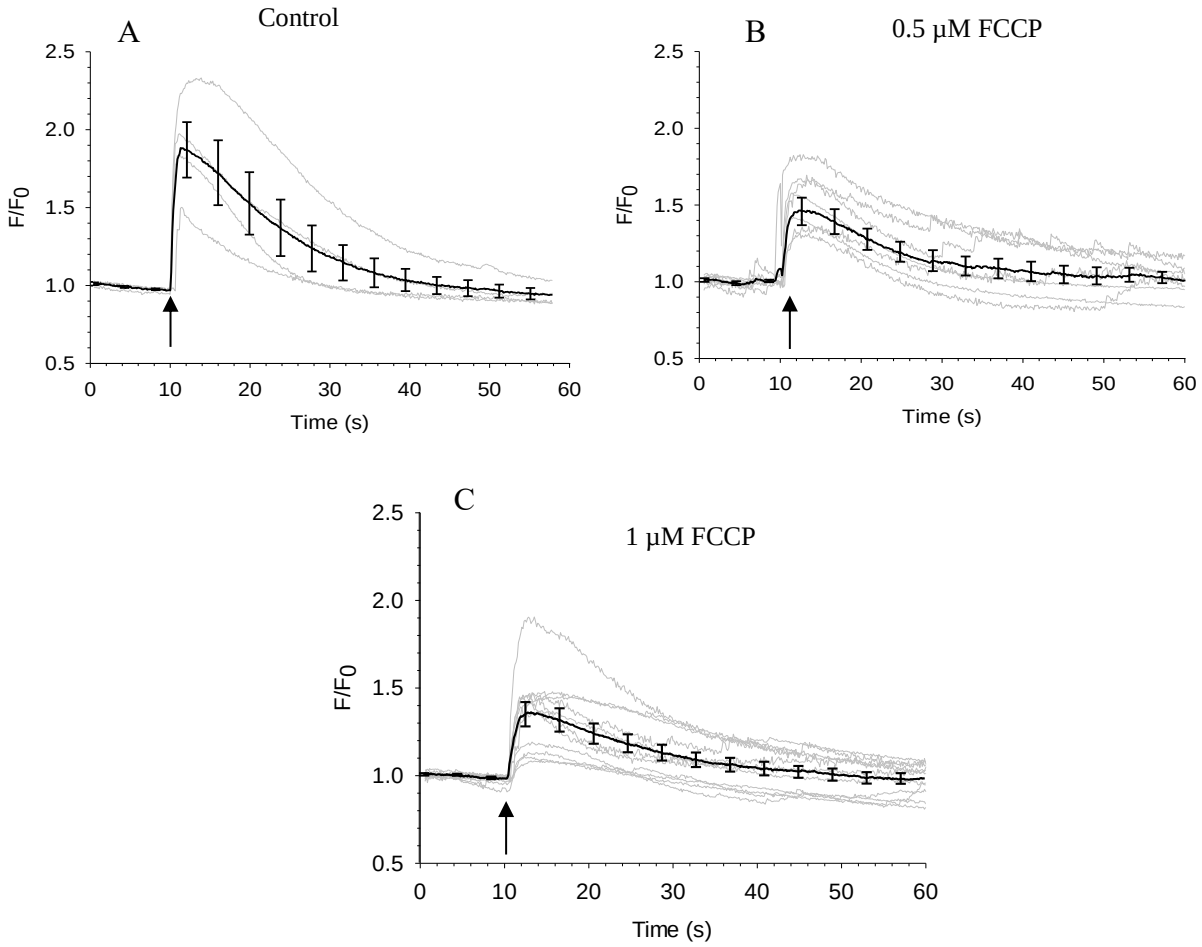

Figure 3.7: Calcium responses of cells treated with FCCP and stimulated with 10 applications of DMPP. Representative fluorescence traces together with the average responses for ten applications of DMPP (100 µM, 10 Hz). A) Control cells (N=4), B) 0.5 µM FCCP-treated cells (N=9), C) 1 µM FCCP-treated cells (N=11). Arrows indicate the time of DMPP delivery.

3.3.3 Effect of CCCP on calcium responses evoked by multiple applications of KCl

High KCl is a stronger depolarizing stimulus compared to DMPP and it was interesting to determine how calcium responses evoked by KCl would be affected by disrupting mitochondrial membrane potential. Chromaffin cells were labeled with

Calcium-Green-1, incubated with 0.5 µM CCCP as described previously and stimulated with five applications of 56 mM KCl at a repetition rate of 1 Hz. As shown in Figure 3.8, KCl-evoked calcium responses in cells treated with 0.5 µM CCCP were significantly decreased in amplitude and had an increased half-width compared to the control cells. These effects were similar to those shown earlier for calcium responses evoked by DMPP. A one-way ANOVA post-hoc Tukey test with a significance level of $p = 0.05$ showed that the p-value for the calcium amplitude and the half-width between the calcium responses of the control cells and CCCP treated cells was $p < 0.05$, indicating statistical significance.

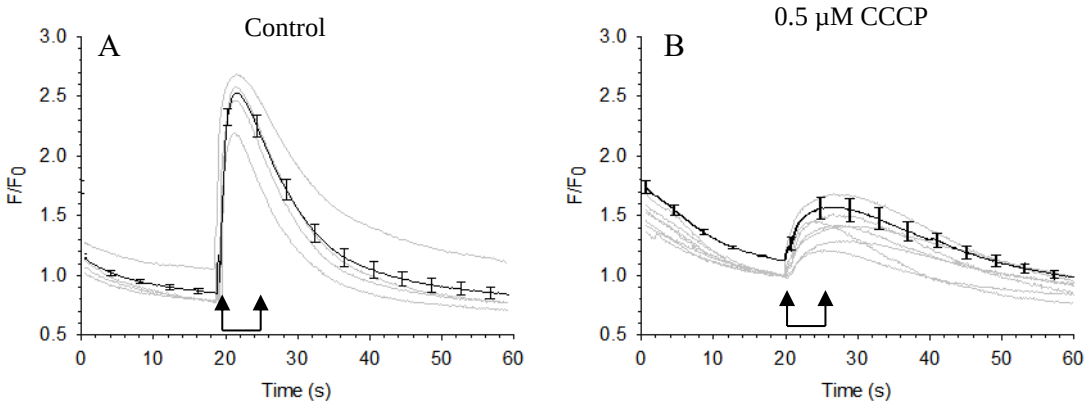

Figure 3.8: Calcium responses in cells treated with 0.5 µM CCCP and stimulated with five applications KCl. Representative fluorescence traces together with the average responses for five applications of KCl (56 mM, 1 Hz). A) Control cells (N=4) and (B) 0.5 µM CCCP-treated cells (N=8). Arrows indicate the time of KCl delivery.

In conclusion, both CCCP and FCCP altered the calcium responses of cells stimulated with either DMPP or KCl to a much greater degree than reported by other groups. However, as stated previously, although variable calcium responses were observed at 0.5 µM, the lowest concentration used in this study, there still may be effects due to

immediate inhibition of the calcium current through VGCCs with a secondary effect on ATP production [13]. As cells remain in the presence of CCCP, a cascade of events associated with disrupting the mitochondria, such as interruption in ATP production and ROS production [15-16], could also impact the calcium response.

3.4 Monitoring changes in mitochondrial membrane potential

3.4.1 Fluorescence imaging of mitochondria

Before experiments got underway, mitochondria were labeled with Mitotracker Green and Mitotracker Orange to determine the optimal conditions for visualizing this organelle using standard widefield fluorescence microscopy. Our frame of reference was a confocal image from the equatorial plane of a bovine chromaffin cell (Figure 3.9) in which mitochondria were labeled with 100 nM Mitotracker Green [17]. The image shows that mitochondria were not clearly defined in shape but appeared as clusters having different fluorescence intensities.

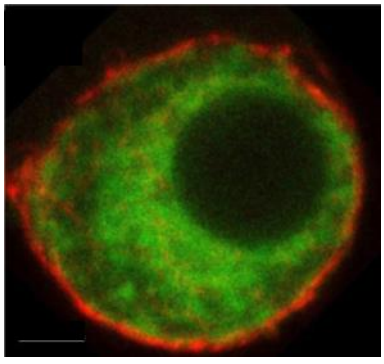

Figure 3.9: Confocal image of a chromaffin cell in which mitochondria were labeled with 100 nM Mitotracker Green. The image, which is from [17], shows an off-center nucleus (dark region) and a non-homogenous distribution of clusters of mitochondria in the cytoplasm (green fluorescence). The cytoskeleton is also shown (red fluorescence). (Adapted with permission from Journal of Cell Science [17], doi: 10.1242/jcs.160242.)

Using the confocal image as a guide, mitochondria were labeled with different concentrations of each dye. As shown in Figure 3.10, A, labeling mitochondria with 200 nM Mitotracker Green resulted in a saturated fluorescence signal. Decreasing the concentration to 100 nM not only reduced fluorescence intensity but yielded images of labeled mitochondrial clusters (Figure 3.10, B) that resembled those obtained by confocal microscopy [17]. Similar results were obtained for the dye Mitotracker Orange at both 50 nM and 20 nM, for TMRE at 25 nM and 20 nM, and for RH 123 at 200 nM and 100 nM (Figure 3.10).

Mitotracker Green was selected to only provide an image of the global population of mitochondria in a chromaffin cell. Although Mitotracker Orange, TMRE, and RH 123 label the mitochondria in the same manner, TMRE and RH 123 are the only dyes considered to be sensitive enough for monitoring changes in mitochondrial membrane potential. Therefore, only TMRE (20 nM) and RH 123 (200 nM) were selected for conducting mitochondrial membrane potential experiments.

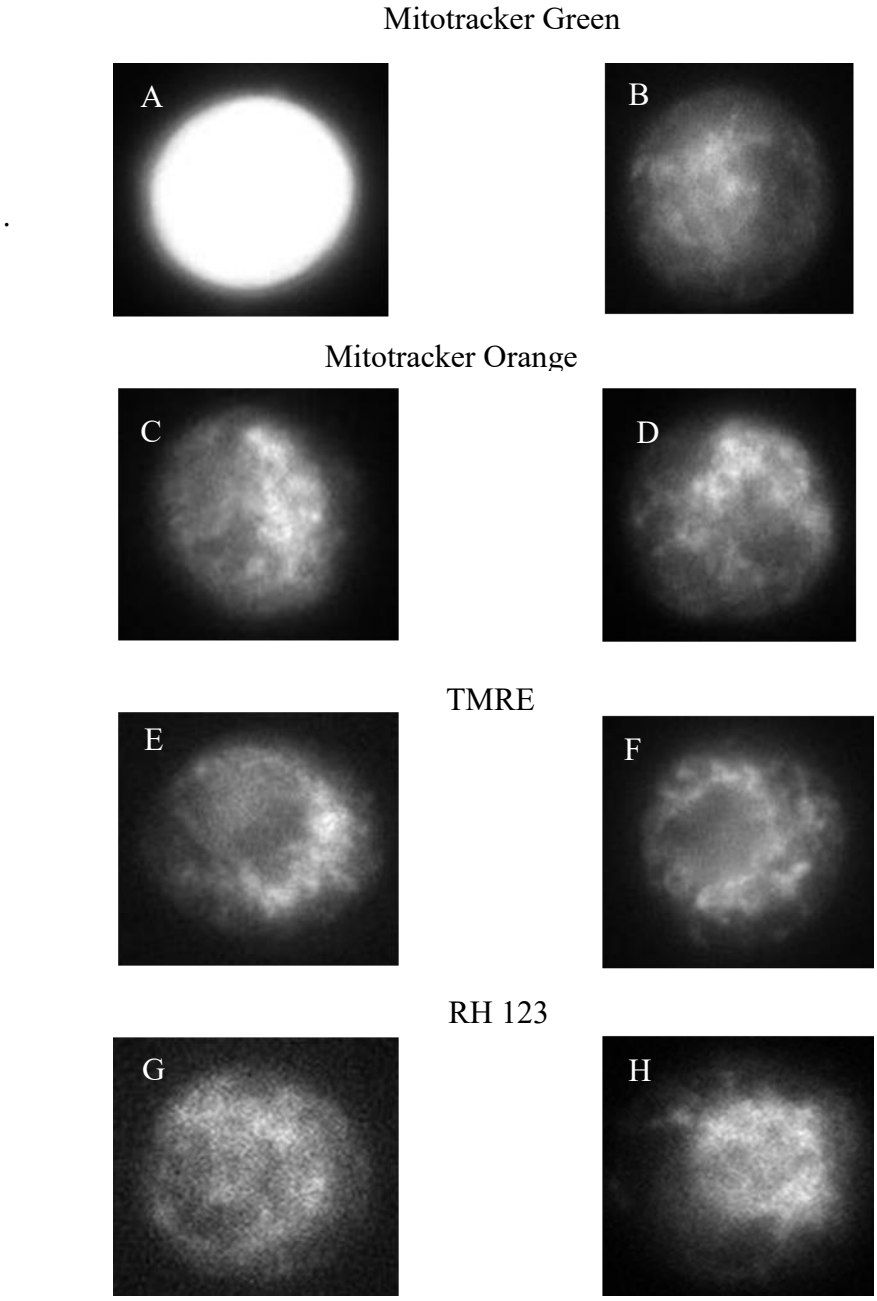

Figure 3.10: Fluorescence images of cells in which mitochondria were labeled with mitochondrial labeling dyes. A) 200 nM Mitotracker Green, B) 100 nM Mitotracker Green, C) 50 nM Mitotracker Orange, D) 20 nM Mitotracker Orange, E) 25 nM TMRE, F) 20 nM TMRE, G) 200 nM RH 123, H) 100 nM RH 123.

3.5 Assessing TMRE and RH 123 fluorescence for photobleaching

After establishing the optimal concentrations of TMRE and RH 123 for labeling mitochondria, we next examined the rate of photobleaching for each dye. As shown in Figure 3.11, TMRE and RH 123 fluorescence traces exhibited different rates of photobleaching that were cell specific. For both dyes, fluorescence traces were sometimes noisy but nevertheless remained linear over the course of a 60 s monitoring period.

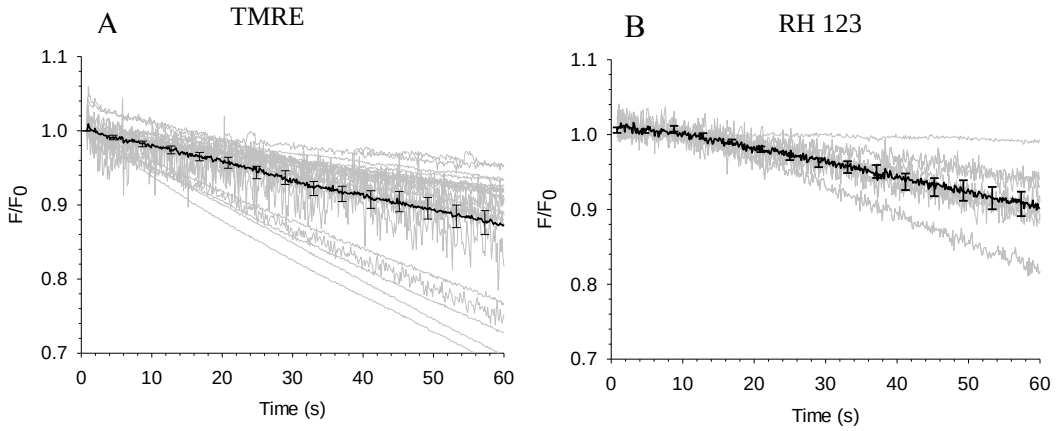

Figure 3.11: Photobleaching of TMRE and RH 123 fluorescence. Representative fluorescence traces together with the average of mitochondria labeled with A) 20 nM TMRE (N=24) and B) 200 nM RH 123 (N=10).

3.6 Monitoring changes in mitochondrial membrane potential in cells treated with CCCP

The effects of 5 ns pulses on mitochondria were studied by delivering single or multiple pulses (five or ten pulses at repetition rate of 10 Hz) at the following electric field magnitudes: 5 MV/m, 10 MV/m, and 15 MV/m. As a control to establish that a decrease

in fluorescence correlated with mitochondrial membrane potential disruption, TMRE and RH 123 labeled cells were perfused with CCCP at concentrations of 1 µM, 2 µM, 8 µM, or 10 µM. The time it took for CCCP to reach the cells was determined by perfusing Calcium Green-1 labeled cells with 100 µM DMPP at a flow rate of 1.1-1.2 ml/min. As shown in Figure 3.12, DMPP reached the cells around 30 s after the BSS containing DMPP was delivered to the cells. On general, this interval varied from 20 to 30 s. Afterwards, CCCP was perfused at a flow rate of 1.1-1.2 mL/min. Figure 3.13 is a schematic showing how CCCP was perfused to cells labeled with TMRE or RH 123.

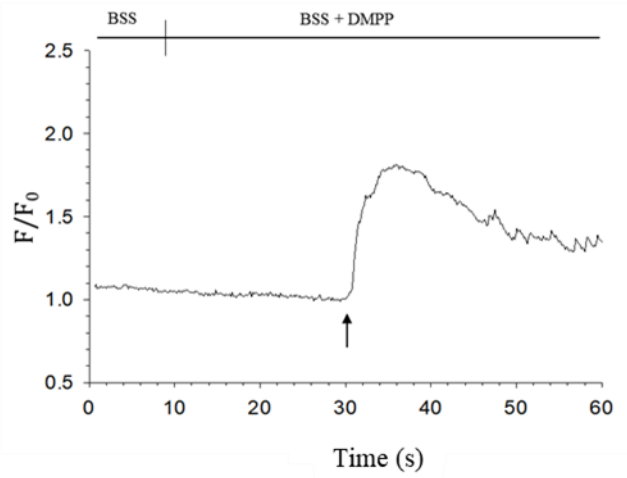

Figure 3.12: Calcium response to DMPP delivered to the cells by perfusion. Representative calcium response of a cell stimulated with 100 µM DMPP. BSS was perfused for the first 5 s followed by switching to a BSS solution containing DMPP. The arrow indicates when DMPP reached the cell.

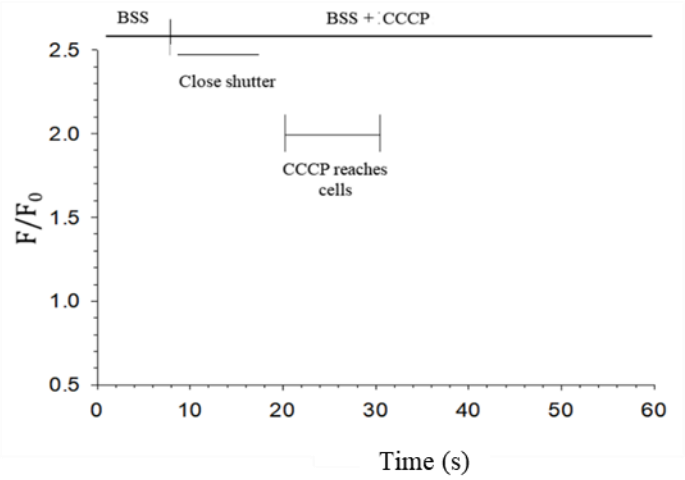

Figure 3.13: Schematic diagram showing the procedure used for perfusing Calcium Green-1 labeled cells with CCCP. BSS was perfused for the first 5 s followed by immediate closure of the shutter for 5 s (to minimize photobleaching) and switching from BSS to BSS containing CCCP, where CCCP reached the cells around 20-30 s during the monitoring period.

Control fluorescence traces for both TMRE and RH 123 labeled cells are shown in Figure 3.14. TMRE and RH 123 fluorescence remained linear throughout the monitoring period with no perturbations in the linearity in TMRE fluorescence at the time when, in an actual experiment, CCCP would reach the cells after the valve would be switched. In this series of experiments, however, there was more photobleaching of RH 123 fluorescence compared to TMRE fluorescence.

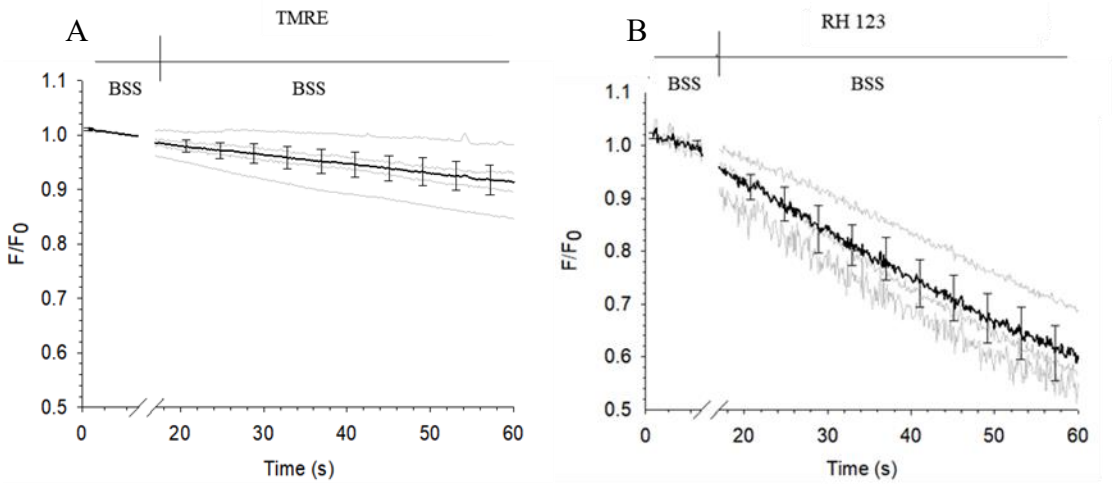

Figure 3.14: Fluorescence traces of TMRE and RH 123 labeled-mitochondria during cell perfusion. Representative fluorescence traces together with the average for mitochondria labeled with TMRE or RH 123. Cells were perfused with BSS at a fow rate of 1.1-1.2 ml/min during the first 5 s, followed by switching the valve to a different BSS reservoir and closing the shutter for 5 s (indicated by the break in the time scale). A) TMRE-labeled cells (N=4), B) RH 123 labeled cells (N=3).

Having established the control traces for TMRE and RH 123 fluorescence over a 40 s monitoring period, CCCP was perfused to TMRE and RH 123 labeled cells at the following concentrations: 1 µM, 2 µM, 8 µM, or 10 µM.

At 1 µM CCCP, there was no effect on TMRE (N=0/4) or RH 123 (N=0/3) fluorescence and the traces were similar to the control traces (results not shown). When the concentration of CCCP was increased to 2 µM, again there was no change in the fluorescence (results not shown). At 8 µM, however, CCCP caused a continuous decrease in TMRE fluorescence in 3 out of 3 cells, (Figure 3.15, A) with an average decrease of 32% over the course of 20 s (that is, from the time the decrease begins until the end of the monitoring period). However, there was no change in fluorescence in RH 123 labeled cells (Figure 3.15, B), suggesting that TMRE is a more sensitive dye for monitoring changes in mitochondrial membrane potential. To assess this further, the concentration of CCCP was

increased to 10 µM. While TMRE fluorescence (N=4/5) underwent a decrease in fluorescence of similar magniute as 8 µM, RH 123 fluorescence remained unchanged (N=0/4).

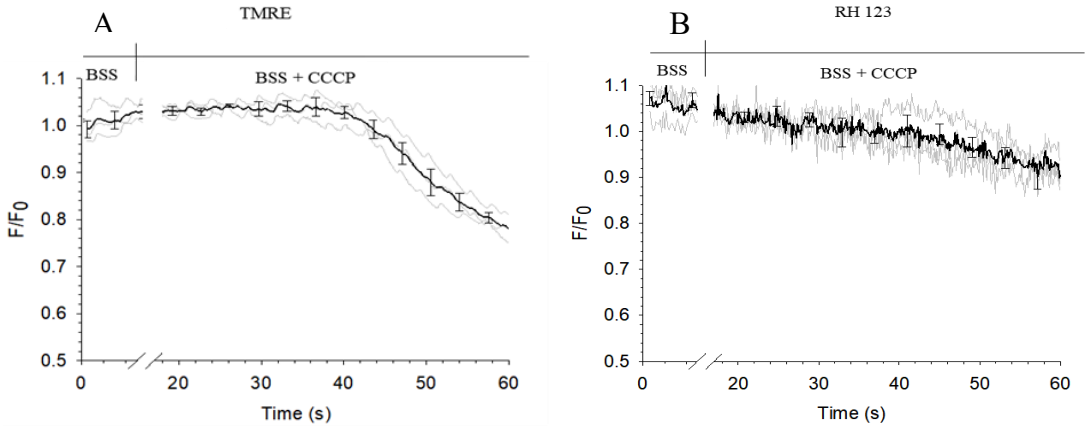

Figure 3.15: Fluorescence traces of TMRE and RH 123 labeled mitochondira during cell perfusion with 8 µM CCCP. Cells were perfused at a fow rate of 1.1-1.2 ml/min with BSS during the first 5 s, followed by switching the valve to BSS containing CCCP and closing the shutter for 5 s (indicated by the break in the time scale). A) TMRE fluorescence traces (N=3), B) RH 123 fluorescence traces (N=3).

From these results, it can be concluded that high concentrations of CCCP are required to cause a consistent decrease in TMRE fluorescence (summarized in Table 2). Because RH 123 fluorescence was unaffected by CCCP, all subsequent experiments to examine stimulus-evoked decreases in mitochondrial membrane potential were carried out in cells in which mitochondria were labeled with TMRE.

Table 2: Summary of the percent decrease in TMRE fluorescence in response to CCCP.

CCCP (Concentration)	Average decrease in fluorescence ± SE (%)
8 µM (N=3/3)	32.7 ± 1.8
10 µM (N=4/5)	26.8 ± 6.1

3.7 Effect of DMPP on TMRE fluorescence

A change in mitochondrial membrane potential would cause dissipation of TMRE dye molecules, causing a decrease in fluorescence either immediately or a few seconds after application of a stimulus. As a control to determine if a strong physiological stimulus would cause a disruption in mitochondrial membrane potential, TMRE labeled cells were stimulated with ten applications of 100 µM DMPP at a repetition rate of 10 Hz. Figure 3.16 shows that the stimulus caused a small drop in fluorescence that unlike the decrease caused by CCCP, was not sustained. The decrease in fluorescence, however, was observed in only 4 out of 17 cells.

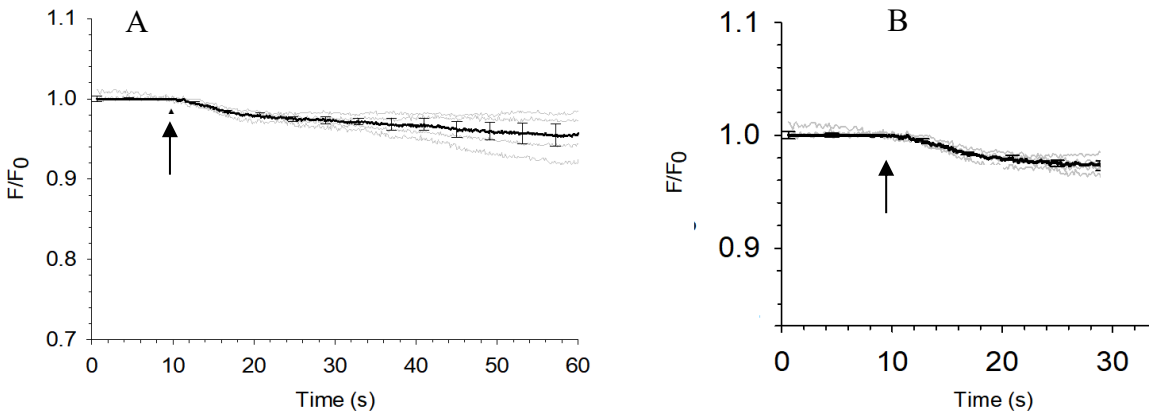

Figure 3.16: Traces of TMRE fluorescence in cells exposed to ten applications (10 Hz) of DMPP. A) Representative fluorescence traces together with the average response (N=4). B) An enlarged view of the drop in fluorescence is shown on the right. The arrows indicate the time at which DMPP was applied.

The average decrease in fluorescence shown in Figure 3.16 was 1.5% and was quantified as shown in Figure 3.17 using whole cell fluorescence. Essentially, the fluorescence intensity at the point where fluorescence stablized after the drop, ~25 s, was subtracted from the fluorescence intensity at 10 s, the time the stimulus was applied. To account for differences in TMRE photobleaching rates (Figures 3.11 and 3.14), we used a line substraction tool in the Origin Pro software. The fluorescence traces were graphed in Origin Pro and the photobleaching rate for the first 10 s of the monitoring period (before application of a stimulus) was subtracted from the fluorescence trace from 11 s to 60 s. An example is shown in Figure 3.18.

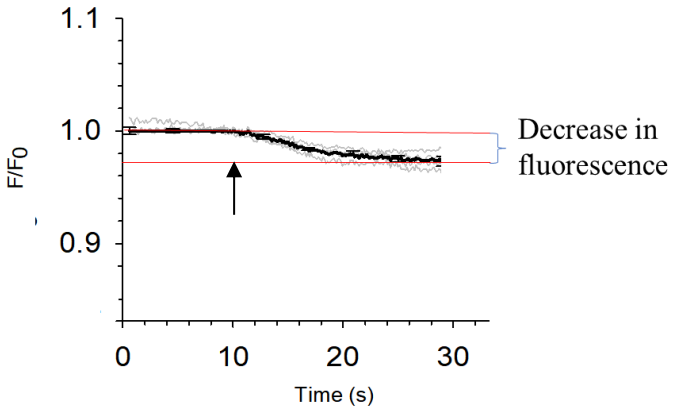

Figure 3.17: Analysis of decreases in TMRE fluorescence in response to a stimulus. The percent decrease was determined by subtracting the lowest fluorescence value between 10-25 s from the normalized fluorescence.

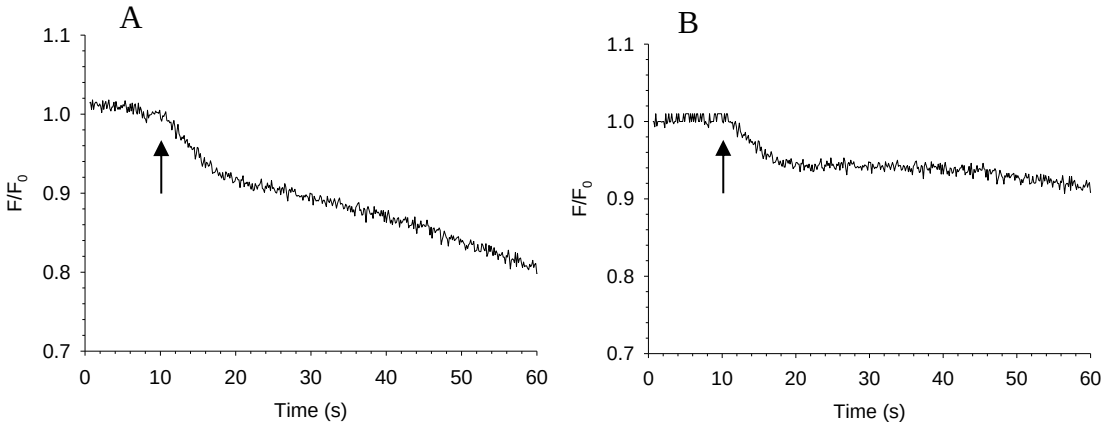

Figure 3.18: Fluorescence trace corrected for photobleaching. TMRE fluorescence trace before A) and after B) correction for photobleaching. The arrow indicates the time at which the stimulus was applied.

3.8 Assessing changes in TMRE fluorescence - whole cell fluorescence vs. fluorescence of mitochondrial clusters

As shown earlier in Figure 3.10, mitochondria labeled with TMRE appeared as bright fluorescent clusters that were not homogeneously distributed in the cell. Given the small decrease in TMRE fluorescence in response to DMPP, we wanted to determine how

analyzing changes in TMRE fluorescence would be affected by the presence of those regions of the cell that were not fluorescent. Hence, three different analyses were carried out to determine the best strategy for assessing changes in mitochondrial membrane potential. As shown in Figure 3.18, comparisons of changes in TMRE fluorescence included assessing whole cell fluorescence, a brightly-labeled mitochondrial cluster, and a region of the cell that included part of a labeled mitochondrial cluster with a non-fluorescent region. The results, which are shown in Figure 3.19 in which the three fluorescence traces were superimposed, showed no significant differences. We did find, however, that using whole cell fluorescence resulted in less noise. Therefore, it was decided to continue assessing mitochondrial membrane potential changes by analyzing whole cell fluorescence.

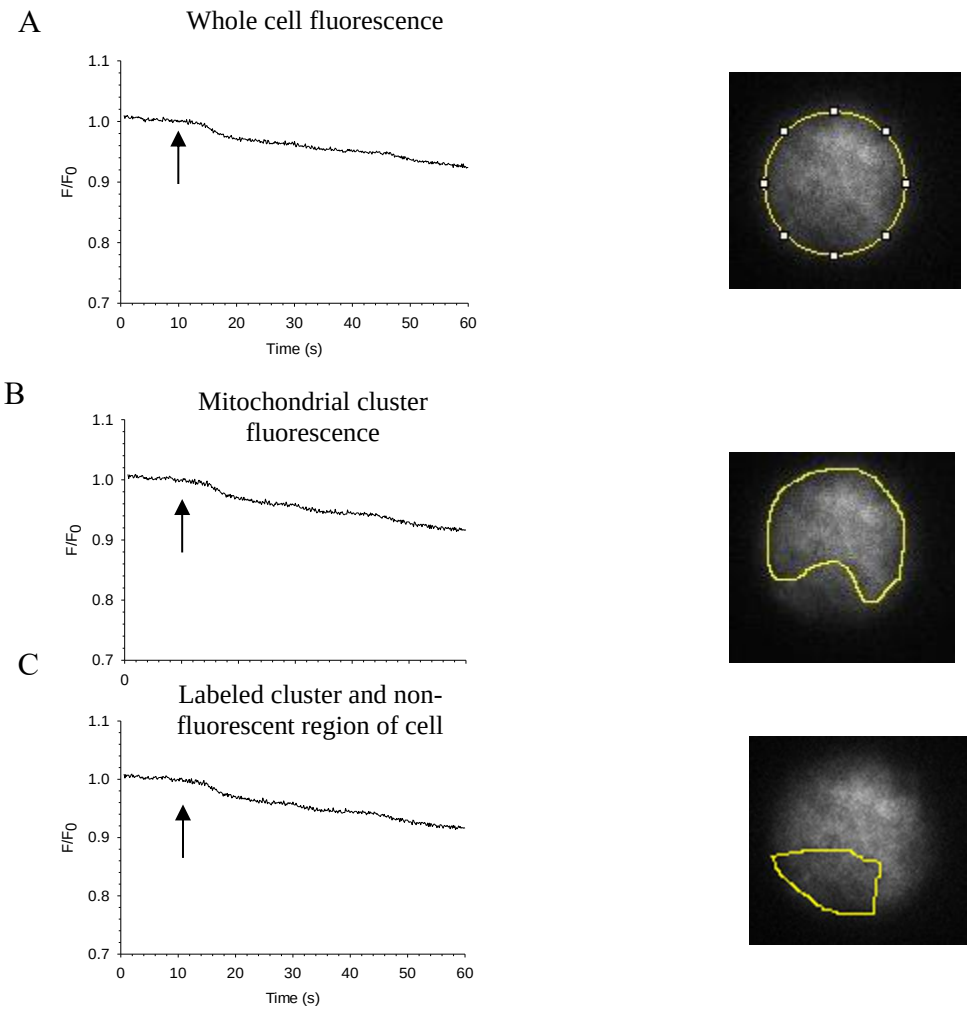

Figure 3.19: Analysis of changes in TMRE fluorescence using different regions of interest. Shown on the left are the fluorescence traces and on the right are enlarged views of the regions of the cell selected for the analysis (outlined in yellow). A) Whole cell fluorescence, B) mitochondrial cluster fluorescence, C) labeled cluster and non-fluorescent region. The arrow indicates when the stimulus was applied to the cells.

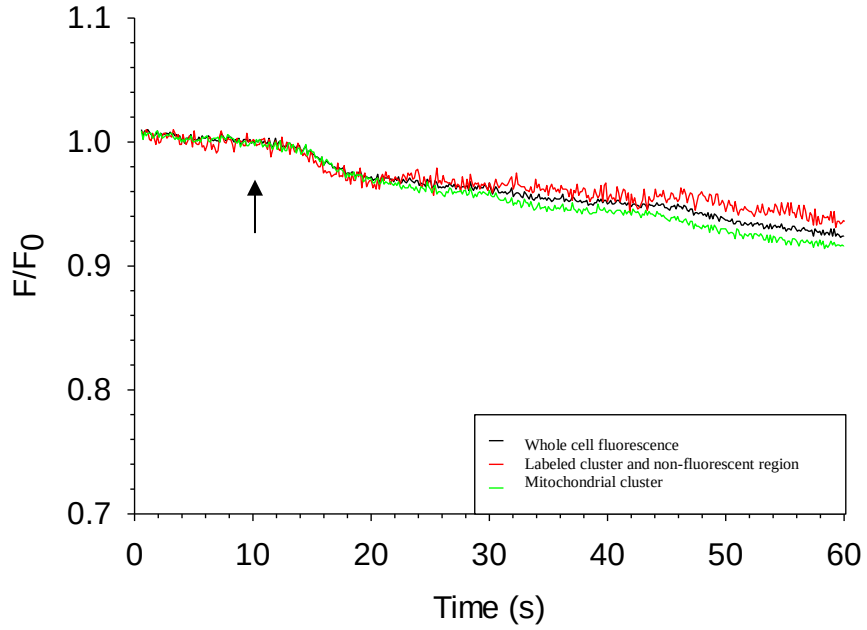

Figure 3.20: Superimposed fluorescence traces of changes in TMRE analyzed by different methods. The superimposed traces are from Figure 3.19.

3.9 Monitoring changes in mitochondrial membrane potential in response to 5 ns pulses

3.9.1 Effect of a single 5 ns, 5 MV/m pulse on TMRE fluorescence

Cells in which mitochondria were labeled with TMRE were stimulated with a single 5 ns pulse at 5 MV/m and the results are shown in Figure 3.21. There was no discernible decrease in TMRE fluorescence in any of the exposed cells (N=17), indicating that a single pulse had no effect on the mitochondrial membrane potential. From these results we concluded that the long-lived duration of calcium responses evoked by a 5 ns, 5 MV/m pulse were not due to a disruption of mitochondrial membrane potential.

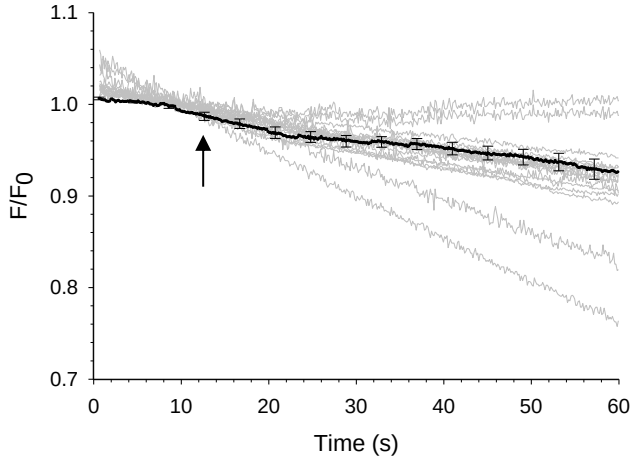

Figure 3.21: Traces of TMRE fluorescence in cells exposed to a single pulse (5 MV/m). Representative fluorescence traces together with the average response (N=17). The arrow indicates the time at which the pulse was applied.

3.9.2 Effect of multiple 5 ns, 5 MV/m pulses on TMRE fluorescence

Given that a single 5 ns pulse at 5 MV/m had no effect on TMRE fluorescence, we next increased the number of pulses to which cells were exposed. Figure 3.23 shows the results when TMRE labeled cells were stimulated with five pulses (10 Hz). In around 31% of the cells (N=4/13), there was an average decrease in TMRE fluorescence of 1.6% that resembled the decrease observed with multiple applications of DMPP (Figure 3.1.6). That is, there was a small drop in fluorescence after the stimulus that was not sustained. Thus, even with multiple pulses there was minimal mitochondrial membrane potential disruption.

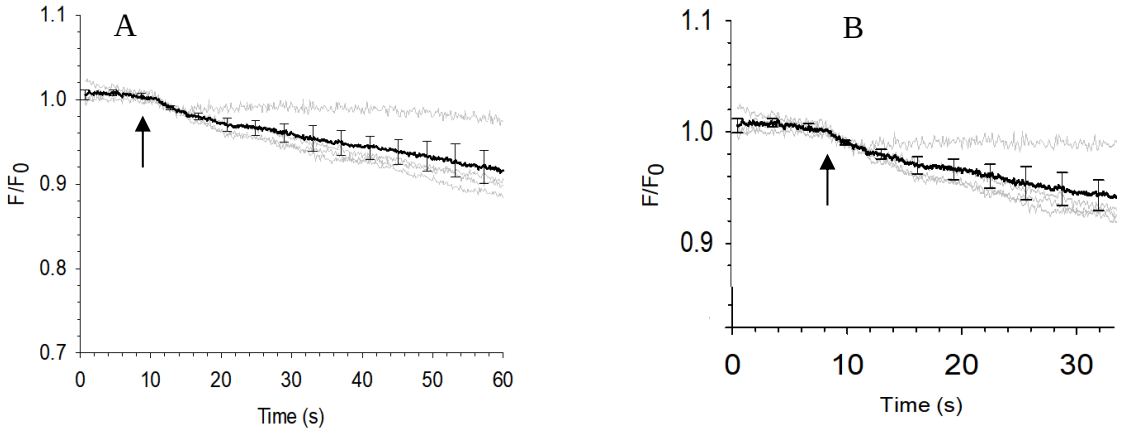

Figure 3.22: Traces of TMRE fluorescence in cells exposed to five pulses. A) Representative fluorescence traces together with the average response (N=4). B) An enlarged view of the drop in fluorescence. The arrow indicates the time at which the pulses were applied.

When TMRE labeled cells were exposed to ten pulses (10 Hz), 60% of the cells (N=9/15) showed a decrease in fluorescence immediately at the end of the pulse train (Figure 3.24). However, the average decrease in TMRE fluorescence under these conditions was only 1.9% and still not very pronounced.

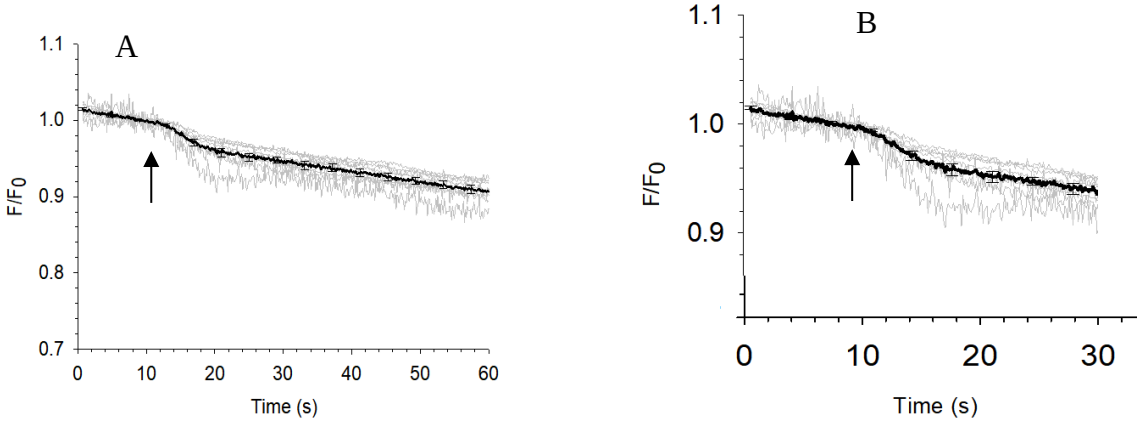

Figure 3.23: Traces of TMRE fluorescence in response to ten pulses. A) Representative fluorescence traces together with the average response (N=9). B) An enlarged view of the drop in fluorescence. The arrow indicates the time at which the pulses were applied.

3.9.3 Effect of a single 5 ns pulse at 10 and 15 MV/m on TMRE fluorescence

Since multiple applications of 5 ns pulses at 5 MV/m were shown to cause in some cells minor changes in TMRE fluorescence, and hence a minor change in mitochondrial membrane potential, we next determined the effect of increasing the electric field magnitude from 5 MV/m to 10 and 15 MV/m. As shown in Figure 3.24, single pulses at these higher electric field magnitudes evoked very sustained increases in intracellular calcium.

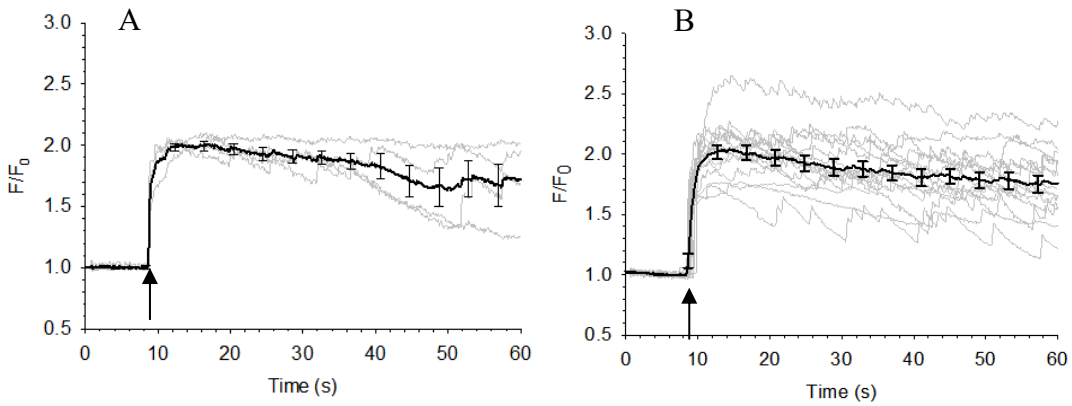

Figure 3.24: Calcium responses in cells stimulated with a single 5 ns pulse at 10 MV/m and 15 MV/m. Representative fluorescence traces together with the average responses in cells exposed to a pulse at A) 10 MV/m (N=4) and (B) 15 MV/m (N=14). The arrow indicates the time at which the pulse was applied.

When TMRE labeled-cells were exposed to a single 5 ns pulse at 10 MV/m, (Figure 3.26, A), there was an average decrease of 2.0% in TMRE fluorescence in 44% (N=4/9) of the cells. Increasing the amplitude of the electric field to 15 MV/m caused a similar average decrease of 1.8% in TMRE fluorescence in 50% (N=8/16) of the cells (Figure 3.26, B). These results further support the conclusion that the long-lived duration of calcium

responses evoked by 5 ns pulses does not involve a disruption of mitochondrial membrane potential.

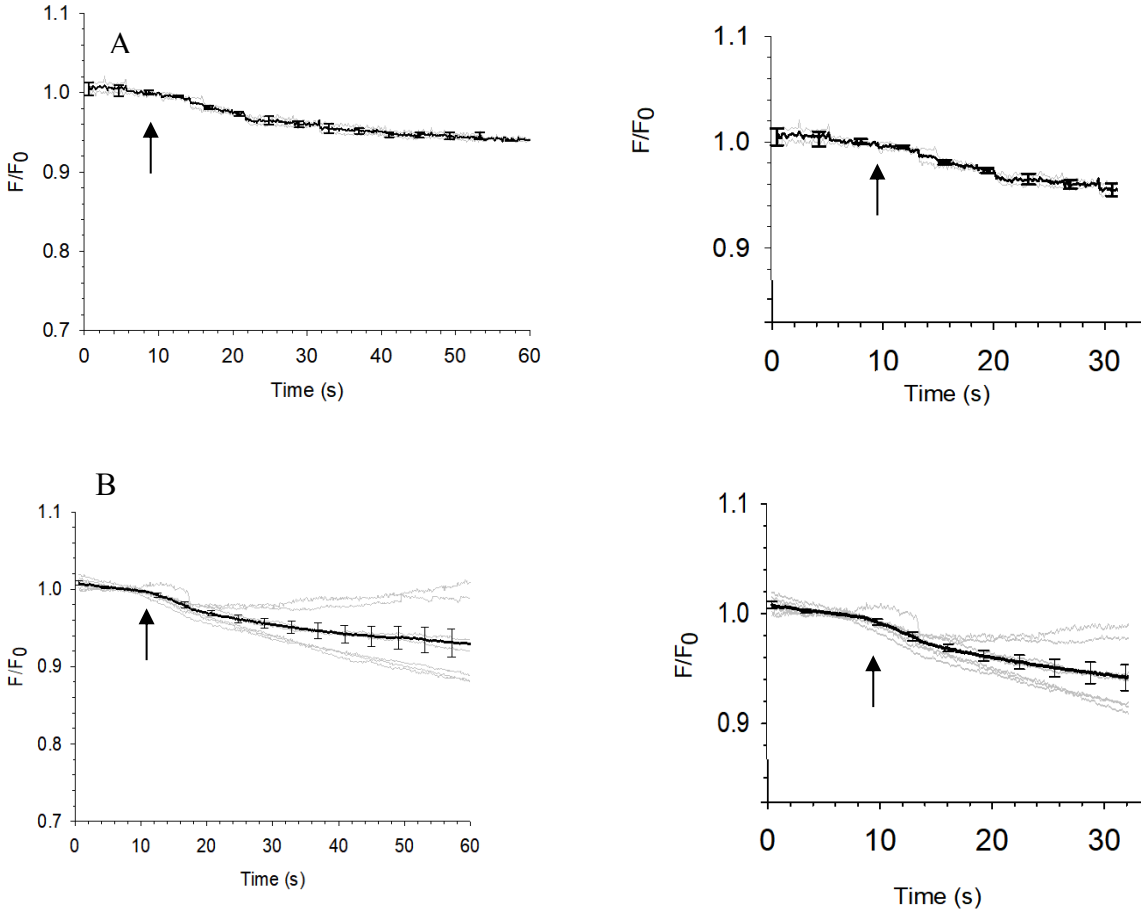

Figure 3.25: Traces of TMRE fluorescence in cells exposed to a 5 ns pulse at electric fields great than 5 MV/m. Representative fluorescence traces together with the average responses in cells exposed to a 5 ns pulse at A) 10 MV/m (N=4) and (B) 15 MV/m (N=8). An enlarged view of the drop in fluorescence is shown on the right of each graph. The arrow indicates the time at which the pulse was applied.

A one-way ANOVA pos hoc Tukey analysis with a p = 0.05 was conducted to analyze for the significance of differences in the decrease in fluorescence in TMRE labeled cells. The analysis showed that there was no statsitical significance in the percent decrease

in fluorescence for TMRE labeled cells for each stimulus (DMPP and pulses) and the applied electric field. Table 3 summarizes the results obtained for each stimulus.

Table 3: Summary of the decrease in TMRE fluorescence in response to 5 ns pulses and DMPP

Stimulus	Cells Responding		Decrease in Fluorescence ± SE (%)
10 applications (10 Hz) of 100 µM DMPP	Decrease	N = 4/17	1.5 ± 0.2
	No Decrease	N = 13/17	0
1 pulse (5 MV/m)	Decrease	N = 0/17	0
	No Decrease	N = 17/17	0
5 pulses (10 Hz, 5 MV/m)	Decrease	N = 4/13	1.6 ± 0.2
	No Decrease	N = 9/13	0
10 pulses (10 Hz, 5 MV/m)	Decrease	N = 9/15	1.9 ± 0.4
	No Decrease	N = 615	0
10 MV/m (1 pulse)	Decrease	N = 4/9	2.0 ± 0.0
	No Decrease	N = 5/9	0
15 MV/m (1 pulse)	Decrease	N = 7/16	1.8 ± 0.2
	No Decrease	N = 9/16	0

3.11 Summary and Conclusions

This study has shown that a single 5 ns, 5 MV/m pulse evokes longer-liver calcium responses than those evoked even by multiple applications of the nicotinic cholinergic receptor agonist DMPP. Based on the results presented here, the mechanism involved does not appear to be due to a disruption of mitochondrial membrane potential since a single pulse had no effect on TMRE fluorescence. Moreover, TMRE fluorescence was only

minimally decreased in a fraction of the cells exposed to five or ten pulses, or in response to a single pulse delivered at higher electric field amplitudes, exposure conditions that produce even more prolonged increases in intracellular calcium than a single, 5 MV/m pulse. In fact, the magnitude of the decrease in TMRE fluorescence observed under these exposure conditions was similar to that observed in response to multiple applications of DMPP. From these results we conclude that other mechanisms affecting intracellular calcium levels are involved that will require further investigation. As stated earlier, these include the effects of a 5 ns pulse on the duration of calcium entry through VGCCs, the time course of the release of calcium from the ER, and the activity of the plasma membrane Na^{+}/Ca^{2+} exchanger and calcium ATPase, the enzymes responsible for calcium extrusion from chromaffin cells.

As for the method used to assess disruption of mitochondrial membrane potential, it should be pointed out that a relatively high concentration of CCCP (8 μM) was required to cause a decrease in TMRE fluorescence (i.e., mitochondrial membrane potential), contrasting with a concentration of only 0.5 μM that was sufficient to significantly alter calcium responses to depolarizing stimuli. Thus, we cannot fully rule out the possibility that our method of detection may not have been sensitive enough. Nevertheless, our results overall suggest that 5 ns pulses do not have toxic effects on mitochondrial function.

References

[1] Contreras, L., Drago, I., Zampese, E. and Pozzan, T. (2010). Mitochondria: The calcium connection. *Biochimica et Biophysica Acta (BBA) - Bioenergetics*, 1797(6-7), pp.607-618.

[2] García-Sancho, J., de Diego, A. and García, A. (2012). Mitochondria and chromaffin cell function. *Pflügers Archiv - European Journal of Physiology*, 464(1), pp.33-41.

[3] García, A., Padín, F., Fernández-Morales, J., Maroto, M. and García-Sancho, J. (2012). Cytosolic organelles shape calcium signals and exo–endocytotic responses of chromaffin cells. *Cell Calcium*, 51(3-4), pp.309-320.

[4] Santo-Domingo, J. and Demaurex, N. (2010). Calcium uptake mechanisms of mitochondria. *Biochimica et Biophysica Acta (BBA) - Bioenergetics*, 1797(6-7), pp.907-912.

[5] J. García-Sancho and A. Verkhratsky, "Cytoplasmic organelles determine complexity and specificity of calcium signalling in adrenal chromaffin cells," *Acta Physiologica*, vol. 192, no. 2, pp. 263–271, 2007.

[6] J. Zaklit, G. L. Craviso, N. Leblanc, L. Yang, P. T. Vernier, and I. Chatterjee, "Adrenal Chromaffin Cells Exposed to 5-ns Pulses Require Higher Electric Fields to Porate Intracellular Membranes than the Plasma Membrane: An Experimental and Modeling Study," *The Journal of Membrane Biology*, vol. 250, no. 5, pp. 535–552, 2017.

[7] G. L. Craviso, S. Choe, P. Chatterjee, I. Chatterjee, and P. T. Vernier, "Nanosecond Electric Pulses: A Novel Stimulus for Triggering Ca^{2+} Influx into Chromaffin Cells Via Voltage-Gated Ca^{2+} Channels," *Cellular and Molecular Neurobiology*, vol. 30, no. 8, pp. 1259–1265, 2010.

[8] G. L. Craviso, S. Choe, I. Chatterjee, and P. T. Vernier, “Modulation of intracellular Ca^{2+} levels in chromaffin cells by nanoelectropulses,” *Bioelectrochemistry*, vol. 87, pp. 244–252, 2012.

[9] G. Craviso, P. Chatterjee, G. Maalouf, A. Cerjanic, J. Yoon, I. Chatterjee, and P. Vernier, “Nanosecond electric pulse-induced increase in intracellular calcium in adrenal chromaffin cells triggers calcium-dependent catecholamine release,” *IEEE Transactions on Dielectrics and Electrical Insulation*, vol. 16, no. 5, pp. 1294–1301, 2009.

[10] I. Cuchillo-Ibáñez, T. Lejen, A. Albillos, S. D. Rosé, R. Olivares, M. Villarroya, A. G. García, and J.-M. Trifaró, “Mitochondrial calcium sequestration and protein kinase C cooperate in the regulation of cortical F-actin disassembly and secretion in bovine chromaffin cells,” *The Journal of Physiology*, vol. 560, no. 1, pp. 63–76, 2004.

[11] Yang, D. and Kao, L. (2008). Relative contribution of the Na^{+}/Ca^{2+} exchanger, mitochondria and endoplasmic reticulum in the regulation of cytosolic Ca^{2+} and catecholamine secretion of bovine adrenal chromaffin cells. *Journal of Neurochemistry*, 76(1), pp.210-216.

[12] Alés, E., Fuentealba, J., García, A. and López, M. (2005). Depolarization evokes different patterns of calcium signals and exocytosis in bovine and mouse chromaffin cells: the role of mitochondria. *European Journal of Neuroscience*, 21(1), pp.142-150.

[13] J. M. Hernández-Guijo, V. E. Maneu-Flores, A. Ruiz-Nuño, M. Villarroya, A. G. García, and L. Gandía, “Calcium-Dependent Inhibition of L, N, and P/Q Ca^{2+} Channels in Chromaffin Cells: Role of Mitochondria,” *The Journal of Neuroscience*, vol. 21, no. 8, pp. 2553–2560, 2001.

[14] D. R. Giovannucci, M. D. Hlubek, and E. L. Stuenkel, “Mitochondria Regulate the Ca^{2+} –Exocytosis Relationship of Bovine Adrenal Chromaffin Cells,” *The Journal of Neuroscience*, vol. 19, no. 21, pp. 9261–9270, 1999.

[15] N. Demaurex, D. Poburko, and M. Frieden, “Regulation of plasma membrane calcium fluxes by mitochondria,” *Biochimica et Biophysica Acta (BBA) - Bioenergetics*, vol. 1787, no. 11, pp. 1383–1394, 2009.

[16] S. W. Perry, J. P. Norman, J. Barbieri, E. B. Brown, and H. A. Gelbard, “Mitochondrial membrane potential probes and the proton gradient: a practical usage guide,” *BioTechniques*, vol. 50, no. 2, pp. 98–115, 2011.

[17] J. Villanueva, S. Viniegra, Y. Gimenez-Molina, V. Garcia-Martinez, G. Exposito-Romero, M. D. M. Frances, J. Garcia-Sancho, and L. M. Gutierrez, “The position of mitochondria and ER in relation to that of the secretory sites in chromaffin cells,” *Journal of Cell Science*, vol. 127, no. 23, pp. 5105–5114, 2014.

Chapter 4: Numerical modeling methods

4.1 Introduction

For any exposure system in which electric fields are applied *in vitro,* the electric field should be homogenous in the region containing the cell and homogeneous to within 30% over larger distances [1]. This is important because large deviations in homogeneity can result in variable biological responses, which in turn can impose difficulty in reproducing experimental results [1]. In our laboratory, applying 5 ns, 5 MV/m pulses to adrenal chromaffin cells using two different exposure systems resulted in calcium responses that differed in duration, as discussed in the Introduction. Hence, in this study we used more refined simulation techniques than those used previously to investigate if the variable calcium responses were due to differences in the electric field at the location of the cell [2-3].

The distribution of the electric field magnitude can be computed utilizing SEMCAD, a software program that computes Maxwell's electromagnetic equations using the FDTD method [4-7]. As a control for establishing that the geometries of the simulations were consistent in producing the same computed electric field results as previously performed in our laboratory, a 5 ns pulse was used as an input signal for both exposure systems to compute the electric field distribution in the region containing a chromaffin cell in experiments. For determining and comparing the homogeneity in the electric field distribution of both exposure systems, we used the Huygens box approach to perform refined simulations with reduced simulation time of the electric field in the region

containing the cell. As mentioned earlier (Sections 1.7.1-1.7.2), previous simulations in the laboratory performed with a coarse mesh (a step size of 16 µm for the region containing the cell) had shown that the electric field magnitude was homogeneous in both exposure systems. The Huygens box approach in SEMCAD has the ability to decrease simulation time and require less computer memory while providing results with finer discretization. However, simulations were limited to CPU, graphic processor unit (GPU), the spatial resolution of the Huygens box, and to single frequency simulations. Hence, only a single frequency simulation was performed with the Huygens box, which was selected from the Fourier transform of the 5 ns electric pulse.

4.2 Electric field simulations

Three-dimensional geometrical models of the exposure systems were created in SEMCAD and each of the numerical computations described below computed the electric field magnitude and the direction of propagation. As stated above, control simulations were performed using the 5 ns electric pulse used in our laboratory as the input signal, and the Huygens box was used to determine homogeneity in the electric field distribution in the region containing the cell. The following sections discuss the geometrical models of the two exposure systems, Huygens box simulations of each exposure system at a single frequency, and tables which include the input values for each region in the geometrical model and the sensors used.

4.3 Fourier transform of the 5 ns electric pulse

A single frequency for the Huygens box simulation was selected from the Fourier transform (FT) of the 5 ns pulse. Figure 4.1, A shows the 5 ns pulse used in experiments in our laboratory and Figure 4.1, B shows the FT of the 5 ns pulse generated using MATLAB. The FT takes the 5 ns electric pulse in the time domain and converts it into the frequency domain, displaying the distribution of the frequencies in the pulse. A frequency of 60 MHz was selected to perform the simulations for both exposure systems. It was important to select a frequency that encompasses most of the pulse's energy, and this was determined by using Parseval's theorem to calculate the upper end of the frequency spectrum within which 99% of the energy is contained. Parseval's theorem states that the energy of the signal is the same in both the time and frequency domains [8]. According to calculations performed with Parseval's theorem in MATLAB, 99% of the 5 ns electric pulse's energy was contained at frequencies up to 60 MHz. However, due to the spatial resolution limitation of the Huygens box, numerical simulations below 60 MHz were not achievable.

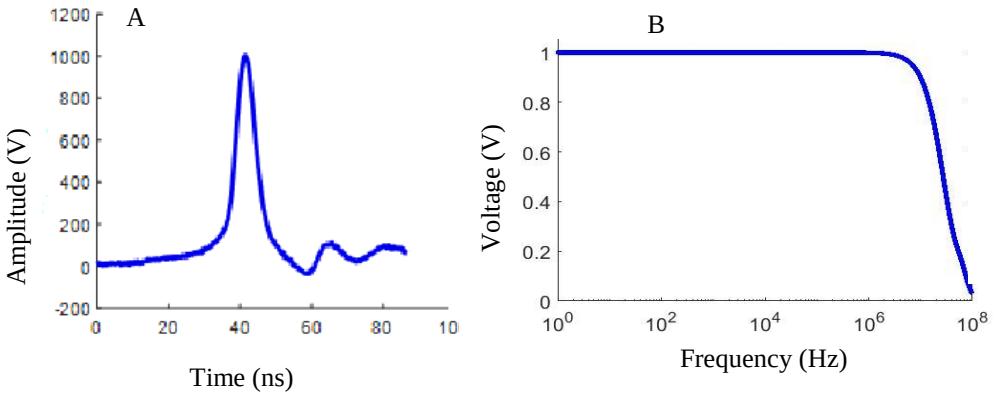

Figure 4.1: FT of the 5 ns electric pulse. A) 5 ns electric pulse. B) FT of the 5 ns electric pulse shows that the maximum bandwidth is 100 MHz (the bandwidth that is covered by the entire FT of the pulse as shown in (A).

The first step in examining homogeneity in the electric field distribution in the region containing the cell was to create geometric models of the two exposure systems.

4.4 Geometrical model of the gold strip exposure chamber

The geometry of the gold strip chamber created in SEMCAD followed the description in [3,9-11] and is shown in Figure 4.2. The geometry consisted of a longitudinal glass slide (length 75 mm, width 25 mm, thickness 1.0 mm**)**, two parallel gold strips (length 40 mm, width 5 mm, thickness 0.025 mm), deposited onto the slide with a spacing of 0.10 mm between them, and a thin square coverslip placed over the gold strips (length 17.2 mm, width 21.1 mm, thickness 0.172 mm). The chromaffin cell was represented as a cube (length 0.016 mm, width 0.016 mm, height 0.016 mm) with diameters matching that of a real chromaffin cell, placed centrally in between the electrodes. This is the region where

the cell would be located during an experiment for exposure to an electric field. BSS was placed between the parallel gold strips as a longitudinal rectangle (length of 21.1 mm, width of 0.10 mm, and height of 0.025 mm) between the gold strips, covering the 0.10 mm gap. The edge source and 50 Ω lumped element were connected in parallel between two copper strips (length 16.8 mm, width 4.84 mm, thickness 0.337 mm). A voltage sensor was placed between the gold strips at the location of the cell for the control simulation (5 ns pulse as an input signal) to verify that the correct voltage was being delivered to the exposure system. An edge sensor was placed between the gold strips to measure voltage. A field sensor or initial computational domain was placed around the cell and copper strip electrodes for both the control and single frequency simulations. A point sensor was placed at the location of the cell in order to compute the electric field.

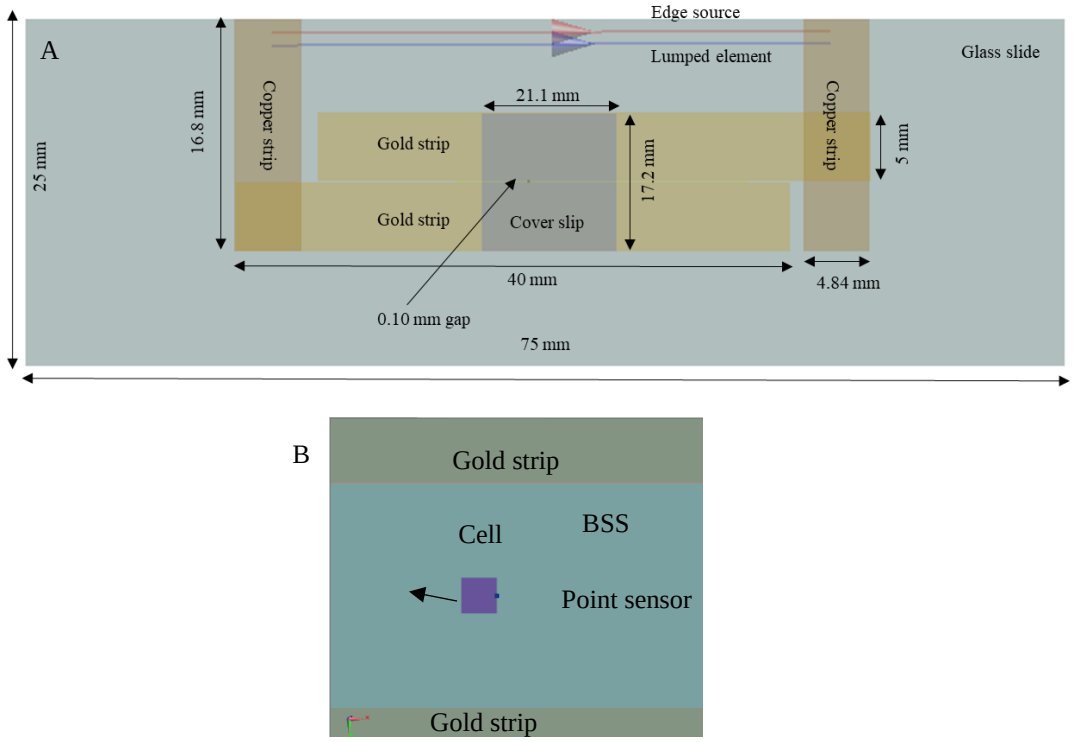

Figure 4.2: Geometry of the gold strip chamber exposure system created in SEMCAD. A) A glass slide forms the bottom of the chamber (large rectangle). Copper strips (the darker gold strips on the each side of the glass slide) are connected to the lighter gold strips that comprise the electrodes (in the center). The two electrodes form a gap of 100 µm between each other, where the longitudinal BSS and the cubic cell are placed. The coverslip is placed on top of the BSS, the region contaning the cell, and covers the electrodes in the center. A 50 Ω lumped element (blue) and edge source (red) are placed between the copper strips. A reference image and diagram are shown in Section 1.7.1. B) An enlarged view of the cell between the electrodes and immersed in BSS. The point sensor is near the cell to compute the electric field at the location of the cell.

4.5 Geometrical model of the tungsten rod exposure system

The geometry of the tungsten rod exposure system created in SEMCAD was based on the exposure system currently in use in our laboratory and is shown in Figure 4.3 (see Chapter 2 for fabrication). An enlarged view of the location of a cell is shown in Figure 4.4

[2]. The tungsten rods had a length of 2.5 mm and a diameter of 127 μm and were separated by100 μm. The tips were positioned 40 μm above the surface of the glass bottom cell dish and placed at a 45° angle to the vertical plane. The dimensions of the dish used in experiments (35 mm circular dish, depth of 7 mm) was reduced and designed as a square (14 mm x 8 mm, depth of 2.93 mm) in order to reduce memory requirements for simulations. As a control to determine if reducing the cell dish size affected the computed results, a control simulation was performed with a cell dish designed in the same manner but with dimensions of 35 mm x 35 mm and depth of 7 mm. Reducing and changing the cell dish size did not affect the computation of the electric field distribution in the region containing the cell because the volume of the cell dish is large and the electric field is generated at the electrode tips, which are confined to a smaller area than the cell dish.

The tungsten rods were immersed in the cell dish containing BSS, with a length of approximately 0.5 mm remaining outside the BSS (the location of the edge source and lumped). The BSS (volume had a length of 11 mm, width of 5 mm, and depth of 1.464 mm) was a rectangle placed inside the cell dish. The part of the electrodes that remained outside the BSS contained the edge source, which acts as the source of the applied electromagnetic signal. A 50 Ω resistor was added at the same location as the edge source. The bottom of the electrodes immersed in BSS had the following sensors between the electrode tips: a) a voltage and b) an edge sensor to measure the voltage of the control simulation. A point sensor was placed at the location of the cell to measure the electric field. The computational domain was large enough to encompass the electrode tips and a cell for each simulation, and large enough to include the parts of the model that will compute the electric field distribution in the region of interest.

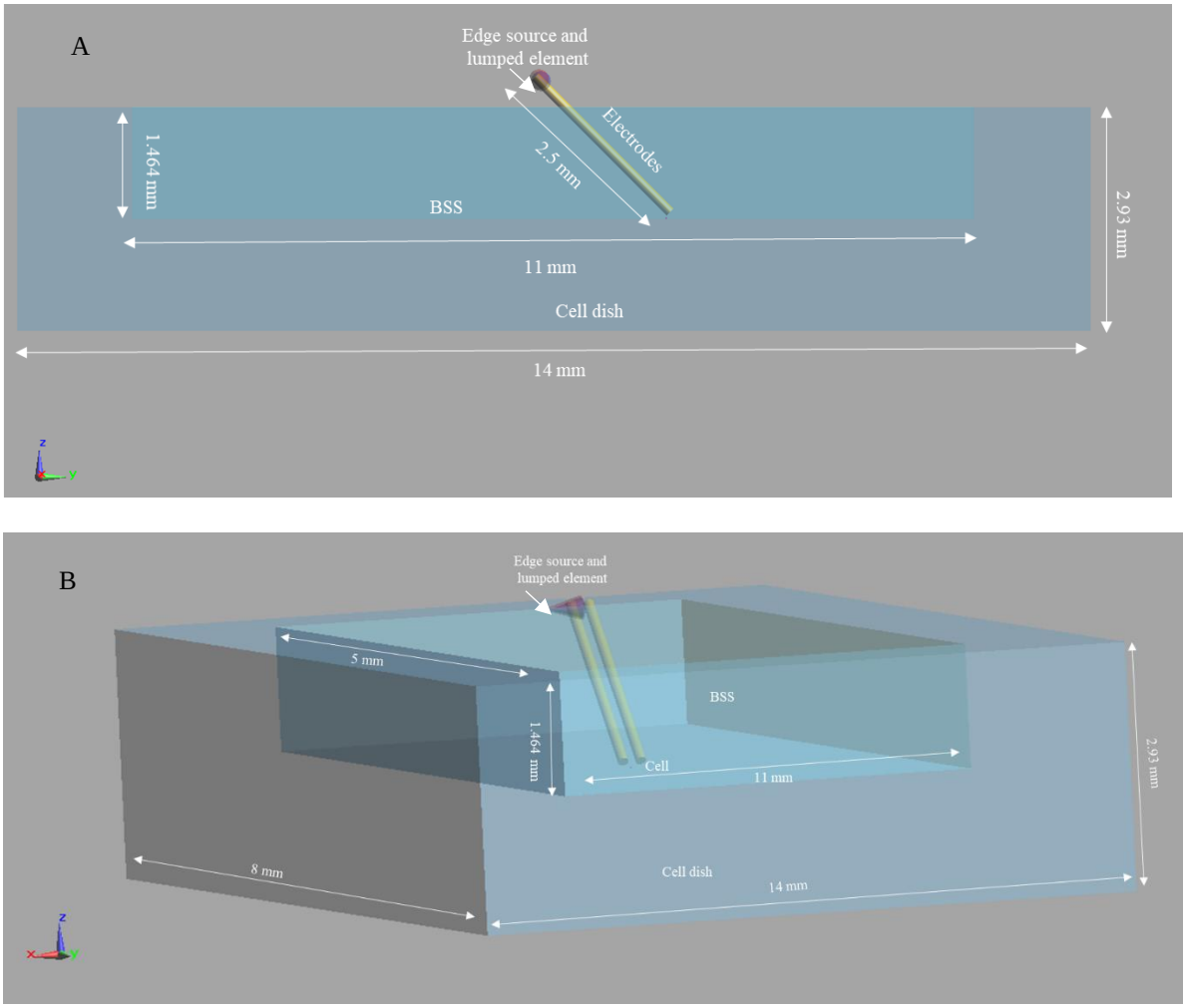

Figure 4.3: Geometry of the tungsten rod exposure system created in SEMCAD. A) Side-view of the tungsten rods immersed in BSS inside the cell dish. The cell dish is the dark blue, larger box area. The BSS is the light blue box area inside the dark blue box. The electrodes are the yellow colored rods in the center. The edge source (red) and lumped element (blue) are at the top of the electrodes. B) A shifted view of the side image. The electrodes are placed 40 μm above the glass dish at a 45º angle. The cell is centrally located between the electrode tips.

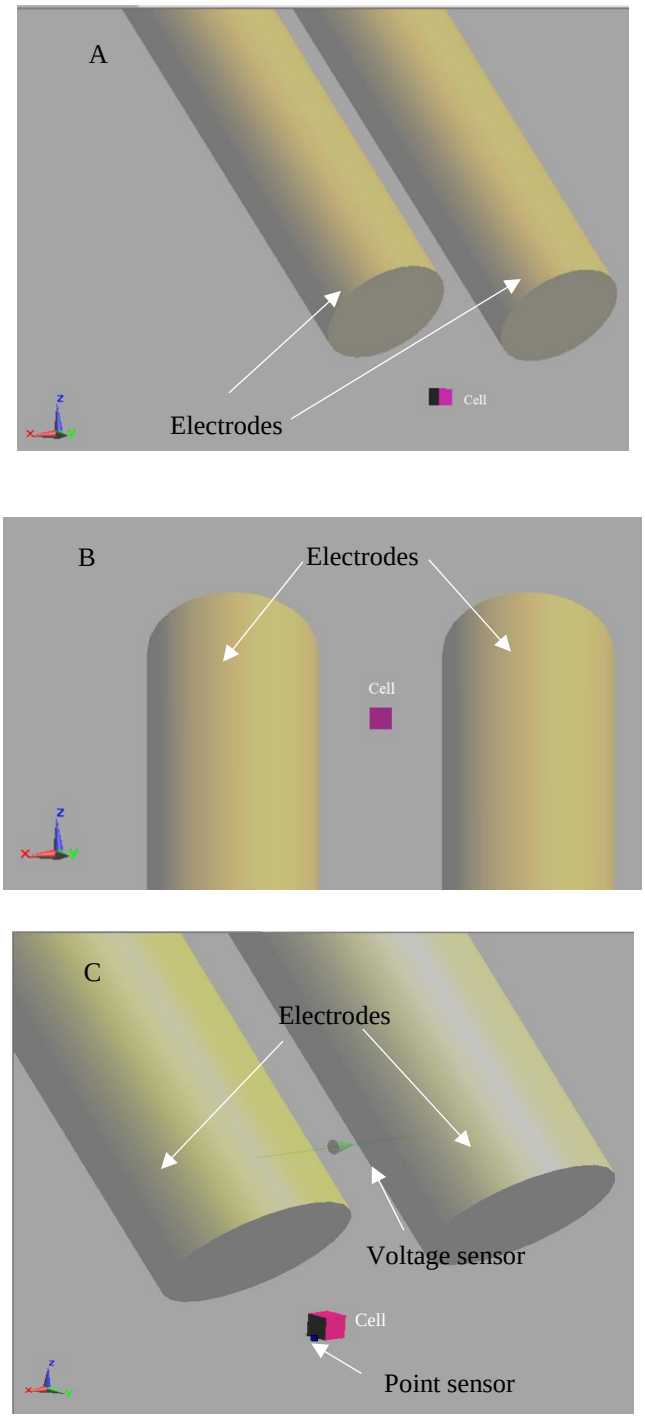

Figure 4.4: Geometry of the tungsten rod exposure system created in SEMCAD showing a view of the electrode tips with respect to the cell. A) View of the electrode tips at a 45ºangle and above the surface of the cell dish. B) View of the cell located centrally between the electrode tips. C) An enlarged view of the cell centrally located between the electrode tips. The point sensor (dark blue square) is located on the bottom of the cell. The voltage sensor is placed between the electrode tips.

After creating the geometric models of the two exposure systems, the Huygens box computational domain was created around the cell to compute the homogeneity of the electric field in the region containing the cell.

4.6 Huygens box simulation

As indicated earlier, the Huygens box in SEMCAD is useful when performing simulations for a refined computation with a significant reduction of the simulation time of the electric field in the vicinity of the cell location [12-17]. Essentially, the Huygens box approach required two computational domains for single frequency simulations, one for the initial computational domain and one for the smaller Huygens box computational domain, requiring a total of two numerical simulations [12-17].

4.7 Grid settings

The grid is important for meshing and discretizing the geometry. For each initial simulation for both exposure systems, the grid mesh was coarse, with the voxels within the volume containing the cell having a step size of 16 μm. The Huygens box had an even finer mesh with a step size of 4 μm for the tungsten rod exposure system and 1 μm for the gold strip chamber exposure system. The discretization for the two exposure systems is shown in Figures 4.5 and 4.6. The computed results for the electric field distribution of the initial

computational domain were used as source input for the Huygens box computational domain.

Table 4 below provides the number of voxels generated for each simulation and discretization of the volume containing the cell in each exposure system.

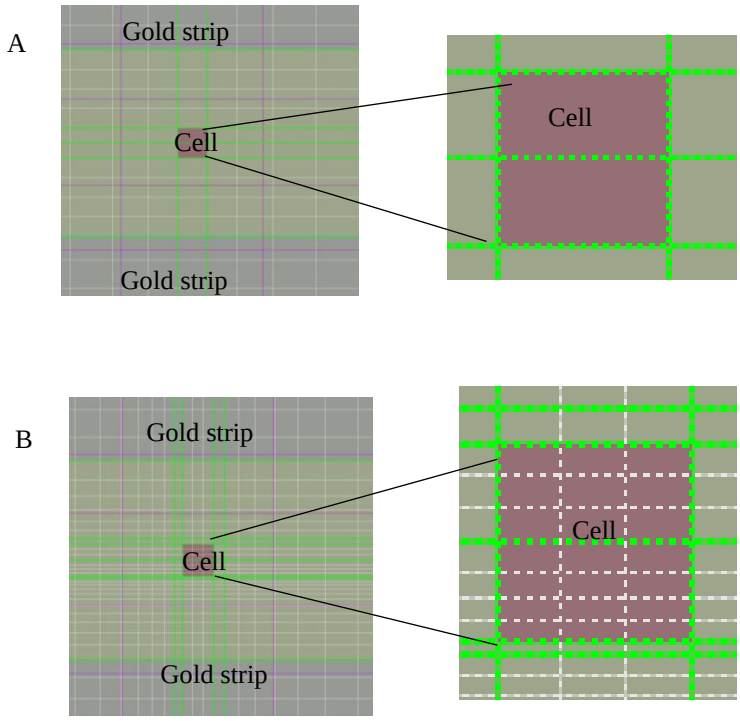

Figure 4.5: Discretization of a cell in the gold strip chamber exposure system for the Huygens box simulations. The cell (magenta) is located centrally between the gold strip chambers (light yellow). Discretization is shown as grid lines that divide the cell into multiple boxes. The green and white lines are part of the grid, where finer discretization is shown by the white lines. The images on the right are zoomed-in-views of the cell. A) Initial computational domain discretization where the cell has a step size of 16 μm. B) Huygens box discretization where the cell has a step size of 1 μm.

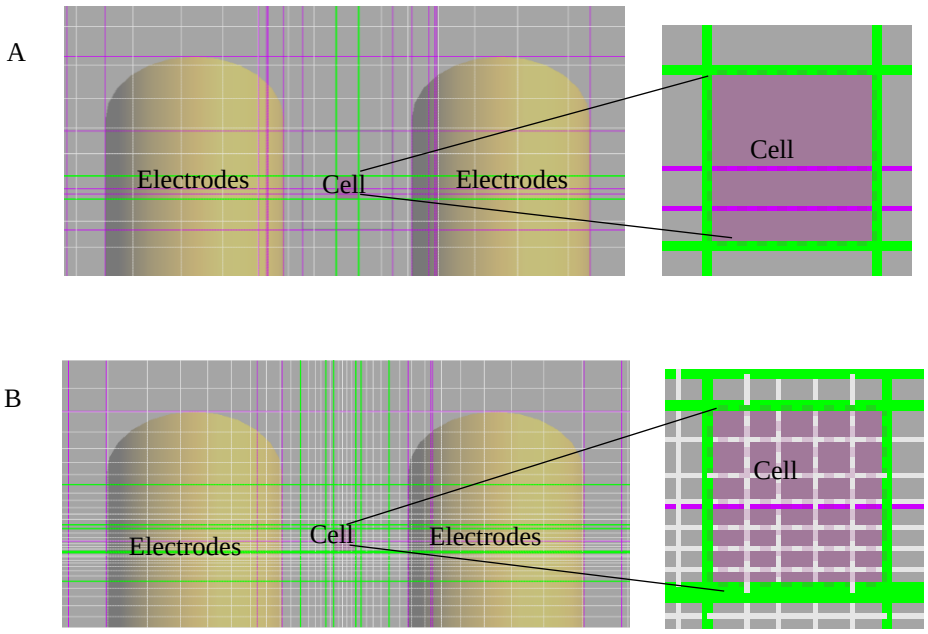

Figure 4.6: Discretization of the cell in the tungsten rod exposure system for the Huygens box simulations. The cell (magenta) is located centrally between the electrode tips (yellow). Discretization is shown as grid lines that divide the cell into multiple boxes. The images on the right show an enlarged view of the cell and the discretization. A) Initial computational domain discretization where the cell has a step size of 16 μm. B) Huygens box discretization where the cell has a step size of 4 μm.

Table 4: Discretization for each simulation for both exposure systems

Exposure system	No. of cells and cell step size in the initial computational domain	No. of cells and cell step size in the Huygens box 2 simulation
Tungsten rod	0.254 Mcells Cell step size of 0.016 mm	0.709 Mcells Cell step size of 0.004 mm
Gold strip chamber	1.242 Mcells Cell step size of 0.016mm	3.784 Mcells Cell step size of 0.004 mm

*Mcells: Megacells or 10^6 cells.

The initial computational domain for the Huygens box simulation was much larger than the Huygens box computational domain, which was located inside the initial computational domain. The Huygens box used electric field results obtained from the initial computational domain as source input. For the tungsten rod exposure system, the initial computational domain had dimensions of 0.070 mm x 0.061 mm x 0.075 mm and a Huygens box computational domain of 0.026 mm x 0.026 mm x 0.022 mm. The gold strip chamber exposure system had an initial computational domain with dimensions of 0.076 mm x 0.076 mm x 0.066 mm, with a Huygens box computational domain of 0.051 mm x 0.051 mm x 0.026 mm. Figure 4.7 shows the initial computational domain (A) and the Huygens box (B). Computed results from the initial computational domain (A) were used as the input source for Huygens box (B).

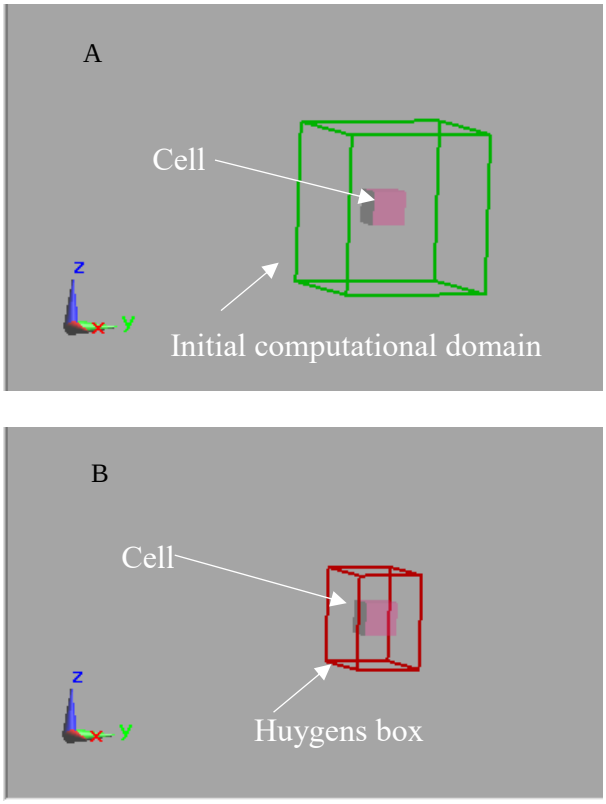

Figure 4.7: Initial computational and the Huygens box computational domain that was used for each simulation. A) The cell is enclosed by the initial computational domain (green). This same computational domain was used to enclose each of the Huygens boxes. B) The Huygens box was located inside the initial computational domain and focused closely on the cell.

After creating the geometric models of the two exposure systems and adding the Huygens box computational domains, running a simulation required a signal input and properties of the various materials/objects in the geometric models. These are described in the next section.

4.8 Signal input for a 5 ns pulse numerical simulation

For the control simulations, the average of 10 traces for a 5 ns pulse was used as the input signal source to compute the electric field distribution (magnitude and direction) for both exposure systems. The purpose was to compute the electric field distribution and ensure the results of these geometries matched those performed earlier by our laboratory. The target was to match results that of 5 MV/m (for the tungsten rod exposure system) and 7 MV/m (for the gold strip chamber exposure system). Since most of the 5 ns pulse experiments were conducted at 5 MV/m, this was the electric field of interest for studying homogeneity in the electric field magnitude in order to determine if the longer-lived calcium responses are due to differences in homogeneity. SEMCAD requires custom signal files (i.e., the pulse trace) to be in text format (.txt file) so that the file reads time (ns) vs. voltage (kV) in two columns. In this manner, the amplitude of the voltage can be scaled if necessary.

4.9 Computer specifications

Simulations were performed on a computer cluster comprised of the SUPER X8DTG-QF motherboard HPC/Cluster with the following hardware specifications:

Windows 7 Enterprise
Processor: Intel (R) Xeon (R) CPU E5506 @ 2.13 GHz (2 processors)
Installed memory: 96 GB
System: 64 bit
Tesla K20C (2X):

CUDA cores: 2496

GK110 GPU

706 MHz frequency

2496 shading units

208 texturing mapping units

40 ROPs

5120 MB GDDR5

Power draw rate of 225 W (maximum)

4.10 Simulation settings common to both exposure systems

The following tables list the properties of the material for each geometrical model and the required settings for a complete simulation (Tables 5 – 14).

Table 5: Basic components used in creating the geometries in SEMCAD of the two exposure systems

Component	Function/Description
Points	Aid in construction and offer a point of reference
Solids	Physical bodies with volume to represent different types of material
Sources	The location where electromagnetic energy is delivered
Lumped elements	Can be resistive, capacitive, or inductive
Sensors	The location where field data are recorded during a simulation
Field Sensor	Boundaries where electromagnetic fields are recorded
Edge Sensor	Records voltage, current, power, or impedance.
Voltage Sensor	Records voltage

Table 6: Dielectric properties for each material used in the exposure system models

Material	Electrical Conductivity (S/m)	Relative Permittivity (F/m)	Reference
Glass (slide, coverslip, cell dish)	1.0×10^{-12}	4.3	[18]
Chromaffin Cell	1.425	72.3	[19, 20]
BSS	1.425	72.3	[19, 20]
Tungsten	1.79×10^{7}	1	[SEMCAD]
Gold	4.098×10^{7}	1	[SEMCAD]
Copper	5.813×10^{7}	1	[SEMCAD]

Table 7: Settings for the background

Type:	**Dielectric**
Density:	1.0×10^{-12} kg/m^3

Table 8: Settings for the chromaffin cell and BSS for both exposure systems

Type:	Dielectric
Region characteristics:	Volume
Frequency:	5.0×10^{2} MHz
Relative Permittivity:	72.3
Relative Permeability:	1
Electrical Conductivity:	1.425 S/m
Number of magnetic poles:	No dispersive poles
Electric Field Saturation:	1

Table 9: Settings for the glass components for both exposure systems

Type:	Dielectric
Region Characteristics:	Volume
Relative Permittivity:	4.3
Relative Permeability:	1
Electrical Conductivity:	1.0×10^{-12} S/m

Table 10: Settings for the control 5 ns pulse simulation

Excitation:	Broadband
Frequency:	Center frequency of operation; selected to be 50 MHz because it is half of the frequency bandwidth of the FFT of the pulse.
Bandwidth:	Essentially, one would need enough bandwidth for the simulation to run. This can be any value, but since the FFT of the pulse yielded a frequency range up to 100 MHz, 100 MHz to 1 GHz was selected to be the bandwidth. This would allow one to view the simulation calculations over the entire bandwidth that covers the entire pulse range.
Wavelength/Wavelength Bandwidth:	The software, depending on the input value of the frequency and bandwidth, calculates these automatically.
User defined signal:	Pulse of interest in .txt file.
Simulation time (s):	Select the length of the time based on the time period from the pulse signal file, it should be long enough to cover the entire pulse signal.
Simulation time unit:	Select seconds.
Automatic termination:	Must be selected in order for the software to terminate the solver once it reaches steady state.
Global Auto Stop Threshold:	Medium was selected. This is important for the solver to converge to a solution once it reaches steady state, medium is the suggested setting.
Monitoring of Edge:	Select this
Solver:	FDTD
FDTD High performance:	aXware
aXware preferences:	Favor fastest simulation
Time step factor:	1
Max iSolve Threads:	Automatic

4.11 Tungsten rod electrode properties

Table 11: Settings for tungsten in the tungsten rod electrode exposure system

Type:	Perfect Electric Conductor (PEC)/Metal
Region characteristics:	Volume
Remove Perfect Electric Conductor (PEC)/Perfect Magnetic Conductor (PMC) :	Select this
Lossy Metal	Select this
Relative permittivity:	1
Relative Permeability:	1
Electrical Conductivity:	1.79×10^7 S/m

4.12 Gold strip electrode properties

Table 12: Settings for the gold strips in the gold strip exposure chamber

Type:	PEC/Metal
Region Characteristics:	Volume
Remove PEC/PMC Spikes:	Select this
Lossy Metal SIBC:	Select this
Frequency:	1.0×10^3 MHz (Frequency is specific for gold)
Relative Permeability:	1
Relative Permittivity:	1
Electrical Conductivity:	4.098×10^7 S/m

4.13 Copper strip properties

Table 13: Copper strip settings used in gold strip exposure system

Type:	PEC/Metal
Region characteristics:	Volume
Remove PEC/PMC spikes:	Select this
Lossy Metal SIBC:	Select this
Frequency:	1.0×10^3 MHz
Relative Permittivity:	1
Relative Permeability:	1
Electrical Conductivity:	5.813×10^7 S/m

Table 14: Settings specific to the Huygens box simulations for both exposure systems

Excitation:	Harmonic
Frequency:	Insert the single frequency at which you wish to run the simulation
On	Select this
Source of Incident Field:	Enclosing Field Sensor
Simulation for Excitation Field:	Previous Simulation
Sensor for Excitation Field:	Field Sensor from previous simulation
Amplitude:	Need to modify the amplitude as needed

4.14 Extracting Results

After the completion of a numerical simulation, the computed electric field results could be extracted in the software in two ways: as contour plots in the X, Y, and Z plane or as line plots in the X, Y, and Z plane. The contour plots provided the magnitude and direction of the computed electric field distribution, within the computational domain. The line plots provided a graphical representation of the magnitude of the computed electric field distribution within the computational domain. 3D mesh graphs of the electric field magnitude along the Z axis were plotted for the tungsten rod exposure system using Sigmaplot (Version 14, Systat Software, Inc.).

References

[1] Kuster, N. and Schonborn, F. (2000). Recommended minimal requirements and development guidelines for exposure setups of bio-experiments addressing the health risk concern of wireless communications. *Bioelectromagnetics*, 21(7), pp.508-514.

[2] Zaklit, J., Craviso, G., Leblanc, N., Yang, L., Vernier, P. and Chatterjee, I. (2017). Adrenal Chromaffin Cells Exposed to 5-ns Pulses Require Higher Electric Fields to Porate Intracellular Membranes than the Plasma Membrane: An Experimental and Modeling Study. *The Journal of Membrane Biology*, 250(5), pp.535-552.

[3] G. Craviso, P. Chatterjee, G. Maalouf, A. Cerjanic, J. Yoon, I. Chatterjee, and P. Vernier, "Nanosecond electric pulse-induced increase in intracellular calcium in adrenal chromaffin cells triggers calcium-dependent catecholamine release," *IEEE Transactions on Dielectrics and Electrical Insulation*, vol. 16, no. 5, pp. 1294–1301, 2009.

[4] Ammar-hakim.org. (2018). *JE7: The dual Yee-cell FDTD scheme — SimJournal*. [online] Available at: http://ammar-hakim.org/sj/je/je7/je7-dual-yee.html [Accessed 28 Sep. 2018].

[5] Fan, W., Chen, Z. and Yang, S. (2016). On the Analytical Solution of the FDTD Method. *IEEE Transactions on Microwave Theory and Techniques*, 64(11), pp.3370-3379.

[6] Kane Yee (1966). Numerical solution of initial boundary value problems involving Maxwell's equations in isotropic media. *IEEE Transactions on Antennas and Propagation*, 14(3), pp.302-307.

[7] Taflove, A. (1988). Review of the formulation and applications of the finite-difference time-domain method for numerical modeling of electromagnetic wave interactions with arbitrary structures. *Wave Motion*, 10(6), pp.547-582.

[8] Yu, C. (2016). Application of Parseval's Theorem on Evaluation Some Definite Integrals. *Turkish Journal of Analysis and Number Theory*, 2(1), pp.1-5.

[9] Craviso, G., Choe, S., Chatterjee, I. and Vernier, P. (2012). Modulation of intracellular Ca^{2+} levels in chromaffin cells by nanoelectropulses. *Bioelectrochemistry*, 87, pp.244-252.

[10] Sun, Y., Vernier, P., Behrend, M., Marcu, L. and Gundersen, M. (2005). Electrode Microchamber for Noninvasive Perturbation of Mammalian Cells With Nanosecond Pulsed Electric Fields. *IEEE Transactions on Nanobioscience*, 4(4), pp.277-283.

[11] P. Vernier, Y. Sun, L. Marcu, S. Salemi, C. M. Craft, and M. A. Gundersen, "Calcium bursts induced by nanosecond electric pulses," *Biochemical and Biophysical Research Communications*, vol. 310, no. 2, pp. 286–295, 2003.

[12] Benkler, S., Chavannes, N., and Kuster, N. "Novel FDTD Huygens source enables highly complex simulation scenarios on ordinary PCs," *2009 IEEE Antennas and Propagation Society International Symposium*, 2009.

[13] Christ, A., Douglas, M., Roman, J., Cooper, E., Sample, A., Waters, B., Smith, J. and Kuster, N. (2012). Evaluation of Wireless Resonant Power Transfer Systems With Human Electromagnetic Exposure Limits. *IEEE Transactions on Electromagnetic Compatibility*, pp.1-10.

[14] Hong, S., Cho, I., Kwon, J. and Pack, J. (2015). Assessment of human exposure to electromagnetic fields from wireless power transfer system in the 1.8 MHz. *Microwave and Optical Technology Letters*, 57(5), pp.1125-1129.

[15] Liu, W., Wang, H., Zhang, P., Li, C., Sun, J., Chen, Z., Xing, S., Liang, P. and Wu, T. (2019). Statistical Evaluation of Radiofrequency Exposure during Magnetic Resonant

Imaging: Application of Whole-Body Individual Human Model and Body Motion in the Coil. International Journal of Environmental Research and Public Health, 16(6), p.1069.

[16] Thiel, M. (2010). Electromagnetic Models for Indoor Wave Propagation Analysis and their Application for Ultra-wideband Near-field Radar Imaging of Building Interiors and Human Movement Detection. Ph.D. University of Michigan.

[17] Vermeeren, G., Gosselin, M., Kühn, S., Kellerman, V., Hadjem, A., Gati, A., Joseph, W., Wiart, J., Meyer, F., Kuster, N. and Martens, L. (2010). The influence of the reflective environment on the absorption of a human male exposed to representative base station antennas from 300 MHz to 5 GHz. *Physics in Medicine and Biology*, 55(18), pp.5541-5555.

[18] "Relative Permittivity - the Dielectric Constant," Engineering ToolBox. [Online]. Available:https://www.engineeringtoolbox.com/relative-permittivity-d_1660.html. [Accessed: 12-Jun-2019].

[19] Retelj, L., Pucihar, G. and Miklavcic, D. (2013). Electroporation of Intracellular Liposomes Using Nanosecond Electric Pulses—A Theoretical Study. *IEEE Transactions on Biomedical Engineering*, 60(9), pp.2624-2635.

[20] Sabuncu, A., Stacey, M., Craviso, G., Semenova, N., Vernier, P., Leblanc, N., Chatterjee, I. and Zaklit, J. (2018). Dielectric properties of isolated adrenal chromaffin cells determined by microfluidic impedance spectroscopy. *Bioelectrochemistry*, 119, pp.84-91.

Chapter 5: Numerical modeling results for both exposure systems

5.1 Introduction

Exposure systems for applying electric fields to biological cells *in vitro* must be well characterized in terms of homogeneity of the electric field magnitude to reproduce experimental results and to understand if variations in biological responses are due to differences in homogeneity of the electric field, or due to some other reason [1]. As mentioned earlier, our laboratory used two different exposure systems to deliver 5 ns pulses to chromaffin cells for studying the effect of these pulses on changes in intracellular calcium [2-4]. Chromaffin cells exposed to a 5 ns pulse using the gold strip chamber exposure system underwent increases in intracellular calcium that returned to pre-stimulus levels with an average half-width of ~8.6 s [4] and in experiments conducted more recently, with an average half-width of ~11.1 s (experiments performed by Dr. Josette Zaklit, University of Nevada, Reno).

Currently, we are exposing cells to 5 ns, 5 MV/m pulses using a tungsten rod exposure system, which evoked variable calcium responses in which calcium either returned to pre-stimulus calcium levels with an average half-width of 23 s or remained prolonged compared to cells exposed by the gold strip exposure system (Figure 3.2). Figure 5.1 compares the average time course of the calcium responses evoked by both exposure systems. This difference in the time course presented an anomaly regarding how the

calcium responses of the same type of cell exposed to a single 5 ns pulse can vary tremendously when two different exposure systems are used. The characteristics of the calcium responses evoked by 5 ns pulses applied using the two exposure systems are summarized in Table 15.

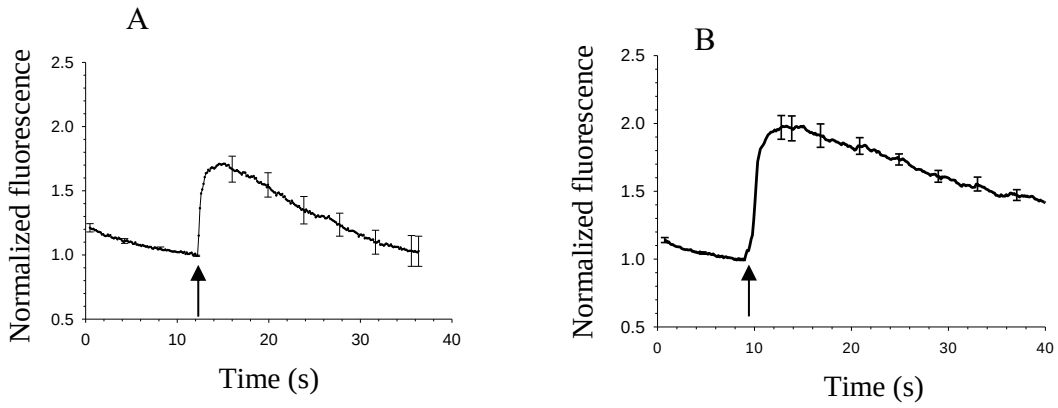

Figure 5.1 Comparison of calcium responses evoked by each exposure system. Average response of cells exposed to a single 5 ns pulse (4-5 MV/m) using A) the gold strip chamber exposure system (N=24) and B) the tungsten rod exposure system (N=11). Responses in (A) obtained from Dr. Josette Zaklit (University of Nevada, Reno). Arrow indicates when the 5 ns pulse was applied.

Table 15: Characteristics of calcium responses generated by the gold strip chambers and tungsten rod exposure systems.

Stimulus	**T_{50} (s)**	**Amplitude ± SE (F/F_0)**	**Half-width ± SE (s)**	**Recovery ± SE ($(F/F_0)/s$)**
Gold strip chambers (4.44 - 5.89 MV/m)	1.6 ± 0.1	1.6 ± 0.2	11.1 ±1.6	0.035 ±0.00 (N= 24)
Tungsten rods (Single 4.95 - 5 MV/m)	2.2 ± 0.3	2.1 ±0.3	23.0 ± 2.6	0.02 ±0.00 (N=11)

The calcium responses evoked by the tungsten rod exposure system had a slightly longer T_{50} to reach maximum calcium amplitude, a larger amplitude, a larger half-width, and a much slower rate of recovery to pre-stimulus calcium levels compared to cells exposed in the gold strip chamber exposure system. Hence, it was pertinent to investigate if the variations in the calcium responses were due to differences in the homogeneity of the electric field magnitude and propagation of the direction in the region containing the cell. It was also important to investigate the effect of slight differences in the placement of the tungsten rod electrode tips above glass bottom dish as well as the effect of slightly misaligned electrode tips on the electric field magnitude.

In this Chapter, the computed results of the electric field magnitude are presented as contour plots along the Y axis and Z axis, vector plots, surface plots, and line plots for

the Huygens box simulations. Figure 5.2 shows diagrams of the X, Y, and Z axis and at which axis the contour slice was extracted.

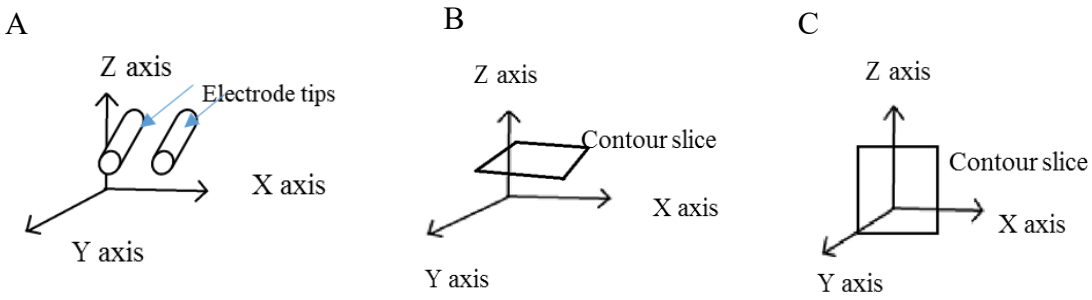

Figure 5.2: Diagram of the axes showing the planes at which contour plots were extracted in SEMCAD. The exposure system geometries are aligned according to the axes shown in (A). The Z axis contour slice is extracted as shown in (B), providing a contour slice in the XY plane. A Y axis contour slice is extracted as shown in (C), providing a contour slice in the YZ plane.

Surface plots of the electric field distribution were generated by plotting individual points of the contour plots along the Z axis in a graphing software program, Sigmaplot, which showed more detail in miniscule differences in the electric field magnitude as compared to the respective contour plots from each simulation in SEMCAD. However, surface plots were graphed in Sigmaplot for the tungsten rod exposure system only. Due to the depth of the glass slide, the small volume in which the cell is located, and meshing of the gold strip chamber exposure system, the exported contour slices did not graph well in Sigmaplot.

5.2 Area of homogeneity of the electric field distribution in the region containing the cell

Homogeneity in the electric field magnitude was calculated by taking the computed electric field magnitude values from each contour slice in the X, Y, and Z directions over multiple slices to provide a volume computation for each simulation. Each slice was the computed electric field magnitude within the grid. For example, in a coarse mesh, the cell was designated by a grid step size of 16 μm or a dimension of 16 μm x 16 μm x 16 μm. The electric field magnitude was computed for a total distance of 16 μm from one end of the contour slice to the other end in the X, Y, and Z directions. The homogeneity of this cell was computed in a larger area around the cell. Figure 5.3 shows a diagram of the region from which the homogeneity in the electric field magnitude was calculated in dimensions of 50 μm x 50 μm x 50 μm, with the cell centrally located.

For the Huygens box simulations, homogeneity in the electric field distribution was calculated in the region containing the cell in a volume of 20 μm x 20 μm x 20 μm, providing the homogeneity in an enlarged view in the region of interest containing the cell. The electric field distribution is plotted as line plots that show the change in the electric field along a distance of 20 μm in the X, Y, and Z directions. Homogeneity was computed by calculating the percent difference in the line plots. In the following section, line plots, surface plots, and contour plots of the electric field magnitude (and direction for control simulations and Huygens box simulations) show the computed electric field magnitude distribution.

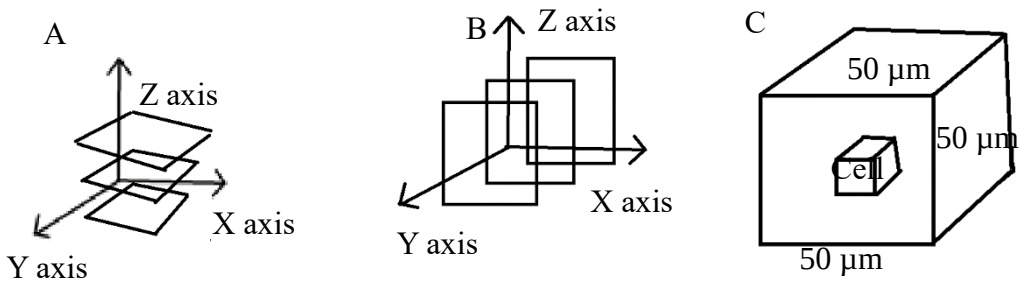

Figure 5.3: Homogeneity in the electric field magnitude was calculated by volume with the cell centered in the region. The diagram in (A) shows how each contour slice of the electric field magnitude was analyzed by slice along the Z axis and used to calculate the electric field homogeneity over a distance of 50 µm, comprising multiple contour slices. The diagram in (B) shows how homogeneity was calculated by slice over a distance of 50 µm along the Y axis. This same method was also used to calculate homogeneity along the X axis. The diagram in (C) shows the total volume if the contour slices were connected to form a 50 µm x 50 µm x 50 µm region, with the cell resting on the glass bottom dish.

5.3 Tungsten rod exposure system: control simulations

A test case control simulation with the tungsten rod exposure system was conducted by comparing the computed electric field magnitude with simulations performed by previous lab members [5]. The goal was to obtain a computed electric field magnitude of 5 MV/m at the location of the cell. The next section discusses this control simulation.

5.3.1 Tungsten rod exposure system: control simulation with cell dish dimensions in the model matching the dimensions of the cell dish used in experiments

Since the dimensions of the cell dish were reduced in order to decrease computer memory requirements and simulation time for the computations of electric field distributions (described in Chapter 4), a simulation was conducted with the cell dish having

the exact dimensions of the cell dish (length and width of 35 mm and height of 7 mm) used in experiments. This simulation was completed with a coarse mesh in which the cell was represented by a cube with a step size of 16 μm having the electrical properties of BSS. Figure 5.4, A shows a contour plot of the distribution of the computed electric field magnitude, taken at the time which the applied pulse was at its maximum magnitude of 1000 V normal to the Z axis. The electrodes are the cylindrical structures (dotted line) with the cell centered between them. The Z axis provides an image of the electrodes as if one were looking downward towards the end of the tips. The cell is represented as a cube centered between the electrodes and is exposed to an electric field of 5 MV/m. The homogeneity was computed in a volume of dimensions 50 μm x 50 μm x 50 μm with the cell centered in this region. The electric field magnitude was constant in the plane normal to the Z axis over a distance of 50 μm, within 6% over a distance of 50 μm in the Y direction, and 3% over a distance of 50 μm in the X direction. Figure 5.4, B is a contour plot of the electric field distribution along the Y plane, showing that the cell, represented as a single voxel, is exposed to an electric field of 5 MV/m. The dark regions in the contour plot are the tips of the electrodes along the Y direction. As expected, since the electrodes are represented by a perfect electric conductor (PEC), the electric field within the electrodes is zero as seen in Figure 5.4, B. Figure 5.5 shows a vector plot of the electric field direction indicating that the cell is exposed to the electric field in the X direction. Figure 5.6 shows a surface plot of the electric field magnitude in the XY plane, showing that the electric field magnitude remains at 5 MV/m over a distance of 50 μm in both the X and Y directions. The next section discusses the results with the reduced cell dish size, which was used for all of the simulations.

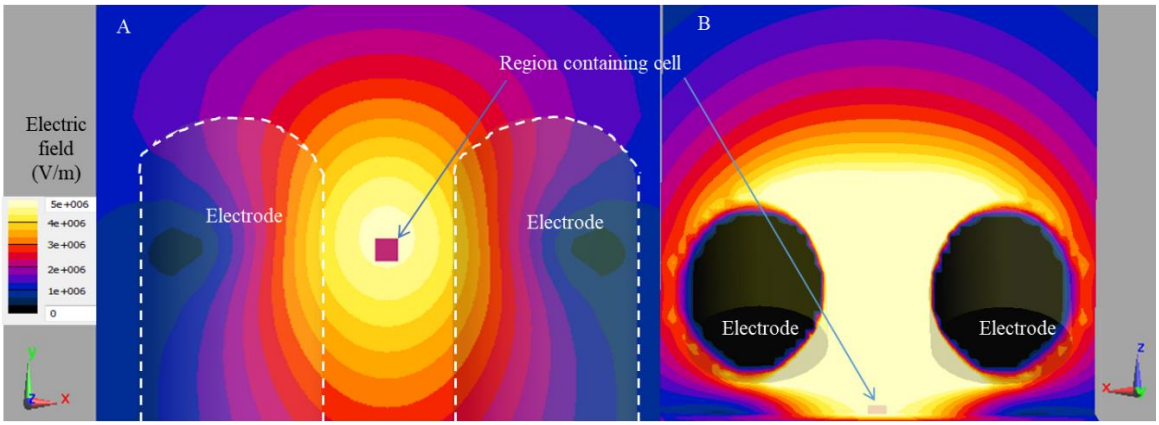

Figure 5.4: Computed electric field magnitude distribution for the tungsten rod exposure system with the cell dish dimensions matching the actual dish size used in experiments. Contour slice images of the magnitude of the computed electric field distribution in a plane normal to the Z axis (A) and Y axis (B), respectively, at the point at which the pulse was at its maximum voltage. The cell (cube) is centered between the electrode tips and receives an electric field magnitude of 5 MV/m. The homogeneity was computed in a volume of dimensions 50 μm x 50 μm x 50 μm with the cell centered in this region.

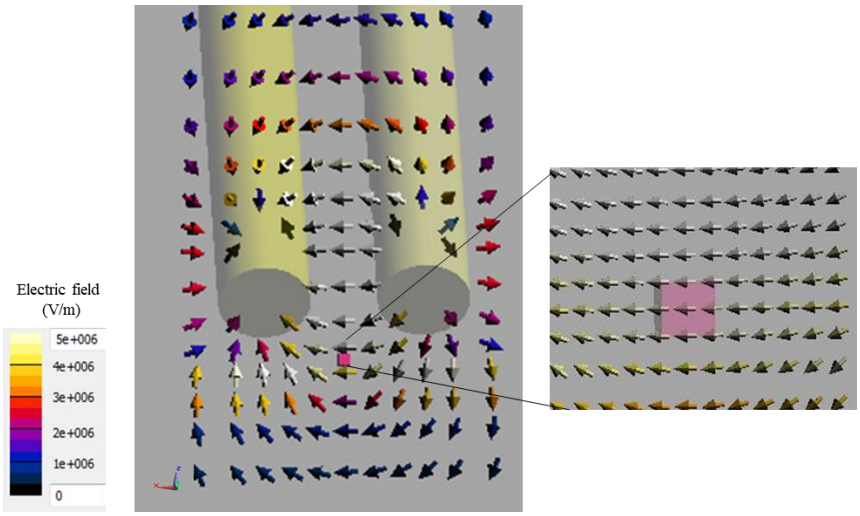

Figure 5.5: Vector plot showing the direction of the electric field distribution in the Y plane. The direction of the electric field at the location of the cell is only in the X-direction.

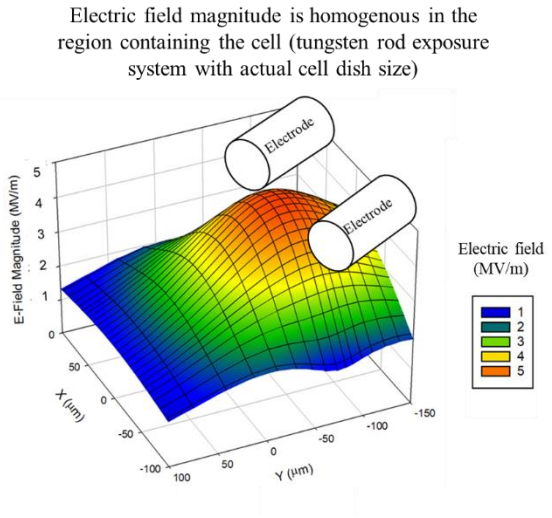

Figure 5.6: Surface plot of the computed electric field magnitude in a plane normal to the Z axis for the tungsten rod exposure system. The cell dish dimensions matched the actual size used in experiments.

5.3.2 Tungsten rod exposure system: control simulation with reduced cell dish dimensions

To compare the electric field distribution in the region containing the cell, using the actual dimensions of the cell dish used in experiments to the electric field distribution obtained in the same region using the smaller dimension cell dish, the computation was performed with the cell having a step size of 16 µm. Figures 5.7, A and 5.7, B show the computed electric field distributions taken at the time point at which the highest voltage in the pulse was applied to the tungsten rod exposure system in planes normal to the Z and Y axes respectively. Figure 5.8 shows a vector plot of the electric field direction applied to the cell by the tungsten rod exposure system. The vector plot shows that the cell is exposed to the electric field in the X direction (E_x direction). However, there is noticeable change in the electric field from the X-direction around the electrode tips. Since the cell is placed

centrally between the electrode tips it is concluded from Figures 5.7, A and 5.7, B, that the cell is not exposed to a change in direction of the electric field. Figure 5.9 shows a surface plot of the electric field in the region containing the cell, demonstrating that the electric field remains constant at a value of 5 MV/m over a distance of 50 µm in the X and Y directions. According to these computations, the cell is exposed to an electric field magnitude of 5 MV/m that was constant in the Z direction over a distance of 50 µm, to within 1.9 % over a 50 µm distance in the X direction, and to within 22.9% over a distance of 50 µm in the Y direction, with the cell placed centrally in the 50 µm x 50 µm x 50 µm region. Within a 20 µm x 20 µm x 20 µm, region, the electric field magnitude remained constant at 5 MV/m in the X, Y, and Z directions. However, since we used a reduced cell dish size for the remaining simulations, we compared the differences between simulations with the reduced cell dish size and actual dish size, as discussed in the next section.

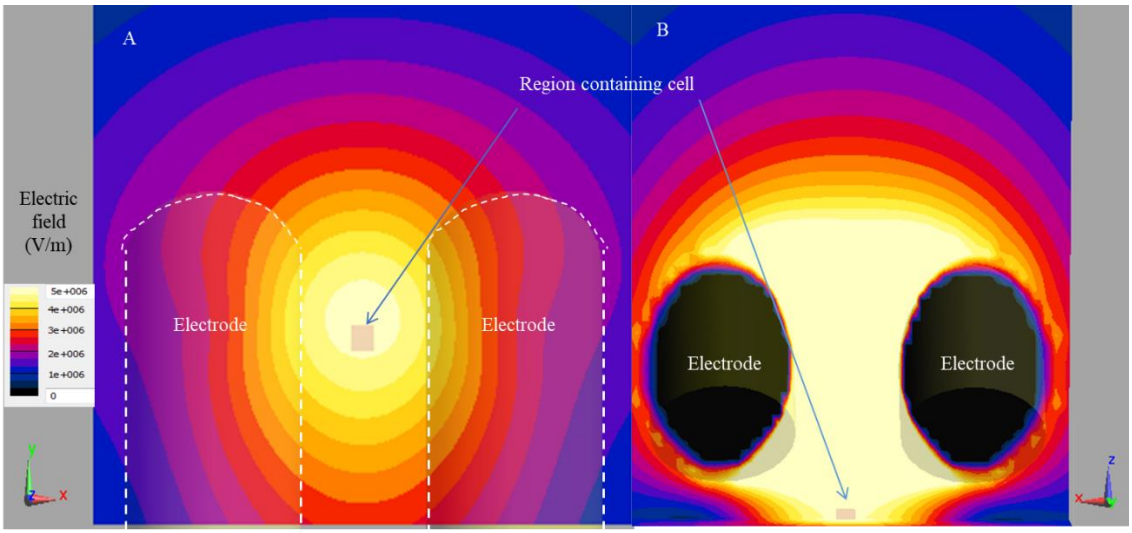

Figure 5.7: Computed distribution of the electric field magnitude for the tungsten rod exposure system with reduced cell dish dimensions. In (A), plane is normal to the Z axis and in (B), normal to the Y axis. The electric field magnitude was 5 MV/m in the X, Y, and Z directions in both (A) and (B).

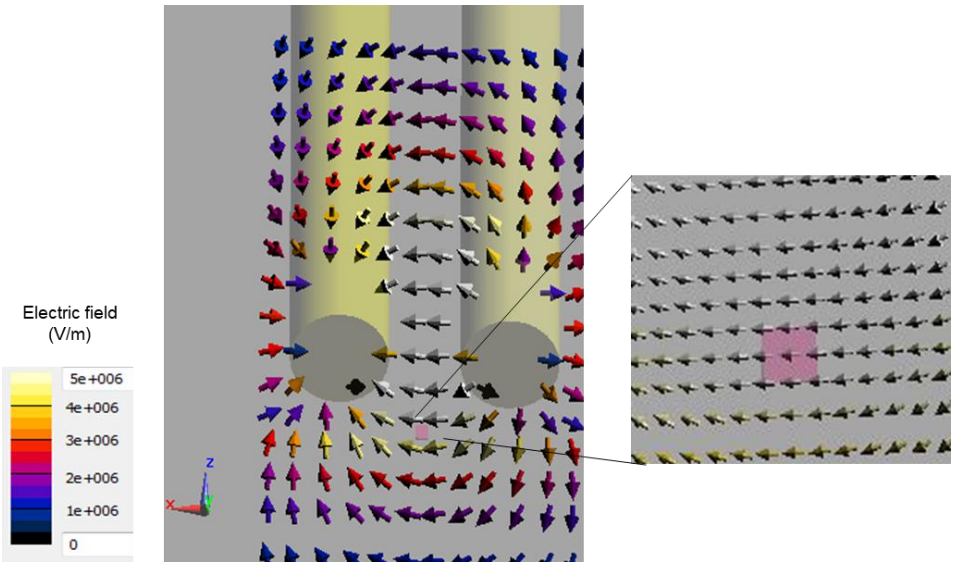

Figure 5.8: Vector plot showing the direction of the electric field distribution in the Y plane with reduced cell dish dimensions. The direction of the electric field at the location of the cell is only in the X direction.

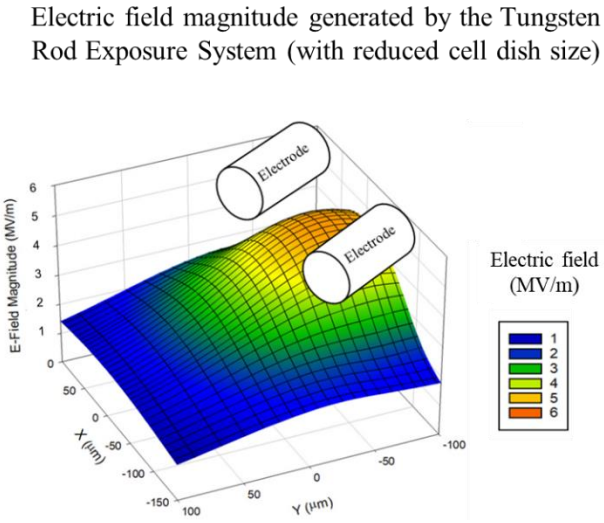

Figure 5.9: Surface plot of the computed electric field magnitude in a plane normal to the Z axis for the tungsten rod exposure system. The cell dish dimensions were reduced relative to the actual cell dish size used in experiments.

5.3.3 Comparison of the computed electric field magnitude and direction for the tungsten rod exposure system with the actual cell dish and reduced dimension cell dish

After completing simulations of the tungsten rod exposure system with the actual cell dish size and reduced cell dish size, it was important to compare the electric field distribution in the region containing the cell for both these cases. Both simulations were conducted with a coarse mesh size with the cell having a step size of 16 μm with dimensions of 16 μm x 16 μm x 16 μm. Figure 5.10 shows the contour plots of the electric field magnitude distribution in the XY plane for both simulations (actual cell dish size vs. the reduced cell dish size). There is relatively no significant difference in the electric field magnitude in the X, Y, and Z directions over a distance of 20 μm when the two cases are compared. However, there is an 8 % difference in the X direction and 6 % difference in the Y direction over a distance of 50 μm. Overall, the region containing the cell is exposed to the same electric field magnitude of 5 MV/m (Figures 5.10 and 5.11) and in the E_x direction only (Figures 5.5 and 5.8) in both simulations. Thus, there is no significant difference in the electric field magnitude and direction when the two cases are compared, validating the use of the reduced cell dish size for the following simulations.

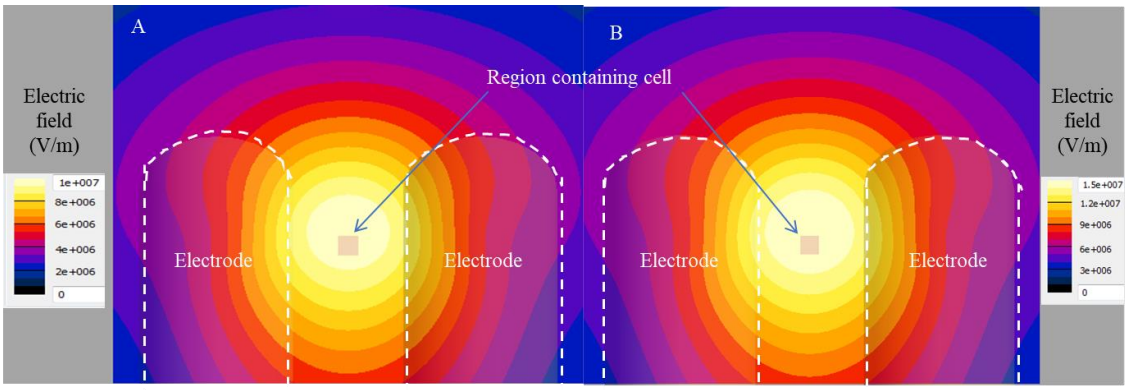

Figure 5.10: Comparison of the computed distribution of the electric field in the tungsten rod simulations using different cell dish sizes. Both (A, cell dish matching actual dimensions used in experiments) and (B, reduced cell dish size) show contour plots of the electric field magnitude in the XY plane with the cell centered between the electrodes is exposed to a constant electric field of 5 MV/m over a distance of 20 µm in the X, Y, and Z directions in both simulations.

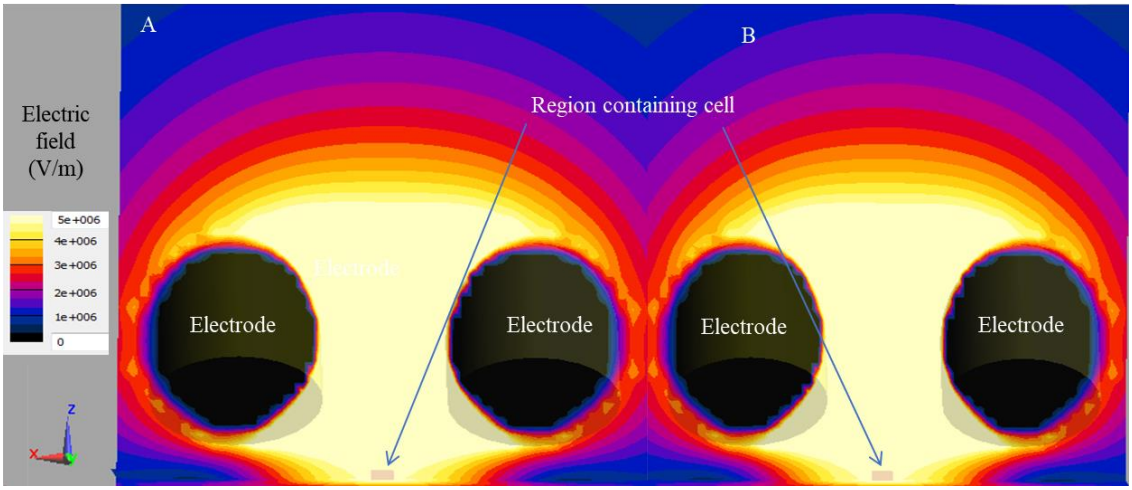

Figure 5.11: The computed electric field magnitude is 5 MV/m in the tungsten rod simulations using different cell dish sizes. Both (A, cell dish matching actual dimensions used in experiments) and (B, reduced cell dish size) contour slices normal to the Y axis of both simulations show no significant difference in the electric field magnitude in the region containing the cell.

5.4 Validation of the conversion factor for obtaining the desired electric field magnitude for experiments

The benefit of performing simulations with SEMCAD is obtaining the computed electric field magnitude relative to the voltage applied to the electrodes. As shown earlier, an applied voltage of 1000 V generates an electric field magnitude of 4.95 MV/m, which is rounded to 5 MV/m. The conversion factor is calculated by dividing the computed electric field magnitude by the applied voltage (see Chapter 4). For example, in this case, 4.95 MV/m divided by 1000 V and yields a conversion factor of 0.00495 MV/m. This applied voltage for an experiment is multiplied by this conversion factor in order to obtain the electric field. Thus, multiplying 0.00495 MV/m by 2000 V yields an electric field magnitude of 9.9 MV/m and multiplying 0.00495 MV/m by 3000 V yields an electric field magnitude of 14.85 MV/m. Figures 5.12, A and 5.12, B show contour plots of the electric field magnitude along the Z axis by applying 2000 V and 3000 V to the electrodes, which correlate with calculating the electric field magnitude by multiplying the conversion factor with the applied voltage.

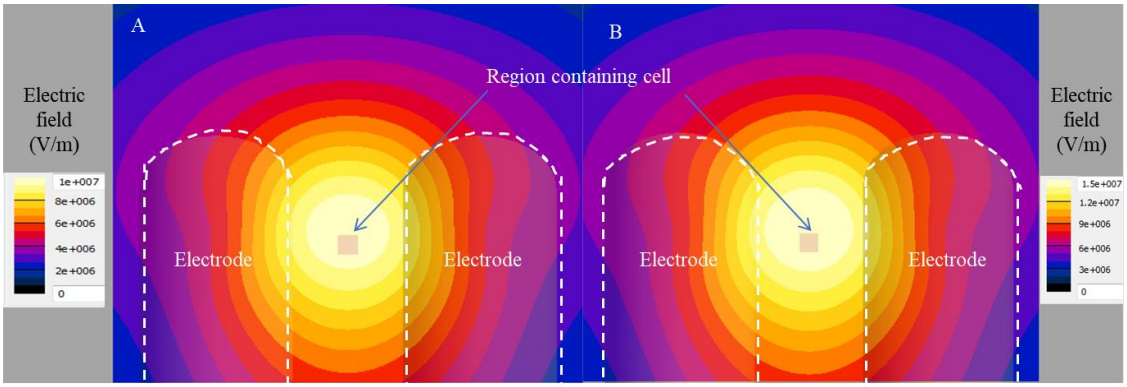

Figure 5.12: Electric field magnitudes of 10 MV/m and 15 MV/m correlate with the conversion factor. A) Applying 2000 V resulted in an electric field magnitude of 10 MV/m in the region containing the cell, validating the linear relation between the conversion factor and applied voltage. B) Applying 3000 V resulted in an electric field magnitude of 10 MV/m in the region containing the cell, also validating the conversion factor and applied voltage relationship.

5.5 Tungsten rod exposure system: Electrode tips placed at different heights from the surface of the glass bottom dish

5.5.1 Computed electric field magnitude and direction at the location of a cell when electrode tips are placed 35 µm and 45 µm above the surface of the glass bottom dish

As described earlier, a cell is exposed to an electric field magnitude of 5 MV/m when the tungsten rod electrode tips are positioned 40 µm above the surface of the cell dish. However, for each cell that is exposed to a pulse in experiments, placement of the electrode tips could possibly be off by ± a few micrometers. We therefore computed the electric field distribution and direction at the location of a cell when the electrode tips were positioned at 40 ± 5 µm from the surface of the glass dish. For these determinations, a cell

was represented by a single cubical voxel of dimension 16 µm. Figure 5.13 shows the computed electric field distributions in the form of contour plots normal to the Z axis with electrodes placed at a height of 35 µm above the dish surface. Under these conditions, the electric field at the location of the cell was increased to 5.5 MV/m, with the electric field remaining constant at 5.5 MV/m over a distance of 50 µm in the X, Y, and Z directions. That is, the electric field magnitude was homogeneous in the Z direction over a 50 µm distance, homogeneous to within 7.7% in the X direction over a 50 µm distance, and homogeneous to within 15.2% in the Y direction over a 50 µm distance, with the cell placed at the center of the 50 µm x 50 µm x 50 µm computational region. The vector plot in Figure 5.14 shows that the electric field propagates in the X direction in the region containing the cell.

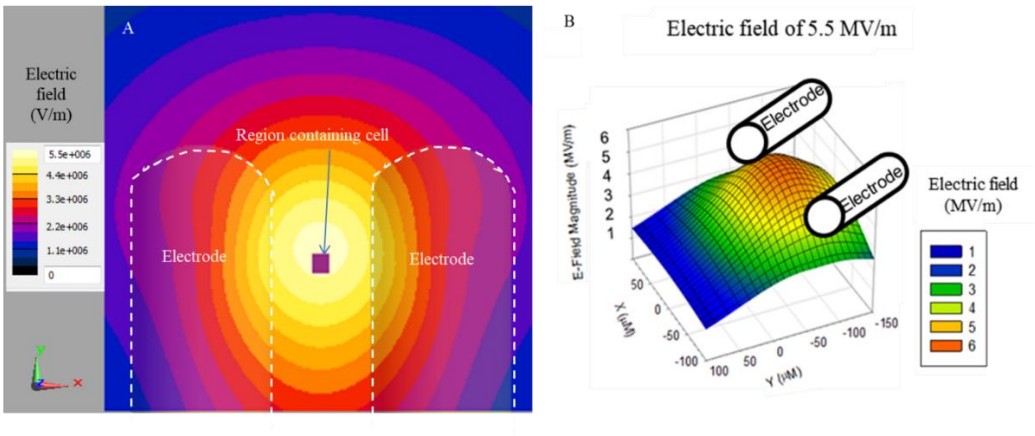

Figure 5.13: Computed electric field for tungsten rod electrode tips placed 35 µm above the surface of the glass bottom dish. A) A contour slice normal to the Z axis shows that the electric field was 5.5 MV/m at the location of the cell. B) The surface plot normal to the Z axis shows that the electric field magnitude remains at 5.5 MV/m over a distance larger than the diameter of a chromaffin cell.

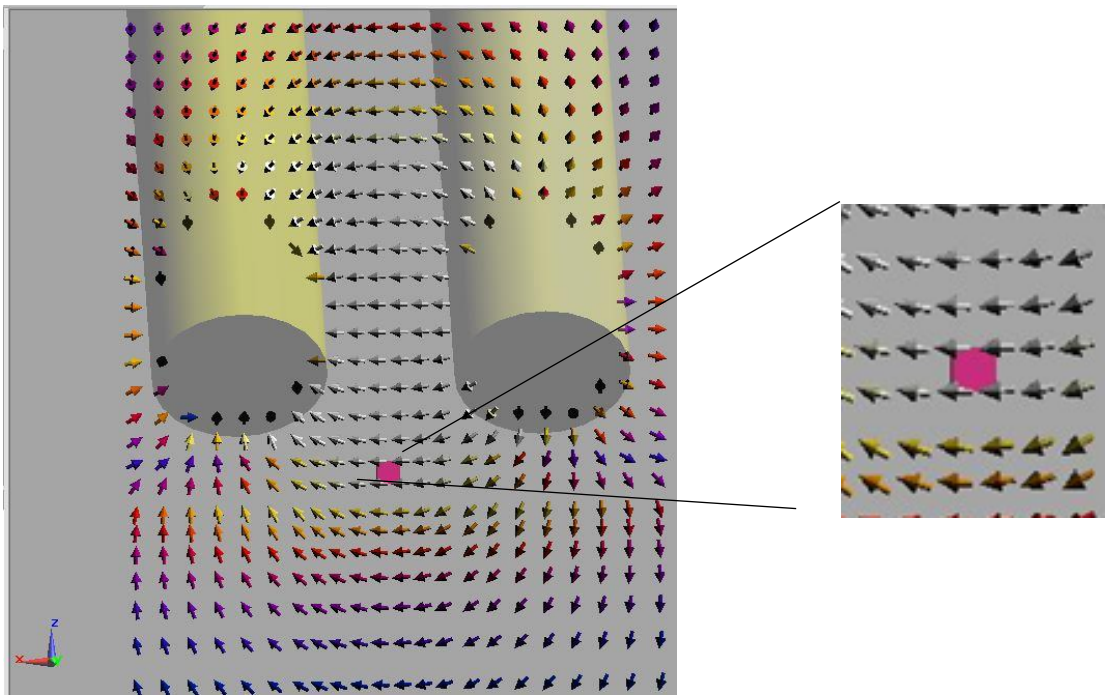

Figure 5.14: Vector plot showing the direction of the electric field distribution in the Y plane with electrodes placed 35 µm above the glass bottom dish. The direction of the electric field at the location of the cell is only in the X direction.

Figure 5.15 shows a contour plot of the computed electric field distribution normal to the Z axis with electrodes placed 45 µm above the surface of the glass dish. In this case, the electric field magnitude decreased to 4.6 MV/m in the region containing the cell, remaining constant at 4.6 MV/m over a distance of 50 µm in the X, Y, and Z directions. That is, the electric field magnitude was constant in the Z direction over a distance of 50 µm, homogeneous to within 4.0 % in the X direction over a 50 µm distance, and homogeneous to within 15.1% in the Y direction over a 50 µm distance, with the cell placed at the center of the 50 µm x 50 µm x 50 µm computational region. The vector plot in Figure 5.16 shows that the electric field propagates in the X direction as well.

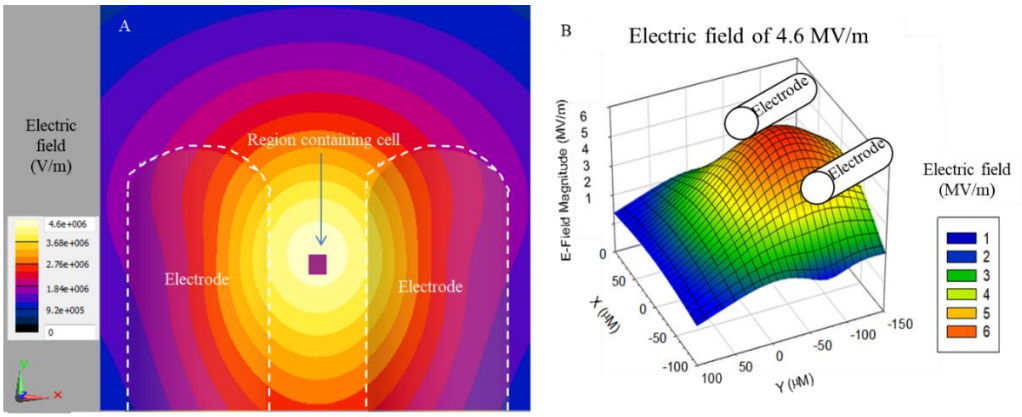

Figure 5.15: Computed electric field for tungsten rod electrode tips placed 45 µm above the surface of the glass bottom dish. A) A contour slice normal to the Z axis shows that the electric field was 4.6 MV/m at the location of the cell. B) The surface plot normal to the Z axis shows that the electric field magnitude remains at 4.6 MV/m over a distance larger than the diameter of a chromaffin cell.

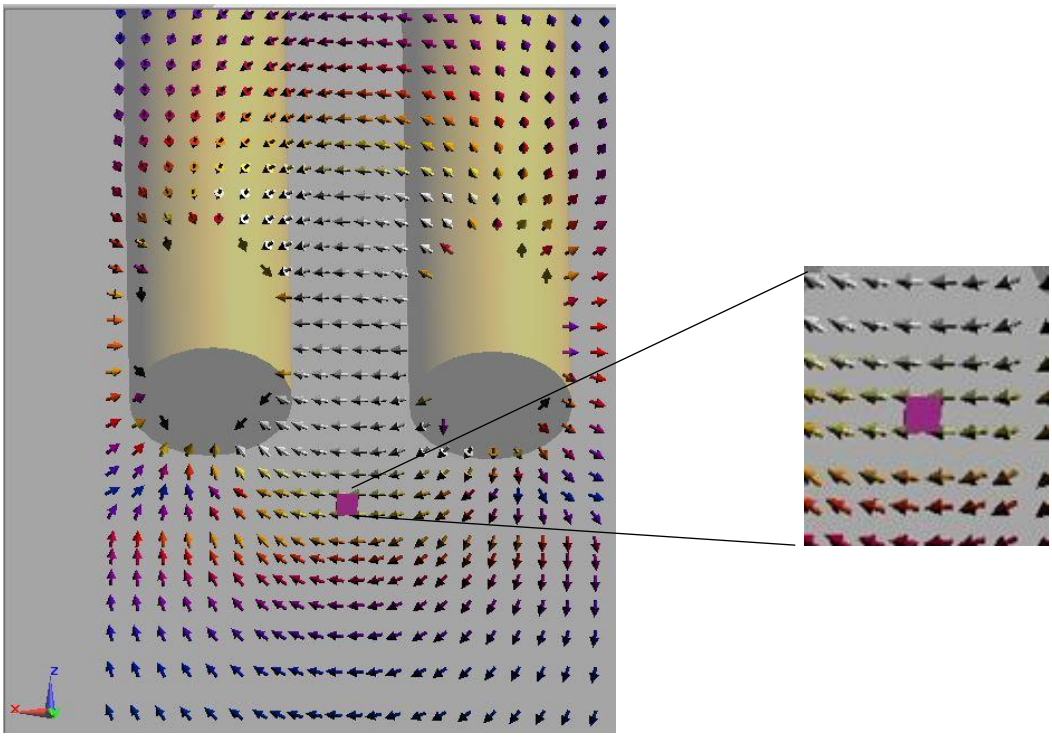

Figure 5.16: Vector plot showing the direction of the electric field distribution in the Y plane with electrodes placed 45 µm above the glass bottom dish. The direction of the electric field at the location of the cell is only in the X-direction.

Taken as a whole, these results suggest that the electric field, though slightly different in magnitude when the electrode tips are placed at slightly different heights above

the bottom of the cell dish, was constant in the Z direction over a distance of 50 µm, with slight variations in the X and Y directions. Therefore, cells are exposed to an acceptable homogeneous electric field magnitude under each of these exposure conditions [1].

5.5.2 Calcium responses evoked by pulses delivered with electrode tips placed 35 µm and 45 µm above the surface of the glass bottom dish

Although the simulations showed that misplacement of the electrode tips affected the electric field magnitude to which a cell was exposed, we would not have expected that the differences in electric field magnitude would be significant enough to affect calcium responses. This is because the threshold for a 5 ns pulse to evoke calcium influx via VGCCs, which is an all-or-none process, is 3 MV/m [5]. As shown in Figure 5.17, there were no significant differences in the calcium responses compared to those observed with the electrode tips placed 40 µm above the surface of the glass bottom dish (compare with responses in Figure 3.2). Thus, minor misplacement of the electrodes that causes cells to be exposed to slightly different electric field magnitudes does not impact 5 ns evoked calcium responses.

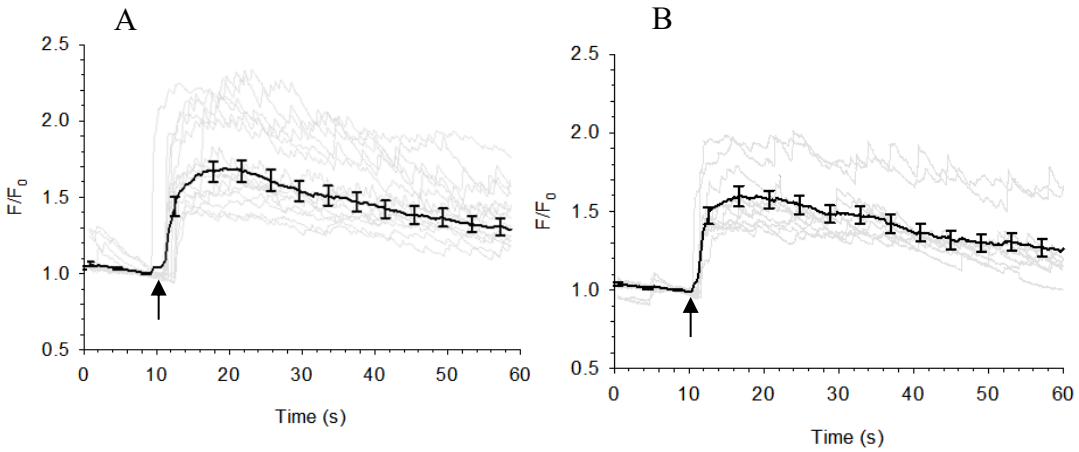

Figure 5.17: Calcium responses in chromaffin cells stimulated with a 5 ns pulse when the tungsten rod electrode tips were placed at two different heights above the surface of the glass bottom dish. A) Electrode tips placed at 35 µm (N=10) and B) at 45 µm (N=10) above the glass bottom dish.

5.6 Tungsten rod exposure system: Misaligned electrode tips

During electrode fabrication, there could be some misalignment of the electrode tips such that one electrode tip is longer than the other. We therefore computed the electric field magnitude at the location of a cell when one electrode tip was 5 µm shorter in length than the other electrode tip. As for previous simulations, the cell was represented by a single cubical voxel of dimension 16 µm. As shown in Figure 5.18, the misalignment of the electrode tips caused an increase in the electric field magnitude to 5.2 MV/m. The electric field magnitude is homogeneous in the Z direction over a 50 µm distance, homogeneous to within 6.2% in the X direction over a 50 µm distance, homogeneous to within 10.5% in the Y direction over a 50 µm distance, with the cell placed at the center of the 50 µm x 50 µm x 50 µm computational region. Figure 5.19 shows further that the

electric field propagates in the X direction in the region containing the cell. These results suggest that misalignment of the electrode tips, while causing a slight increase in electric field magnitude, does not affect the direction or homogeneity of the electric field.

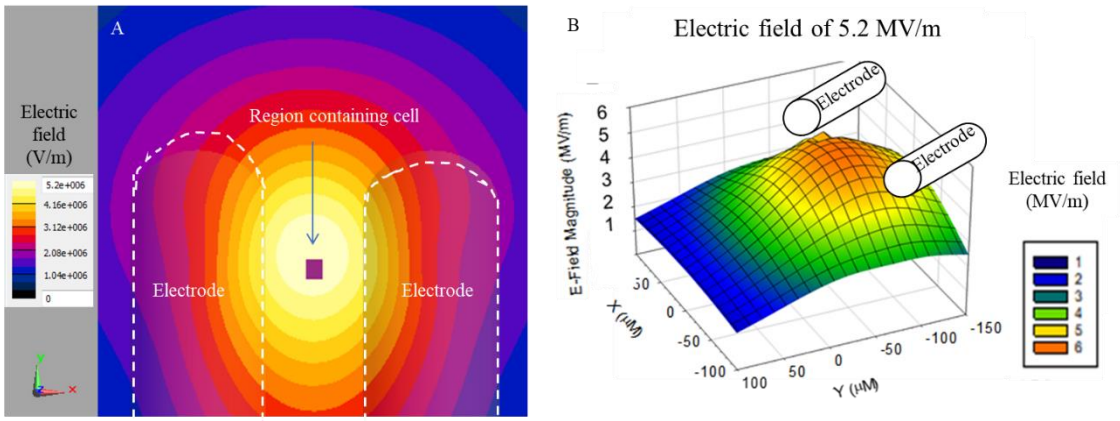

Figure 5.18: Computed electric field for misaligned tungsten rod electrode tips. A) A contour slice normal to the Z axis shows that the electric field was 5.2 MV/m at the location of the cell. B) The surface plot normal to the Z axis shows that the electric field magnitude remains at 5.2 MV/m over a distance larger than the diameter of a chromaffin cell.

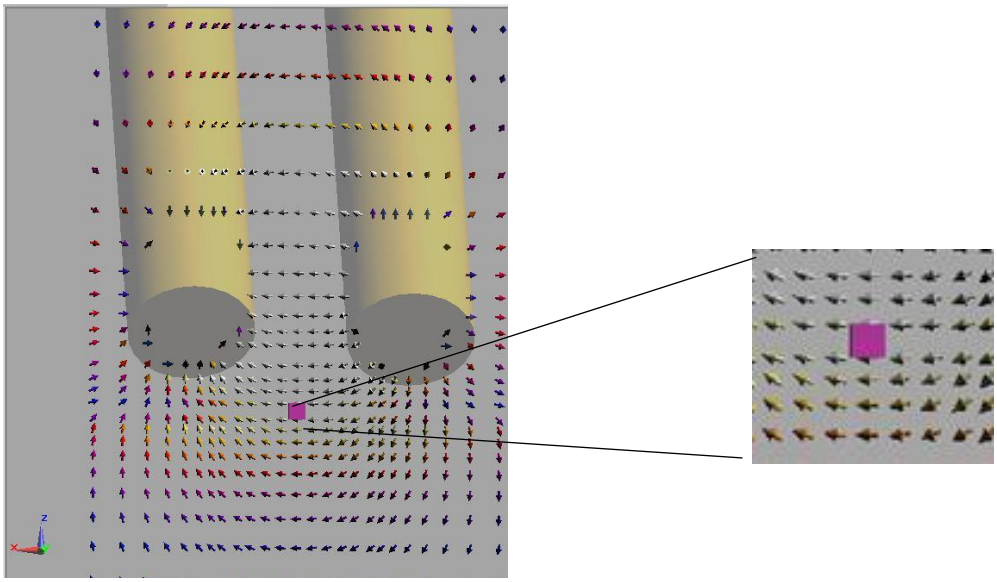

Figure 5.19: Vector plot showing the direction of the electric field distribution in the Y plane with misaligned electrode tips. The direction of the electric field at the location of the cell is only in the X-direction.

5.7 Homogeneity in the region containing the cell for the tungsten rod exposure system at a single frequency

After establishing the electric field magnitude of the tungsten rod exposure system with the rods placed 35 µm, 40 µm, and 45 µm above the surface of the glass bottom dish, as well as for misaligned electrode tips, the homogeneity of the electric field in the vicinity of the region containing the cell was computed at the frequency of 60 MHz that encompasses most of the pulse's energy (Section 4.3). Moreover, whereas the previous simulations were performed with a coarse mesh with the cell having a step size of 16 µm, in the following sections the region containing the cell was further discretized with a step size of 4 µm for the tungsten rod exposure system and 1 µm for the gold strip chamber exposure system in the Huygens box simulation, thereby providing the computed electric field magnitude with higher resolution. The following sections show the results using line plots of the electric field magnitude extracted over a distance of 20 µm in the region containing the cell, along with vector plots of the electric field direction.

5.7.1 Tungsten rod electrodes: Computations at 60 MHz

At 60 MHz, the electric field magnitude homogeneity in the initial computational domain (Figure 5.20) was computed over a distance of 20 µm in each direction based on the line plots. The electric field was homogeneous within 7% in the X direction, uniform in Y direction, and within 7% in the Z direction. Furthermore, there was no change in the

direction of the electric field in the region containing the cell (Figure 5.21). These simulations showed that the cell is in an acceptably homogeneous region [1].

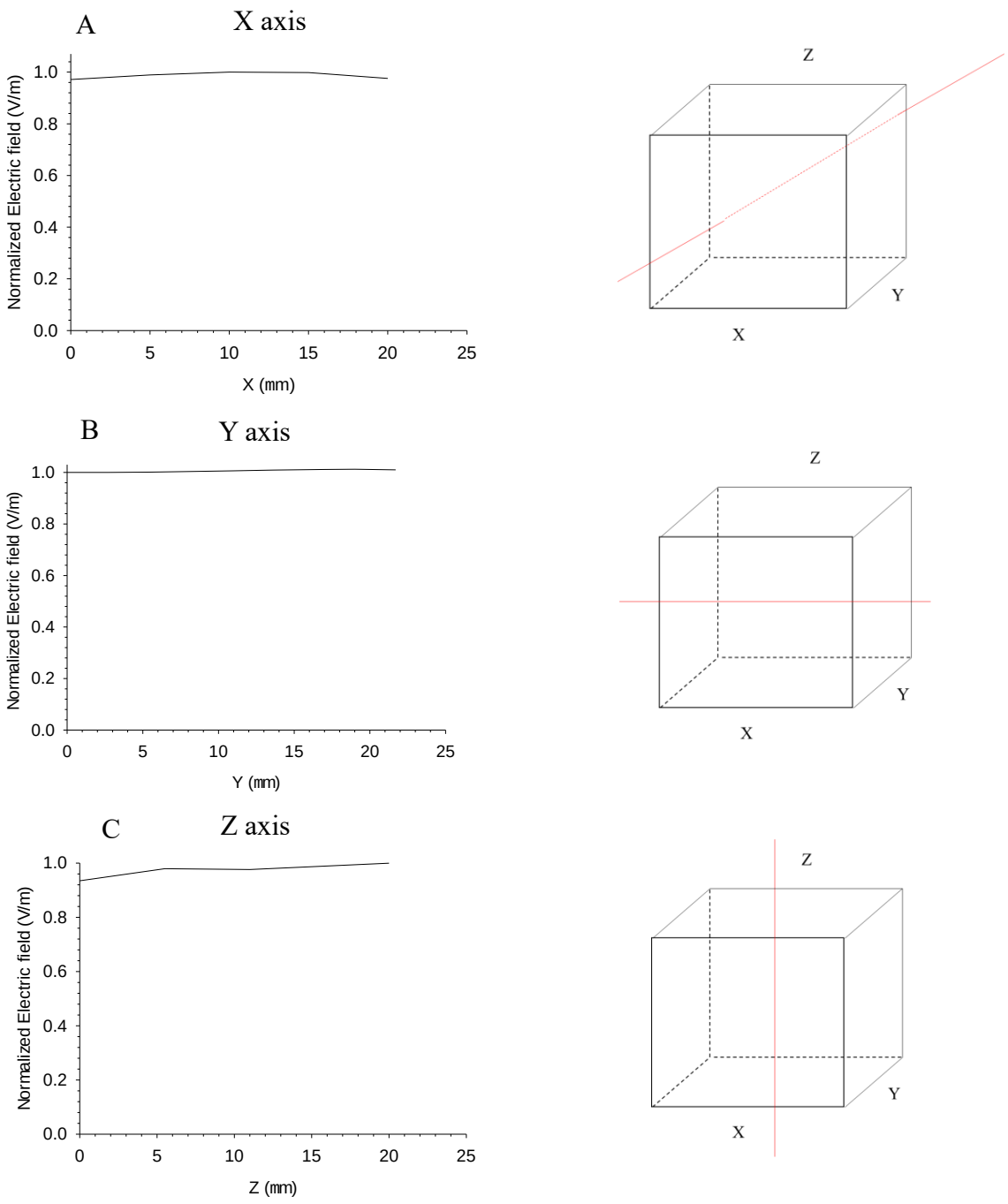

Figure 5.20: Computed distribution of the electric field magnitude for the tungsten rod exposure system at 60 MHz along the X, Y, Z directions. The homogeneity in the electric field magnitude axis over a distance of 20 µm in the A) X direction was within 7%, B) constant in the Y direction, C) and within 7% in the Z direction. The electric field was normalized to 1 and the purple box represents the area of the cell along that axis. The cube on the right of each graph represents the cell with the red line marking the line of extraction for each line plot.

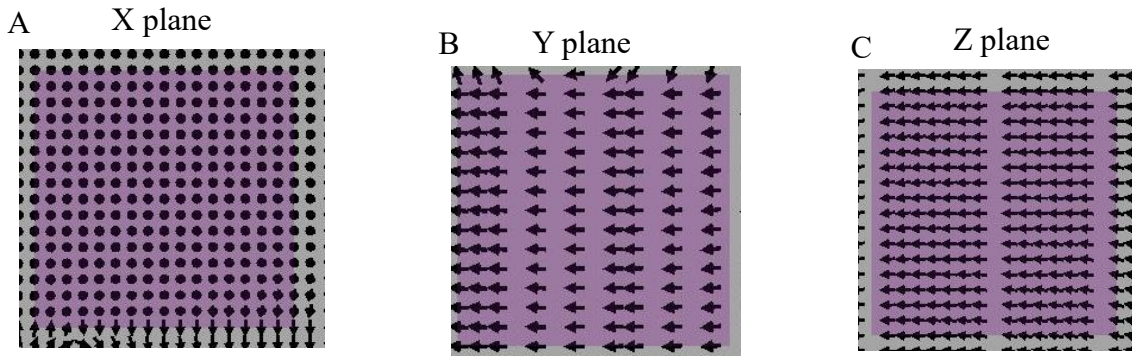

Figure 5.21: Vector plot showing the direction of the electric field distribution in the X, Y, and Z planes at 60 MHz for the tungsten rod exposure system in the region containing the cell. The vector plots show that the electric field propagates in the X direction only. The purple box represents the region containing the cell along each axis.

5.8 Gold strip chamber exposure system: Control Simulations

Simulations of the gold strip chamber exposure were performed and the homogeneity in the electric field magnitude was calculated in the same manner as for the tungsten rod exposure system. First, control simulations were performed to verify that the electric field magnitude distribution of magnitude 7 MV/m was the same as previously published [2], with the cell being represented by a single voxel at a step size of 16 μm. The homogeneity in the electric field magnitude over a distance of 20 μm in the Z direction (starting at the bottom of the cell resting on the glass surface and 20 μm above the glass surface) and 20 μm in both X and Y directions with the cell in the center was computed. The electric field magnitude was constant in the Z direction over a distance of 20 μm, homogeneous to within 0.1% in the X direction, and homogeneous to within 0.01 % in the Y direction.

After completing a simulation at 7 MV/m, a simulation was performed to compute the electric field distribution at 5 MV/m, which is the electric field magnitude at which the distributions for both the exposure systems will be compared. Figure 5.22 shows the electric field magnitude and direction distribution at 5 MV/m in the gold strip chamber exposure system with the cell represented as a single voxel (step size of 16 μm). The vector field view shows that the cell is exposed to the electric field in the X direction. The electric field magnitude is constant in the Z direction over a distance of 20 μm, homogeneous to within 0.1% in the X direction, and homogeneous to within 0.01 % in the Y direction.

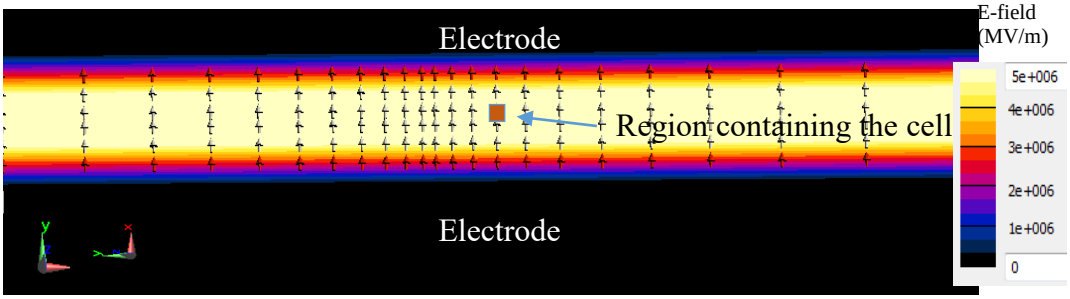

Figure 5.22: Electric field magnitude and direction within the gold strip chamber exposure system. The cell is exposed to an electric field of 5 MV/m in the X direction only. The black regions are where the gold strips are located, and where the computed electric field magnitude is zero as expected.

5.9 Homogeneity in the region containing the cell in the gold strip chamber exposure system at a single frequency

In order to compare the homogeneity in the electric field magnitude generated by the gold strip chambers to that of the tungsten rod exposure system, a 60 MHz simulation was performed.

5.9.1 Gold strip chambers: Computations at 60 MHz

At 60 MHz, the electric field magnitude homogeneity in the initial computational domain (Figure 5.23) was computed over a distance of 20 μm in each direction based on the line plots. The electric field was homogeneous within less than 1% in the X direction, within 19% in the Y direction, and within 18% in the Z direction. In addition, there was no change in the direction of the electric field in the region containing the cell (Figure 5.24). This showed that the cell is in an acceptably homogeneous region [1].

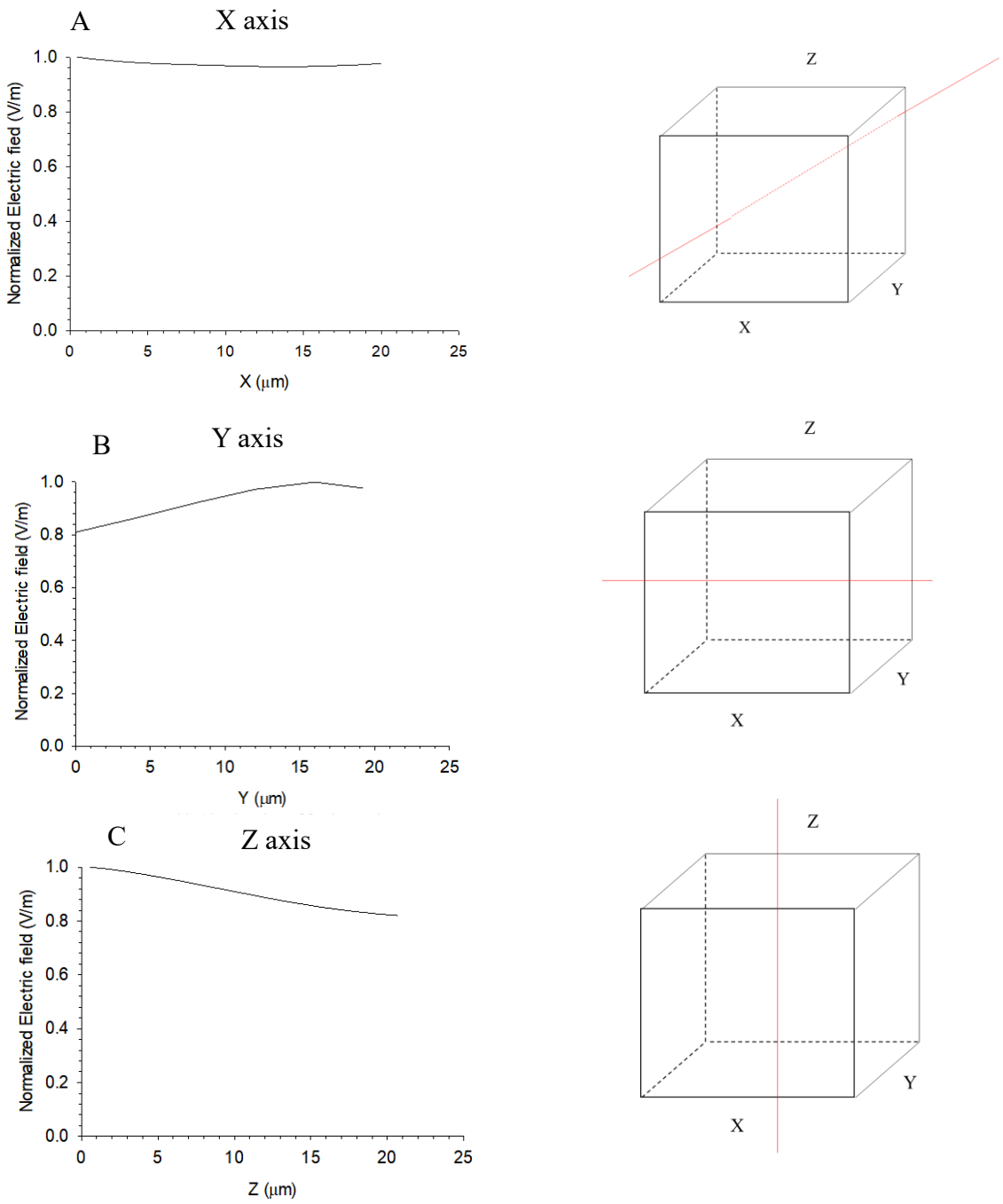

Figure 5.23: Computed distribution of the electric field magnitude for the gold strip chamber exposure system at 60 MHz along the X, Y, Z directions. The homogeneity in the electric field magnitude axis over a distance of 20 µm in the A) X direction was within less than 1%, B) within 20% in the Y direction, C) and within 18% in the Z direction. The electric field was normalized to 1 and the purple box represents the area of the cell along that axis. The cube on the right of each graph represents the cell with the red line marking the line of extraction for each line plot.

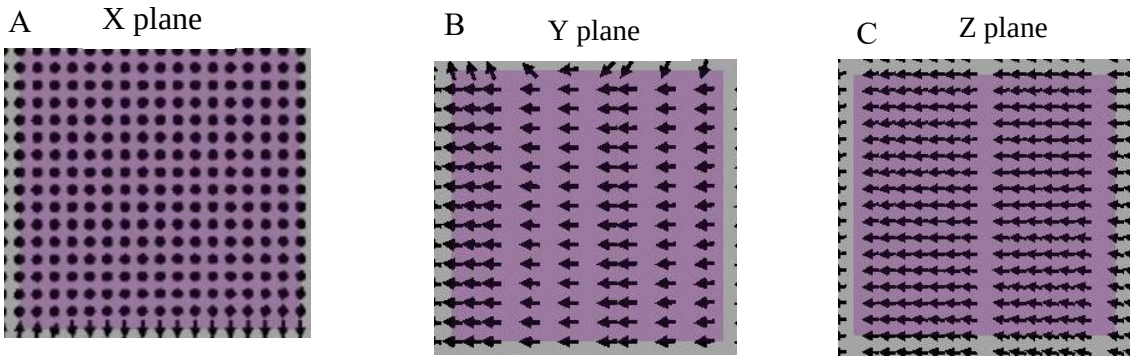

Figure 5.24: Vector plot showing the direction of the electric field distribution in the X, Y, and Z planes at 60 MHz for the gold strip chamber exposure system in the region containing the cell. The vector plots show that the electric field propagates in the X direction only. The purple box represents the region containing the cell along each axis.

5.10 Summary and Conclusions

The Huygens box simulations showed that the region containing a chromaffin cell is exposed to a homogeneous electric field magnitude at 60 MHz in both exposure systems. There are minor differences in homogeneity in the X and Y directions between the tungsten rod and gold strip chambers exposure systems as shown in Figure 5.25, but they are not significant enough to cause a large deviation in the electric field magnitude [1]. In addition, there are also no major differences in other electric field parameters, such as the direction of the electric field (Figure 5.26), that could account for the variability in calcium responses observed with each exposure system.

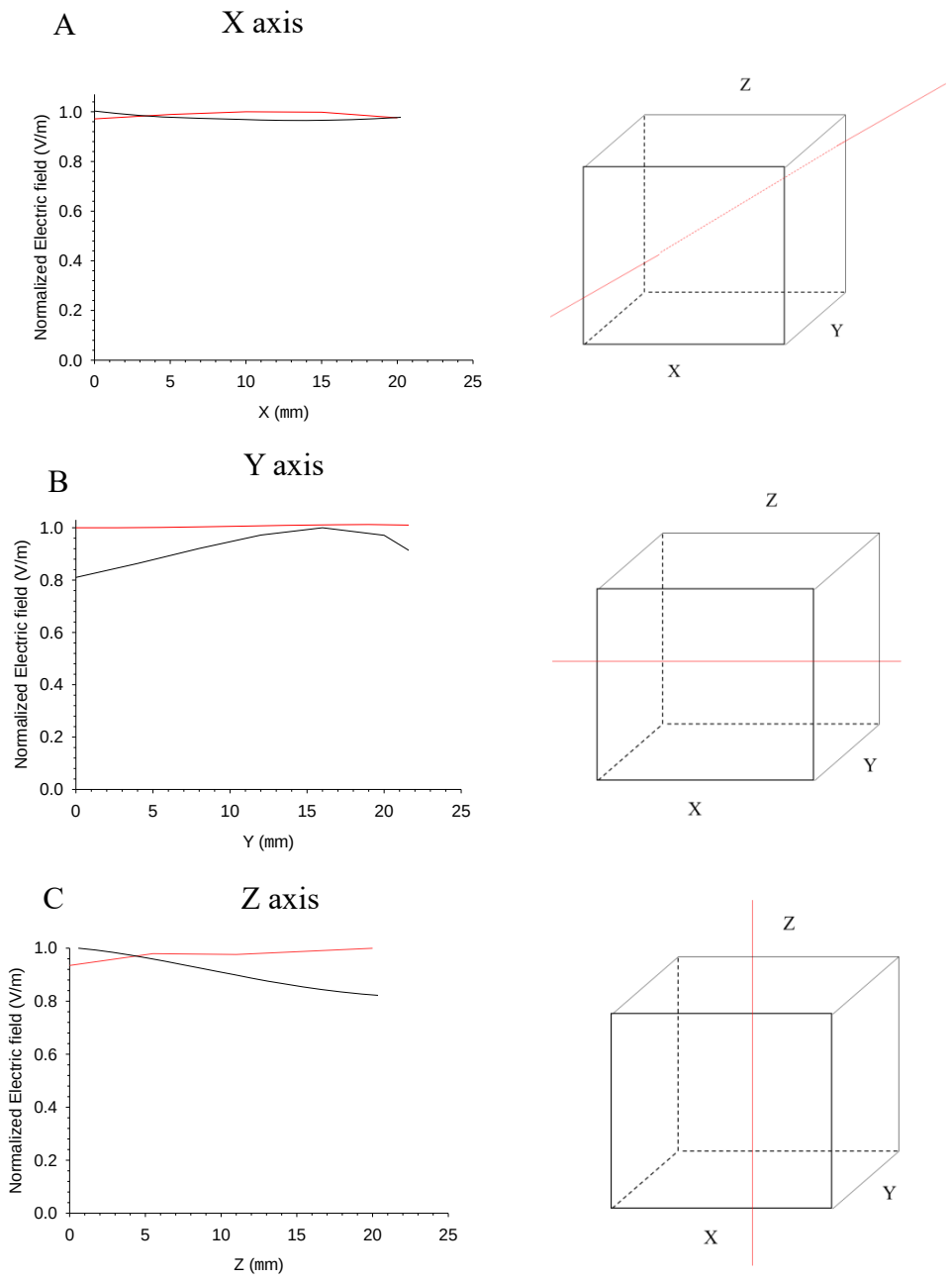

Figure 5.25: Comparison of the distribution of the electric field magnitude for the gold strip chamber and tungsten rod exposure systems at 60 MHz along the X, Y, Z directions. The homogeneity in the electric field magnitude axis over a distance of 20 µm in both exposure systems (red: tungsten rod exposure system, black: gold strip chamber exposure system) is within acceptable limits. There is no significant difference in the homogeneity in the A) X direction between, B) in the Y direction in, and C) in the Z direction in. The cube on the right of each graph represents the cell with the red line marking the line of extraction for each line plot.

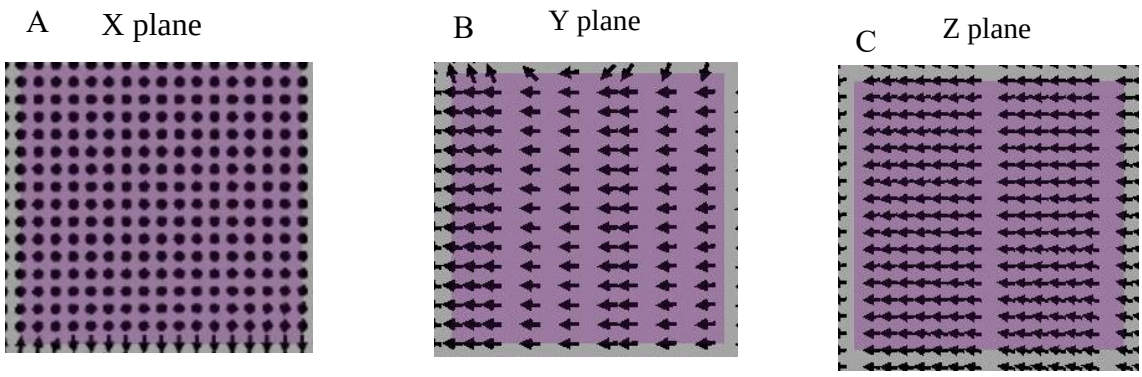

Figure 5.26: Comparison of the vector plots of the electric field in both exposure systems. The vector plots show that the electric field propagates in the X direction only in both exposure systems. The purple box represents the region containing the cell.

From these results we conclude that although the two exposure systems are different in design and deliver the same 5 ns electric pulse, the region containing the cell is exposed to the same homogeneous electric field and electric field direction in each case.

The simulations further showed that for the tungsten rod exposure system, placing the electrode tips 35 μm from the surface of the glass bottom dish causes an increase of 0.5 MV/m in the electric field magnitude compared to that when electrode tips are placed 40 μm from the surface of the glass bottom dish. Placing the electrode tips at 45 μm causes a decrease of 0.4 MV/m in the electrode field magnitude. Likewise, misaligned electrode tips caused a minor increase of 0.2 MV/m in the electric field magnitude. Importantly, in each case the homogeneity of the electric field or its direction in the region containing an exposed cell is not affected.

References:

[1] Kuster, N. and Schonborn, F. (2000). Recommended minimal requirements and development guidelines for exposure setups of bio-experiments addressing the health risk concern of wireless communications. *Bioelectromagnetics*, 21(7), pp.508-514.

[2] G. Craviso, P. Chatterjee, G. Maalouf, A. Cerjanic, J. Yoon, I. Chatterjee, and P. Vernier, "Nanosecond electric pulse-induced increase in intracellular calcium in adrenal chromaffin cells triggers calcium-dependent catecholamine release," *IEEE Transactions on Dielectrics and Electrical Insulation*, vol. 16, no. 5, pp. 1294–1301, 2009.

[3] G. L. Craviso, S. Choe, P. Chatterjee, I. Chatterjee, and P. T. Vernier, "Nanosecond Electric Pulses: A Novel Stimulus for Triggering Ca^{2+} Influx into Chromaffin Cells Via Voltage-Gated Ca^{2+} Channels," *Cellular and Molecular Neurobiology*, vol. 30, no. 8, pp. 1259–1265, 2010.

[4] G. L. Craviso, S. Choe, I. Chatterjee, and P. T. Vernier, "Modulation of intracellular Ca^{2+} levels in chromaffin cells by nanoelectropulses," *Bioelectrochemistry*, vol. 87, pp. 244–252, 2012.

[5] J. Zaklit, G. L. Craviso, N. Leblanc, L. Yang, P. T. Vernier, and I. Chatterjee, "Adrenal Chromaffin Cells Exposed to 5-ns Pulses Require Higher Electric Fields to Porate Intracellular Membranes than the Plasma Membrane: An Experimental and Modeling Study," *The Journal of Membrane Biology*, vol. 250, no. 5, pp. 535–552, 2017.

Chapter 6: Discussion

6.1 Introduction

The effects of electric pulses in the low nanosecond duration range (less than 10 ns) are being investigated by our group for their potential application for targeted non-invasive neurostimulation. The ultimate goal is an alternative to surgical implantation of electrodes that serves as an electrostimulation method in procedures such as deep brain stimulation. To work toward this goal, we are using a well-characterized neural-type cell model, adrenal chromaffin cells, to investigate the effects of nanosecond electric pulses, specifically pulses that are 5 ns in duration, on the neurosecretory function of the cells. Our laboratory has shown that the application of a 5 ns pulse mimics the actions of acetylcholine to evoke calcium-dependent catecholamine release by causing activation of VGCCs and a rise in intracellular calcium [1-4]. However, calcium responses evoked by the pulse are more prolonged in duration compared to those evoked by the physiological stimulus. Because of the importance of understanding how and why 5 ns pulses trigger calcium responses that exhibit a slower return of calcium to pre-stimulus levels, our first aim was to investigate the effects of these pulses on the mitochondria, the main organelle involved in rapid calcium clearance. Moreover, because calcium responses were also shown to differ in duration depending on which NEP exposure system was used for experiments (i.e., a gold strip chamber and a tungsten rod exposure system), our second aim was to carry out refined numerical simulations to determine the extent to which the electric field distribution differed between the exposure systems.

6.2 5 ns pulses have no apparent effect on the mitochondrial membrane potential

When chromaffin cells are stimulated and calcium enters via VGCCs, mitochondria rapidly clear the calcium once the stimulus has ended. Mitochondria accomplish this by utilizing the mitochondrial membrane potential as the driving force for taking up calcium ions [5-7]. Perturbations or possible collapse of the mitochondrial membrane potential by protonophores, such as CCCP and FCCP, has been shown to cause a delay in calcium clearance [8-11]. The effects of these protonophores vary by concentration in different cell types. For example, the I_{C50} (maximal concentration of a substance that causes 50% inhibition of an enzyme or function) for CCCP has been reported to be 0.3 µM for myocardial cells and 0.55 µM for Jurkat cells [12-13]. As for FCCP, the I_{C50} has been reported to be 0.02 µM for human neutrophils, 1.31 µM for human hepatocellular carcinoma cells, and 7 µM for human hepatocellular carcinoma cells [14-16]. For our experiments we treated chromaffin cells with concentrations of CCCP and FCCP close to and higher than these ranges to obtain an effect in chromaffin cells. We started by treating the cells with 2 µM CCCP since this concentration was reported to cause an increase in the half-width of the calcium responses in these cells [8]. At this concentration, applying 5 applications of 100 µM DMPP resulted in calcium responses exhibiting a pronounced decrease in amplitude relative to control cells, with similar results observed with cells treated with 1 µM CCCP, and FCCP at 2 µM and 1 µM. At 0.5 µM CCCP, calcium responses were variable, with amplitudes that were either similar to those of the control

cells or much smaller. The decrease in amplitude most likely can be attributed to non-specific effects of CCCP. For example, CCCP has been shown to decrease calcium currents through L-type channels by indirectly disrupting ATP production [17-18]. In addition, when mitochondrial membrane potential is disrupted, several cellular mechanisms are also affected that result in a decrease in ATP production, a decrease in respiration, an increase in ROS production, and changes in pH levels [17-18]. Therefore, our experiments suggested that CCCP and FCCP altered the calcium responses of chromaffin cells in our hands but the effects of CCCP and FCCP may not have been limited to the mitochondria.

Before proceeding to study the effects of NEPs on mitochondrial membrane potential, we first established that in cells in which mitochondria were labeled with TMRE, CCCP caused a decrease in fluorescence, which would be indicative of a disruption in mitochondrial membrane potential. For these experiments, chromaffin cells were treated with CCCP at concentrations of 1 µM, 2 µM, 8 µM, or 10 µM. The results showed that TMRE fluorescence did not undergo a decrease at 1 µM and 2 µM CCCP that caused significant effects on the amplitude of calcium responses to DMPP. Only at CCCP concentrations of 8 µM and higher was a decrease in TMRE fluorescence observed (up to 35%-50%). While we have no explanation for this finding, it may be that using mitochondrial membrane potential dyes for assessing changes in mitochondrial membrane potential in conjunction with widefield fluorescence microscopy is not sensitive enough.

We did not detect convincing evidence of a change in mitochondrial membrane potential in cells exposed to a singe 5 ns, 5 MV/m pulse, to a train of five and ten pulses at 5 MV/m, or to a single pulse applied at electric field magnitudes of 10 and 15 MV/m. In fact, the small changes in fluorescence (less than 2%) that were observed in some cells

were also observed in cells exposed to multiple applications of DMPP. From these results it can concluded that NEPs do not cause an effect on mitochondrial membrane potential disruption that could account for why calcium responses are prolonged in duration.

6.3 The electric field distribution in the region containing a cell is homogenous to the same degree in each NEP exposure system

Our laboratory has studied the effects of 5 ns pulses on chromaffin cells by exposing the cells to 5 ns pulses using either a gold strip chamber or tungsten rod exposure system. In cells exposed to a pulse using the gold strip chamber exposure system, calcium returns to pre-stimulus calcium levels with half-widths ranging from 8 to 11 s [1, 3] versus a half-width of 23 s or greater for cells exposed to a pulse using the tungsten rod exposure system. To understand the basis for these variations in cell response duration, we investigated whether there are differences in the homogeneity in the magnitude and other parameters of the electric field in both exposure systems using the Huygens box approach. The advantage of using this approach was the ability to conduct simulations with finer discretization of the region containing a cell together with a significant reduction in the simulation time. Previous simulations had the region containing the cell discretized with a mesh size of 16 μm. In the simulations presented in this thesis, this region was further discretized (with a mesh size of 4 μm for the tungsten rod exposure system and 1 μm for the gold strip chamber exposure system) for the Huygens box simulation. The homogeneity in the electric field generated by the tungsten rod exposure system in the Huygens box computational domain at a frequency of 60 MHz was homogenous (over a distance of 20

μm in each direction) within 7% in the X direction, constant in the Y direction, and within 7% in the Z directions, which was acceptable [19]. As for the gold strip chambers, the homogeneity in the electric field distribution in the Huygens box simulations at a frequency of 60 MHz was homogeneous within 1% in the X direction, within 20% in the Y direction, and within 18% in the Z direction, which was acceptable [19]. Although there are minor differences in homogeneity in the exposure systems, the differences are not significant enough to cause a large deviation in the electric field magnitude in the region containing the cell. In addition, differences in the direction of the electric field in the region containing the cell in the exposure systems were also not significant. From these results we conclude that when comparing the two exposure systems, the differences in electric field homogeneity in the region containing the cell are too minor to account for the variation in calcium responses.

With respect to the tungsten rod exposure system, we also determined that when the electrodes are placed 5 μm below or above the target position of 40 μm above the glass bottom dish, there are no significant differences in calcium responses even though numerical simulations determined that the electric field is different at each height. That is, at 40 μm the electric field at the location of the cells is 5.0 MV/m, at 45 μm the electric field is 4.6 MV/m, and at 35 μm the electric field is 5.5 MV/m. Our conclusion is that during experiments, placement of the electrode tips could be off by ± 5 μm without having an impact on cell responses. Likewise, misalignment of the electrode tips such that one electrode tip is longer than the other also has no impact. Although experiments with misaligned electrode tips were not conducted, numerical simulations showed a computed electric field of 5.2 MV/m, which falls in the electric field range established for electrodes

placed 5 µm below or above the target position of 40 µm. Thus, calcium responses would not be affected by electrode tips having slightly different lengths.

6.4 Future directions

Since the results of our studies raise the possibility that the method that we used for detecting changes in mitochondrial membrane potential may not have been sensitive enough, repeating experiments with the mitochondria labeled with a quantitative, cationic dye such as JC-1 (5,5′,6,6′-tetrachloro-1,1′,3,3′-tetraethylbenzimi-dazolylcarbocyanine iodide), which distinguishes minute changes in the mitochondrial membrane potential by forming JC-1 aggregates and JC-1 monomers that can be viewed under two different wavelengths [20-21]. This particular dye is more sensitive in detecting changes in the mitochondrial membrane potential because it allows for thorough assessment of the labeled mitochondria at two different wavelengths, whereby a decrease in JC-1 aggregates indicates a decrease in mitochondrial membrane potential [20-21]. If these experiments still do not show an effect of NEPs on mitochondrial membrane potential, other mechanisms that may be involved in prolonging intracellular calcium levels would need to be explored. One series of experiments could determine whether NEPs affect the activity of the plasma membrane calcium ATPase and/or the plasma membrane Na^{+}/Ca^{2+} exchanger. Other experiments could be to examine the extent to which calcium release from the ER or calcium influx via VGCCs continues after pulse delivery.

As for computational studies, since the magnitude and direction of the electric field were not significantly different in each exposure system, it is important to consider other factors between the two geometries. For example, the current density between the two electrodes in each exposure may be different. Once the basis for the different calcium responses evoked by the two exposure systems is identified, further studies would be directed at designing geometries of the rod exposure system that evoke less sustained calcium responses.

References:

[1] J. Zaklit, G. L. Craviso, N. Leblanc, L. Yang, P. T. Vernier, and I. Chatterjee, "Adrenal Chromaffin Cells Exposed to 5-ns Pulses Require Higher Electric Fields to Porate Intracellular Membranes than the Plasma Membrane: An Experimental and Modeling Study," *The Journal of Membrane Biology*, vol. 250, no. 5, pp. 535–552, 2017.

[2] G. L. Craviso, S. Choe, P. Chatterjee, I. Chatterjee, and P. T. Vernier, "Nanosecond Electric Pulses: A Novel Stimulus for Triggering Ca^{2+} Influx into Chromaffin Cells Via Voltage-Gated Ca^{2+} Channels," *Cellular and Molecular Neurobiology*, vol. 30, no. 8, pp. 1259–1265, 2010.

[3] G. L. Craviso, S. Choe, I. Chatterjee, and P. T. Vernier, "Modulation of intracellular Ca^{2+} levels in chromaffin cells by nanoelectropulses," *Bioelectrochemistry*, vol. 87, pp. 244–252, 2012.

[4] G. Craviso, P. Chatterjee, G. Maalouf, A. Cerjanic, J. Yoon, I. Chatterjee, and P. Vernier, "Nanosecond electric pulse-induced increase in intracellular calcium in adrenal chromaffin cells triggers calcium-dependent catecholamine release," *IEEE Transactions on Dielectrics and Electrical Insulation*, vol. 16, no. 5, pp. 1294–1301, 2009.

[5] P. Bernardi and A. Rasola, "Calcium and Cell Death: The Mitochondrial Connection," *Subcellular Biochemistry Calcium Signalling and Disease*, pp. 481–506.

[6]N. Demaurex, D. Poburko, and M. Frieden, "Regulation of plasma membrane calcium fluxes by mitochondria," *Biochimica et Biophysica Acta (BBA) - Bioenergetics*, vol. 1787, no. 11, pp. 1383–1394, 2009.

[7] D. G. Nicholls, “Mitochondria and calcium signaling,” *Cell Calcium*, vol. 38, no. 3-4, pp. 311–317, 2005.

[8] E. Alés, J. Fuentealba, A. G. García, and M. G. López, “Depolarization evokes different patterns of calcium signals and exocytosis in bovine and mouse chromaffin cells: the role of mitochondria,” *European Journal of Neuroscience*, vol. 21, no. 1, pp. 142–150, 2005.

[9] A. Caricati-Neto, J.-F. Padín, E.-D. Silva-Junior, J.-C. Fernández-Morales, A.-M. G. D. Diego, A. Jurkiewicz, and A. G. García, “Novel features on the regulation by mitochondria of calcium and secretion transients in chromaffin cells challenged with acetylcholine at 37°C,” *Physiological Reports*, vol. 1, no. 7, 2013.

[10] D.-M. Yang and L.-S. Kao, “Relative contribution of the Na /Ca2 exchanger, mitochondria and endoplasmic reticulum in the regulation of cytosolic Ca2 and catecholamine secretion of bovine adrenal chromaffin cells,” *Journal of Neurochemistry*, vol. 76, no. 1, pp. 210–216, 2008.

[11] M. Montero, M. T. Alonso, E. Carnicero, I. Cuchillo-Ibáñez, A. Albillos, A. G. García, J. García-Sancho, and J. Alvarez, “Chromaffin-cell stimulation triggers fast millimolar mitochondrial Ca2 transients that modulate secretion,” *Nature Cell Biology*, vol. 2, no. 2, pp. 57–61, 1999.

[12] A. Dumesic, A. A. Guedikian, V. K. Madrigal, J. D. Phan, D. L. Hill, J. P. Alvarez, and G. D. Chazenbalk, “Cumulus Cell Mitochondrial Resistance to Stress In Vitro Predicts Oocyte Development During Assisted Reproduction,” *The Journal of Clinical Endocrinology & Metabolism*, vol. 101, no. 5, pp. 2235–2245, 2016.

[13] D. Piwnica-Worms, J. F. Kronauge, and M. L. Chiu, “Uptake and retention of hexakis (2-methoxyisobutyl isonitrile) technetium(I) in cultured chick myocardial cells.

Mitochondrial and plasma membrane potential dependence.," *Circulation*, vol. 82, no. 5, pp. 1826–1838, 1990.

[14] S. Sakamuru, X. Li, M. S. Attene-Ramos, R. Huang, J. Lu, L. Shou, M. Shen, R. R. Tice, C. P. Austin, and M. Xia, "Application of a homogenous membrane potential assay to assess mitochondrial function," *Physiological Genomics*, vol. 44, no. 9, pp. 495–503, 2012.

[15] M. D. Brand and D. G. Nicholls, "Assessing mitochondrial dysfunction in cells," *Biochemical Journal*, vol. 435, no. 2, pp. 297–312, 2011.

[16] G. Fossati, D. A. Moulding, D. G. Spiller, R. J. Moots, M. R. H. White, and S. W. Edwards, "The Mitochondrial Network of Human Neutrophils: Role in Chemotaxis, Phagocytosis, Respiratory Burst Activation, and Commitment to Apoptosis," *The Journal of Immunology*, vol. 170, no. 4, pp. 1964–1972, 2003.

[17] J. M. Hernández-Guijo, R. D. Pascual, A. G. García, and L. Gandía, "Separation of calcium channel current components in mouse chromaffin cells superfused with low- and high-barium solutions," *Pflugers Archiv European Journal of Physiology*, vol. 436, no. 1, pp. 75–82, 1998.

[18] J. M. Hernández-Guijo, V. E. Maneu-Flores, A. Ruiz-Nuño, M. Villarroya, A. G. García, and L. Gandía, "Calcium-Dependent Inhibition of L, N, and P/Q Ca2 Channels in Chromaffin Cells: Role of Mitochondria," *The Journal of Neuroscience*, vol. 21, no. 8, pp. 2553–2560, 2001.

[19] N. Kuster and F. Schönborn, "Recommended minimal requirements and development guidelines for exposure setups of bio-experiments addressing the health risk concern of wireless communications," *Bioelectromagnetics*, vol. 21, no. 7, pp. 508–514, 2000.

[20] F. Sivandzade, A. Bhalerao, and L. Cucullo, “Analysis of the Mitochondrial Membrane Potential Using the Cationic JC-1 Dye as a Sensitive Fluorescent Probe,” *Bio-Protocol*, vol. 9, no. 1, 2019.

[21] S. W. Perry, J. P. Norman, J. Barbieri, E. B. Brown, and H. A. Gelbard, “Mitochondrial membrane potential probes and the proton gradient: a practical usage guide,” *BioTechniques*, vol. 50, no. 2, pp. 98–115, 2011.

Appendix I: Copyright permission to use Mitotracker Green labeled chromaffin cell

Email granting permission to use cell image of labeled chromaffin cells from the following journal: "The position of mitochondria and ER in relation to that of the secretory sites in chromaffin cells" by Jose´ Villanueva et. al 2014. The link to the journal is:

https://jcs.biologists.org/content/joces/127/23/5105.full.pdf.

Dear Ruby,

Thank you for your request. Permission is granted without charge for a thesis.

The acknowledgement is very important and should state "reproduced/adapted with permission" and give the source journal name - the acknowledgement should either provide full citation details or refer to the relevant citation in the article reference list - the full citation details should include authors, journal, year, volume, issue and page citation.

Where appearing online or in other electronic media, a link should be provided to the original article (e.g. via DOI).

Journal of Cell Science: http://www.biologists.com/journal-of-cell-science

We wish you the best of luck with your thesis.

Kind regards

Richard

Richard Grove

Commercial Manager

The Company of Biologists Ltd

Bidder Building, Station Road, Histon, Cambridge, CB24 9LF, UK

T: +44 (0) 1223 632 850 |richard.grove@biologists.com | www.biologists.com